OBJECT DETECTION USING FUSION OF MULTIBAND MICROWAVE DATA

A Thesis Submitted to

Delhi Technological University

For the Award of Degree of

DOCTOR OF PHILOSOPHY

In
ELECTRONICS & COMMUNICATION ENGINEERING

By
SANJAY SINGH
(2K15/PHD/EC/04)

Under the Supervision of
Dr K.C. Tiwari
Professor, Department of Civil Engineering
Delhi Technological University, New Delhi

DEPARTMENT OF ELECTRONICS & COMMUNICATION ENGINEERING
DELHI TECHNOLOGICAL UNIVERSITY
(Formerly Delhi College of Engineering)
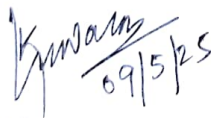Delhi-110042, India
May- 2025

CANDIDATE'S DECLARATION

I **SANJAY SINGH** certify that the work which is being presented in the thesis entitled **Object Detection using Fusion of Multiband Microwave Data** in the partial fulfilment of the requirements for the award of the degree of Doctor of Philosophy, submitted in the Department of **Electronics & Communication Engineering, Delhi Technological University** is an authenticated record of my own work carried out during the period from August 2015 to December 2023 under the supervision of **Dr K. C. Tiwari.**

The matter discussed in the thesis has not been submitted by me for the award of any other degree of this or any other institute.

Candidate's Signature

This is to certify that the student has incorporated all the corrections suggested by the examiner in the thesis and the statement made by the candidate is correct to the best of our knowledge.

Signature of Supervisor   Signature of External Examiner

CERTIFICATE

This is to certify that the thesis entitled "**Object Detection using Fusion of Multiband Microwave Data**" submitted by **Mr. Sanjay Singh** (Reg. No: 2K15/PhD/EC/04) for the award of degree of Doctor of Philosophy, to the Delhi Technological University, is based on the original research work carried out by him. He has worked under my supervision and has fulfilled the requirements, which to my knowledge have reached the requisite standard for the submission of this thesis. It is further certified that the work embodied in this thesis in neither partially nor fully submitted to any other university or institution for the award of any other degree or diploma.

(Dr K. C. Tiwari)

Supervisor and Professor,

Department of Civil Engineering

Delhi Technological University,

Delhi, 110042

ACKNOWLEDGEMENTS

ABSTRACT

Detection and identification of surface and subsurface objects has been an area of research for remote sensing experts. Globally, researchers have struggled to detect and identify subsurface buried landmines using remote sensing technologies. Despite several research and efforts, people still lose their lives from the explosion of hidden landmines near the border areas. India has also long been fighting insurgency along northern borders. Remote sensing technologies may be helpful in the detection and identification of all or some of these objects and targets, which may either be on the surface or buried. The Ability of all-time vision and penetration capability of Scatterometer (SCAT) and Synthetic aperture radar (SAR) makes them suitable for the detection of objects adverse weather conditions. In this research, improvement of detection of surface and subsurface objects has been has been studied through three objectives. All the three objectives are based on use of different microwave data and associated methodology to achieve the desired outcomes.

In the first objective, microwave remote sensing has been explored to detect buried targets (e.g., landmines). Although microwave-borne detection of shallow buried landmines is a safe option, it is a complicated and computationally profound process combining multiple parameters. This research uses data obtained in VV and HH polarizations and their fusion to minimize surface roughness for landmine detection. Therefore, in this objective, experiments have been carried out using a ground-based C- and X-band (VV and HH polarization) microwave scatterometer to detect landmines. A microwave transmitter setup was established on a 24x24 frame size (5 cm of each grid) to collect the backscatter data from a landmine buried under the dry sand. A wooden profile is used to vary the soil surface roughness from 1cm to 5 cm. Raw data is

subjected to various preprocessing steps: Calibration, deconvolution, and normalization. This objective involves processing under full-frame(24x24) and local-frame (8x8) processing. In this task, the polarimetric characteristics of waves and interaction with buried landmines are critically evaluated through histogram, segmentation of images, and various statistical characteristics. Various numerical polarization fusion approaches have been assessed for their effect on landmine detection. In addition, a numerical polarization fusion approach ((HH+VV)- (VV-HH)) has been evaluated. At last, the performance of all approaches has been evaluated using entropy. The result indicates that multi-polarization fusion approaches minimize the surface roughness effects, further enhancing landmine detection. Analysis of multiband (C- and X-band) has been presented at the end to explore multiband data's capability to discriminate objects.

In the second objective of this research, polarimetric characteristics of SAR have been utilized to improve man-made and natural object detection. PolSAR image is decomposed with hybrid decomposition methods to reduce the value of cross-polarization coupling of scattering components. The value of the overestimated (dominated) scattering component is evaluated by calculating the mean scattering power of single, double-bounce, and volume scattering components. A novel scattering component fusion of L- and C- band PolSAR image has been proposed and evaluated to reduce the effect of overestimation. In this approach, the double-bounce component of the L-band is fused with the C-band's single and volume scattering components. The principal component analysis (PCA) is employed for fusing the two data sets, and the result is evaluated through SVM classification of man-made and natural objects.

The third objective of this research focuses on image fusion of SAR and optical data. Sentinel-1A (SAR) and Sentinel-2A (optical) data have been downloaded from the

European Space Agency (ESA). This research also focuses on pixel-level SAR-optical fusion methods, fusion performance assessment, and applications. This objective explores an optimal combination of specific selected image fusion and image classification techniques to improve classification accuracy. Four fusion techniques, Brovey Transform, Hue-Saturation-Value (HSV), Principal component analysis (PCA), and Gram-Schmidt (GS) Transform, have been compared along with two classification methods, Support Vector Machine (SVM) and Maximum Likelihood (ML), have been explored. Improvement in five classes, urban, water, baresoil, forest, and vegetation agricultural, has been analyzed. The result indicates that the GS-ML combination gives superior classification accuracy than the GS-SVM combination. In contrast, PCA in combination with SVM provides superior accuracy compared to the combination of PCA-ML.

Based on the results of this research, the fusion of microwave data improves the surface and subsurface object detection in all three objectives. In the first objective, the research findings encourage the potential of multiband, multi-polarization fusion techniques for enhancing landmine detection capabilities. The second objective found that utilizing the polarimetric nature of SAR and the fusion of scattering components improves the result. The third objective finds that not all fusion techniques improve accuracy, and image fusion techniques influence the accuracy of classification methods. So, an optimal approach is needed to explore the capability of fusion techniques fully.

TABLE OF CONTENTS

LIST OF FIGURES

LIST OF TABLES

LIST OF ABBREATION

ALOS: Advanced Land Observing Satellite

ANN: Artificial Neural Network

AP: Anti-Personnel

ATK: Anti-Tank Mine

AWT: Adaptive Wavelet Transform

BOA: Bottom of Atmospheric

BT: Brovey Transform

CC: Covariance correlation

cGAN: Conditional generative network

CS: Component Substitution

CN: Colour Normalized

CNN: Convolutional Neural Network

DEM: Digital Elevation Model

DLF: Decision Level Fusion

DN: Digital Number

DWT: Discrete wavelet transform

EM: Electromagnetic

EMD: Empirical mode decomposition

ENL: Equivalent Number of Looks

ERGAS: Global Adimensional Relative Error of Synthesis (English translation of French word 'Erreur Relative Globale Adimensionnelle de Synthèse')

ESA: European Space agency

FDD: Freeman and Durden Decomposition

FLF: Feature Level Fusion

FQI: Fusion Quality Index

GPR: Ground Penetrating Radar

GS: Gram-Schmidt

GDP: Gross Domestic Product

IHS: Intensity Hue Saturation

HH: Horizontal transmitted Horizontal received

HPF: High Pass Filter

HR: High Resolution

HSV: Hue Saturation Value

HV: Horizontal transmitted Vertical received

IHS: Intensity Hue Saturation

LIDAR: Light Detection and Ranging

LR: Low Resolution

LULC: Land use Land Cover

MAP: Maximum A Posteriori

MB: Mean Bias

MI: Mutual Information

ML: Maximum Likelihood

MRA: Multi Resolution Approach

MS: Multi Spectral

NIR: Near Infrared

NSCT: Nonsubsampled contourlet transform

OA: Overall Accuracy

OAC: Orientation Angle Compensation

PAN: Panchromatics

PC: Principal Component

PCA: Principal Component analysis

PDR: Polarimetry Decomposition Ration

PLF: Pixel Level Fusion

PolSAR: Polarimetry Synthetic Aperture Radar

PTD: Polarimetric Target Decomposition

RADAR: Radio Ranging and Detection

RMS: Root Mean Square

ROI: Region of Interest

SAM: Spectral Angle Mapper

SAR: Synthetic Aperture Radar

SCAT: Scatterometer

SD: Standard Deviation

SF: Spatial Frequency

SRBM: Sparse Representation Based Techniques

SRD: Surface Roughness Depth

SRTM: Shuttle Radar Topography Mission

SSIM: Structural Similarity Index Measure

SWIR: Shortwave Infrared

SVM: Support Vector Machine

TOA: Top of Atmospheric

UIQI: Universal Image Quality Index

VH: Vertical transmitted Vertical received

VV: Vertical transmitted Vertical received

WGS: World Geodetic System

Chapter – 1
Introduction

1.1 Motivation

India, with a GDP (Gross domestic product) of 3 trillion US Dollars, is ranked 5th in terms of GDP amongst world economies and aspires to be the world's third-largest economy by the year 2030. Obviously, the country has to continue to evolve and adopt sustainable advanced technologies to realize this goal. India also became the 4th nation in the world to land on the moon on 23rd August 2023. This has given a tremendous boost to the space and remote sensing applications in the country. What is both interesting and intriguing is the fact that while humans have developed the capability to observe galaxies tucked miles away deep into space, we have still not been able to develop technologies to detect and identify subsurface objects buried barely meters below the surface of the earth. The recent tunnel collapse incident in Uttarakhand in India in November 2023 wherein 41 miners were trapped and almost all the technologies failed. Finally, it was the rat miners who dug a shallow tunnel with their hands to save precious lives. Similarly, globally researchers have been struggling to detect and identify subsurface buried landmines using remote sensing based far field technologies. The western and northern borders of India have experienced several wars, and landmines are still lying undetected in many places, which often results in the loss of precious lives. India has also long been fighting insurgency along northern and north-eastern borders, sponsored by its adversaries through the training camps and hideouts located just across the borders. Most of these targets present a mix of surface and subsurface objects and necessitate technologies for detecting not only surface but subsurface objects as well. Remote sensing technologies may be helpful in the detection

and identification of all or some of these objects and targets, which may either be on the surface or buried. For example, microwave remote sensing may possibly have evolved indigenously for the detection of subsurface landmines and objects, particularly along the western borders of India, which have deserts and where it may be successful.

Similarly, hyperspectral sensors may aid in detecting objects that otherwise may be difficult to detect in multispectral data. Besides, many times, the fusion of optical and SAR image is also capable of aiding the detection and identification of many of these objects. There, however, appears to be a limited indigenous effort in the exploitation of various possibilities that exist with the satellite-based remote sensing image [1][2][3][4][5]. The motivation for this work comes from a desire to explore and develop various possible ways to detect and identify various surface and subsurface objects and targets.

1.2 Remote sensing data types

Remote sensing is the discipline focused on obtaining data regarding a region, object, or occurrence without direct physical interaction. Objects at the surface either reflect a portion of the electromagnetic energy received from the sun or emit energy based on their temperatures. Remote sensing sensors record information about an object by measuring this reflected or emitted electromagnetic energy [6]. Since recording information at each wavelength of the electromagnetic spectrum is practically impossible, the sensors are often designed to record data in certain discrete bands only. However, data acquired in a few discrete wavelength bands always precludes accurate detection and identification of several surfaces and subsurface objects due to merging their reflectance with the background scene [6].

Primarily, there are two types of sensors: optical and microwave. Examples of optical sensors are hyperspectral, multispectral, and panchromatic sensors, of which

multispectral sensors are the most common. All multispectral sensors, however, depend upon reflected solar radiation to record information about ground objects in the visible and near-infrared bands and hence are known as passive sensors. This form of remote sensing is known as optical remote sensing and has been actively employed in mapping, forestry, agriculture, and military surveillance. However, the usefulness of this data gets restricted in areas under shadow, fog, darkness, camouflage, *etc.*, due to the inability of sunlight to illuminate and reflect from these otherwise accessible locations. A solution to this problem is the availability of data from active microwave remote sensing sensors, which have their energy source and are thus not dependent on sunlight. Due to their longer wavelengths, microwave frequencies (1GHz to 30 GHz) can penetrate fog, clouds, vegetation, and even the top layer of soil. The requirement of active microwave remote sensing has usually been felt in obtaining images of sub-surface (both ground and underwater) materials and objects and in areas of thick foliage, forest, vegetation, or camouflage cover [6] [7].

There are two types of active microwave sensors: imaging and non-imaging. SAR is an imaging sensor with high-resolution imaging capability. Altimeters, radiometers, and SCAT, which collect data in a single linear dimension, are examples of non-imaging active microwave sensors. Radiometers record the microwave radiation scattered or emitted by the Earth's surface or atmosphere, providing information such as humidity, temperature, and surface characteristics. Altimeters measure elevation or height, and a SCAT measures the backscattered objects precisely. The backscattered value depends on the object's characteristics (e.g., dielectric constant and roughness) and the angle of incidence on the object. The ground-based SCAT can, however, also be used to record the backscatter to generate an image of the surface being imaged. Ground-based SCAT can be calibrated and validated more quickly than their satellite

counterparts. The proximity to the instrument allows for direct measurements of calibration objects, reducing calibration-related uncertainties.

Remote sensing is being used extensively for the benefit of humanity through a variety of diverse applications, including forestry, land cover classification, agricultural, climate change and environmental monitoring, glacier and polar region mapping and monitoring, defence and security applications such as target/object detection, flood mapping, disaster management, and many more [8][9][10]. Remote sensing comes under the umbrella of Geoinformatics and is a multidisciplinary subject that has rapidly grown into a domain of interest across various disciplines.

Although, remote sensing has significantly aided in many applications but it has also resulted in several new challenges and issues depending upon the applications. These challenges can be in terms of specific data requirements, methodologies involved and the limitations of sensors etc. The focus in this work is on detection of surface and sub-surface natural and man-made objects wherein there are several challenges, however, the major challenge is detection and recognition of surface and subsurface objects with no or minimal *a priori* information [11]. These objects may be buried, shallow buried, or landscape surface objects. Specific requirements such as type and the object's location often dictate the selection of remote sensing data [12][13].

Amongst various subsurface objects of interest, the detection of shallow buried landmines has occupied the significant interest of researchers due to its well-known implications on military interest [14][15]. The humanitarian benefit of preventing casualties and saving lives in impacted communities motivates research on landmine detection. In addition, it helps with post-conflict reconstruction, environmental preservation, and technological innovation. Landmine detection necessitates a

multidisciplinary strategy. The effectiveness, precision, and safety of landmine detection systems must be improved via ongoing research and development to contribute to the worldwide objective of eliminating and protecting landmines.

Detecting surface objects in remote sensing applications faces numerous challenges, including susceptibility to sunlight, weather conditions, and spatial, spectral, and temporal resolution limitations. While multispectral and hyperspectral data offer enhanced spectral resolution for surface object detection, their functionality is hindered by daylight dependence and the requirement for clear weather conditions. In contrast, microwave SAR sensors overcome these limitations by providing all-weather capabilities and higher spatial resolution. Though much work has been carried out with some success to detect and identify shallow buried landmines, however even with SAR data, uncertainty exists on many issues, such as modelling microwave scattering, surface roughness effects, soil moisture effects, and background clutter [16][17]. Microwave reflections or emissions from surface and subsurface objects do not exhibit a direct correlation with their counterparts in the visible or thermal segments of the EM spectrum [18]. Research on detecting buried objects in sand, soil of varying moisture, and snowpack using microwave remote sensing has been a subject of active research.

Researchers are increasingly motivated to explore the fusion of SAR and optical image by recognizing the complementary strengths of SAR and optical sensors [11][19]. This synergistic approach aims to leverage the advantages of both technologies, combining the detailed spectral information from optical sensors with the all-weather, high-resolution capabilities of SAR. Such fusion techniques could enhance the accuracy and reliability of surface object detection across various environmental and atmospheric conditions, addressing the shortcomings associated with individual sensor types [20]. Many remote sensing-related problems are handled by fusing data acquired from active

and passive remote sensors, which is impossible with a single sensor [21]. Fusion of multispectral (MS) images with SAR images or with high-resolution image data has been recommended for spatial-spectral analyses to enhance object identification capabilities. SAR and optical images carry complementary information, so the fusion of these data is a complex issue that further needs investigation.

Besides, microwave remote sensors are single-band data, thus lacking spectral resolution, sometimes limiting their operations. SAR microwave data is unable to characterize objects independently, so to increase the dimensionality of subjected data, a fusion of two or more sensors with different frequency bands and polarisation may enrich the information for the surface and subsurface object detection [22][23][24]. Further analysis of the relative scattering coefficients from different object types for different wavelengths and polarisations needs investigation.

Although the fusion of microwave data has been researched for several years, it has now acquired momentum due to the availability of multi-resolution image with lesser revisit time from various space agencies.

1.3 Remote sensing for object detection

An object refers to a physical entity with a distinct and separate existence. It can be any entity that occupies space and has properties or characteristics. Objects can be categorized in terms of size, shape, and complexity and can be both natural or man-made. The term object has been used in a variety of ways and has been referred to as targets, endmembers, or end products of specific processes, and sometimes even to refer to various classes [25][26]. In remote sensing, an object refers to a distinct feature or entity within an image with spatial and spectral characteristics different from its surroundings /background [27].

1.3.1 Methods of object categorization

The objects may be categorized in many ways [27][28], as summarised below -

(i) Based on location:

(a)   **Surface (ground or water)**: Examples of objects in this category include urban structures, water pots, forests, and ships.

(b)   **Subsurface (buried):** Objects in this category are situated beneath the surface, and examples include landmines, caves, and submarines.

(c)   **Air**: Objects in the air, such as missiles and aircraft.

(ii) Based on condition:

(a) **Open/hidden camouflaged**: Objects can be classified based on their condition, which may be open, hidden, or camouflaged. Examples in this category include cantonments, hideouts, and camouflaged tanks.

(b) **Originated/Created**: Objects are also classified based on their origin or creation. Examples of objects originating from minerals or bunkers, whether on the surface or subsurface, fall into this category.

(c) **Buried (subsurface):** The condition for object classification is whether they are buried beneath the surface. An example provided in this category is landmines and underground gas pipelines.

(iii) Based on shape:

(a) **Point**: Objects categorized as points but no spatial dimensions. Point objects include examples such as tree, vehicle, buildings, and bridges. It uses individual point coordinates to localize and recognize objects

(b) **Linear:** Linear objects are characterized by their elongated form. Examples in this category include rivers, roads, and canals.

(c) **Area**: Objects with an area-based shape cover a specific region. Examples provided are urban, village, agricultural vegetation, forest, and river. These are also known as landscape objects.

(iv) Based on size

(a) **Group of Pixels**: Objects falling into this category are characterized by more extensive pixel collections. Examples include towns, villages, and store dumps.

(b) **Pixel:** Pixel-sized objects are more defined and distinct. Examples in this category comprise tanks, vehicles, and wells.

(c) **Sub-pixel**: Sub-pixel objects are smaller and more detailed than regular pixels, including tanks, vehicles, and wells.

However, an appropriate categorization of the objects may be the first step in object detection since the object type may dictate the selection of appropriate remote sensing data and the processing technique. For example, optical remote sensing may not be suitable for detecting subsurface or camouflaged objects, which may require microwave remote sensing data [27].

1.3.2 Challenges in object detection

Table 1.1 summarises various challenges reported by researchers during the process of remote-sensing object detection. Selection of remote sensing data, appropriate object detection methodology and surroundings clutters are vital challenges that limit object detection.

1.4 Buried object detection using microwave data

When an electromagnetic (EM) wave interacts with buried objects, several phenomena occur that can provide information about the objects' properties and

characteristics. Reflection, scattering, and absorption are the three main events that occur during the interaction of an EM wave with the buried object. When an EM wave encounters a buried object, a part of it is reflected towards the surface. The reflected

Table 1.1 Challenges in Object detection

Challenges	Description [6][18][27][28][29]
Complex Surroundings	It is challenging to distinguish objects from the background when the surroundings are cluttered with diverse elements.
Object Occlusion	Partial or complete occlusion of objects by other objects or natural features affects accurate detection.
Scale Variation	Objects in remote sensing data can vary significantly in size, requiring scale-invariant algorithms.
Spectral Variability	Objects of the same class exhibit spectral variations due to lighting conditions or inherent properties.
Limited Training Data	Obtaining high-quality labelled training data for object detection is time-consuming and costly.
Class Imbalance	Unequal representation of object classes in the dataset can result in biased predictions or poor performance.
Computational Complexity	Object detection in large-scale or high-resolution datasets can be computationally demanding.
Generalization of model for Dataset	Models trained on one dataset may need to generalize better to different datasets or domains.
Data Variability	Variations in sensor characteristics, acquisition parameters, and environmental conditions introduce variability.

wave carries information about the object's size, shape, and composition. Analysing the phase and amplitude of the reflected wave makes it possible to infer the features of the buried object, such as its location, geometry, and material properties. Scattering occurs

when the EM wave interacts with the object's boundaries or discontinuities, causing changes in the direction and intensity of the wave. Some EM waves are absorbed by buried objects, reducing the intensity of the transmitted or reflected waves. The absorption depends on the object's composition and the frequency of the EM wave [30].

Imaging buried landmines beneath rough surfaces poses a complex inverse scattering challenge with numerous engineering applications. These buried devices, designed to detonate upon contact, present significant threats, causing harm and leaving enduring psychological impacts.

Landmines used on battlefields are illegal under international humanitarian law, which protects people who have left armed conflict or are not involved in it. Due to the lack of effort to clear landmines from affected areas, several years after a war/conflict has ended, buried landmines continue to threaten civilians. It was not only the security forces but also the insurgents and guerrillas who have used landmines as a weapon in civil wars and insurgencies for decades [31].

Landmine inspection systems that are reliable are in high demand. Challenges arise from the lack or unavailability of maps or data regarding landmine types and original placements, as well as the shifting of their locations due to environmental and physical factors. The diverse range of landmines and the substantial costs associated with their detection and removal further complicate the process. Moreover, individuals are at risk due to the sensitivity of landmines to detonate over time or in response to atmospheric variables. Table 1.2 summarises the currently available landmine detection techniques.

Several approaches for demining, or identifying and removing buried landmines, have been designed and developed. Depending on the explosion, soil and

type of landmine casing, each method is preferred for detection under certain conditions. Addressing the issue of landmine detection requires not only the development of techniques capable of meeting this formidable challenge but also the customization of these techniques to suit local conditions. Effectively applying any given technique is more feasible when there is a clear understanding of the nature of the mines, soil composition, and background clutter. It is unrealistic to expect a singular detection technology to fulfil all requirements, highlighting the necessity for a systems fusion approach to tackle the complexities of landmine detection effectively [32].

Numerous landmine types and burial ground, such as fields, buildings, roads, forests, and deserts, complicate the detection problem [33]. The manual clearance of landmines remains a highly preferred method despite technological advancements due to its consistency, predictability, and reliability. However, a traditional method's shortcomings include its slowness and worker safety risks [34]. Over the years, much of the work has been done in retrieving buried landmines. The object's shape and orientation affect microwave scattering differently in different polarizations. Therefore, polarisation plays a significant role in determining the shape and orientation of the object. A neural network-based classifier was successfully employed to detect buried objects. The system detected and mapped pipes, cables, and anti-personnel landmines [11]. Using neural networks to detect dielectric cylinders distributed over an area has also been reported by Caorsi *et al.* (2005) [35]. Therefore, neural networks and other advanced computing techniques may extract various properties of buried objects, such as shape.

Microwave scattering is influenced variably by the shape and orientation of an target across different polarizations. Therefore, polarisation significantly influences the

shape and orientation of the target. Bhadouria *et al.* (2021) [11] successfully employed a neural network-based classifier to detect buried objects. The system successfully detected and mapped pipes, cables, and anti-personnel landmines. The use of neural networks for detecting dielectric cylinders distributed over an area has also been reported by Caorsi *et al.* (2005) [35]. Therefore, neural networks and other advanced computing techniques may extract various properties of buried objects, such as shape. Amiri *et al.* (2012) [36] aimed to investigate the extent of multi-frequency wave propagation in GPR. The findings are then applied to designing a new multi-band antenna with frequency-switching capabilities. The antenna's chosen operating frequencies fall between 0.5 and 5 GHz. A commercial program based on the Finite Integral Method simulates various ground penetrating radar (GPR) models. The simulation results show that the selected upper and lower bands offer a complementation between penetration, and range resolution.

A novel buried object detection method specifically designed for the detection of unexploded landmines is proposed by Bestagini *et al.* (2021) [14]. The suggested methodology uses a convolutional neural network (CNN) known as an autoencoder to analyse volumetric data obtained by GPR with various polarizations. This technique, GPR, collects the data in landmine-free regions to train the autoencoder within an anomaly detection framework. Landmines are then identified by the system as objects that differ from the soil that was used in the training phase. Most of the reported landmine detection research is focused on estimating dielectric variations near the buried landmine. However, these variations get severely diminished for various reasons, primarily the scattering due to surface roughness and the dielectric contrast at the air-soil-landmine interface.

The most frequent issue with buried landmine detection is the backscatter from the ground clutter that overrides the backscatter from buried landmines. To get around this, some researchers created polarimetric and multifrequency techniques to differentiate between the return and individual utilities [14][36][37]. There is ongoing research on the field of landmine detection, but still maximum approaches are the complex in working and require a large amount of data. As a result, it is currently necessary to reduce complexity and create a model for finding buried landmine objects.

1.5   Surface object detection using SAR data

Now-a-days, imaging radars are playing a crucial role in investigations related to the Earth and other celestial bodies. It can be done by analyzing data acquired from an overhead perspective by the transmission and reception of EM waves from the microwave spectrum. For this purpose, SAR has served humanity over the last several decades. In SAR, a satisfactory resolution in the azimuth direction is achieved by 'synthesizing' a larger virtual aperture of the antenna. The radar antenna, which acts like a single array element of the antenna, is mounted on a moving platform. The platform motion moves this single element through successive element positions on a known trajectory to form the complete array.

A pulse is transmitted at each element position along the path, and the scattered EM wave from the object is received. When the single element has travelled across the length of the complete array, the received backscattered signal from each element position is coherently combined to create the effect of a large phased array antenna. The SAR system thus synthesizes a virtual aperture equal to the length of a phased array antenna that is much larger than the physical length of the actual antenna. SAR imagery is a complex image having real (amplitude) and imaginary (phase) components. Based

Table 1.2 Landmine detection technique

Landmine detection technique	Cost, complexity	False alarms	Limitations
Biological methods [38][39][40]			
Dogs, rodents, bees, plants, bacteria: • Dogs possess a strong sense of explosive smell and can detect various explosive degradation. • Rodents are trained with nourishment to point the presence of explosives by scratching. • Bees are trained to the odour of an explosive with food. • Genetically converted bacteria emit fluorescence in the presence of explosive materials.	low	low	• Dogs require maintenance and training, and performance decrease with time. • Rats are generally untrained and prone to tropical diseases. • Bees can work under only particular climate weather. • Highly sensitive to weather (bacteria).
Ultrasound detection [41]			
• The Sensor emits sound wave of higher frequency into soil and records the signal after reflected from the interface of materials with dissimilar acoustical behaviour. • It is useful for both soft and hard ground and provides real-time monitoring.	high	Low	• Penetrate a certain depth only; after that, they are attenuated by the soil.

Prodders approach [41]			
• In prodding, Physical manual prodding using nonmagnetic rods is used to penetrate the ground for landmine detection. • In the presence of a landmine, it exhibits vibration and produces sound or increased resistance.	low	medium	• Risky as it involves proximity to landmine • Limited coverage range • Effective only for shallow-depth landmine
Electromagnetic based method [42][43]			
• **Metal detectors** collect the disturbance of an emitted EM wave caused by metal components in the soil. • Magnetometers, exclusively for ferromagnetic objects, measure only the disturbance of the earth's natural EM field. • It scans a large area with an array of metal detectors.	medium high	medium medium	• Can identify metallic objects but cannot differentiate them from debris. • Increasing sensitivity increases false alarm rates due to metal debris. • It cannot detect non-metallic landmines.
• • **X-ray backscattering** entails directing X-rays downward. Because of their higher electron density, materials with less atomic numbers—like plastics—disperse X-ray radiation more effectively.	high	medium	• It is affected by background clutter during the detection process.
• By using a two-dimensional array of electrodes positioned on the ground, **electrical impedance tomography** creates	high	medium	• False alarm generated due to mine-like conducting objects.

a map of the conductivity distribution in which mines are identified as anomalies.			
Advance application of metal detector [43][44][45]			
▪ **Impulse metal detectors** Discriminates mines from metallic debris and reduce false alarm rates by comparing characteristic decay curve with curves stored in a library. ▪ Based on eddy current frequency response over a large frequency band.	high	medium	• Response curve depends on the orientation of the metallic object, metal type, etc., and is effective only with objects whose decay curves are already known.
▪ **Meandering winding magnetometer** is a square wave-winding conductor generating a spatial periodic EM field, the wavelength of which depends on the primary winding spatial periodicity.	high	medium	• Suitable for objects with some metallic content • It can detect object shape, size, etc., but its application is still under investigation.
▪ **Cavity detector** locates nonconducting objects, or "cavities", relies on the theory that a sizeable nonconducting object locally alters the natural ground conductivity.	high	low	• Large items are best detected by the cavity-locating system in soils with strong conductivity by nature.
Ground penetrating radar [14][35][36]			
• Radar detects landmines by transmitting and receiving reflected signals from objects using a wideband antenna. Reflection caused by dielectric variations are measured. • By moving the antenna and image processing, 3D representation generated.	high	low	• Detecting smaller objects requires GHz frequencies, which Limit the soil penetration • False positives caused by other buried objects

Bulk explosive detection [33][41]			
Thermal neutron analysis (TNA) Neutrons are released in TNA, and when a nucleus absorbs one of them, gamma rays with an energy unique to that nucleus are released.	high	low	• TNA system is complex, and soli penetration is 10-20 cm only.
High-energy neutrons are used in **fast neutron analysis (FNA)** to identify and classify gamma radiation at various energies.	high	medium	• Relies on hydrogen nuclei also present in water, hence effective in dry environment.
The same idea behind FNA is applied in **pulsed fast neutron analysis (PFNA)**, which uses a pulsed neutron beam.	high	medium	• Not effective in wet environment
Pulsed fast thermal neutron analysis, uses continuous neutron beams. Its transportable construction and great dependability are its key benefits.	high	medium	• The Process is complex and compelling only for dry soil penetration.
Nitrogen nuclei in the explosive are excited by radio frequency pulses sent by **nuclear quadrupole resonance (NQR)**, which creates an electric potential at a receiver coil.	high	medium	• NQR difficult to adopt for mine detection
Unmanned aerial vehicles [36]			
Drones equipped with sensors, such as cameras and thermal imaging, can survey and detect landmines from the air.	high	medium	• Limited flight time and coverage area • Challenging detection in dense vegetation or uneven terrain

on these components, the analysis of SAR can be divided into two approaches: SAR backscatter analysis and polarimetry analysis [46][47].

SAR backscatter analysis aims to understand and interpret the radar backscatter signals that the SAR system has detected. Analyzing data on the magnitude or strength of the backscattered value is necessary to learn more about the characteristics and features of the investigated objects. Radiometric calibration, backscatter signatures, backscatter coefficient, and backscatter modeling are vital aspects of SAR backscatter analysis [46].

Polarimetry of any EM wave is the method of accessing, processing, and investigating the state of polarization. Polarimetric SAR (PolSAR) upgrades the capacities of SAR by introducing a polarimetry to it. However, to express the polarization state of an EM wave, two orthogonal polarization basis vectors are required. A fully polarimetric SAR system transmits two orthogonal polarizations and coherently receives by dual orthogonal polarized channels. Since the polarization information present in the backscattered wave is sensitive to the geometrical structure, orientation and shape of a given target, a PolSAR system greatly helps in extracting the significant information of the target or scatterer. PolSAR system involves transmitting and receiving SAR signals in multiple polarization states, such as (VV, VH, HV, and HH), to capture additional detail about the scattering mechanisms and attributes of the imaged objects. Here, 'VV' stands for vertically transmitted and vertically received, whereas 'VH' stands for vertically transmitted and horizontally received EM wave. Polarimetric decomposition, polarimetric parameters, target classification, and interferometry are vital aspects of polarimetric analysis [48].

SAR polarimetry allows for decomposing the complex polarimetric data into different scattering mechanisms techniques like Freeman and Durden decomposition (FDD), Yamaguchi, and Cloude-Pottier decomposition can separate the backscattering contributions from different types of scattering, such as surface, double-bounce, and volume scattering. SAR polarimetry provides several polarimetric parameters, such as coherency matrix elements, polarimetric entropy, anisotropy, and scattering power, which characterize the scattering properties of the imaged scene. These parameters help identify and discriminate between types of targets and surface conditions [48].

A pixel value in SAR imaging is the total of all the coherent reflections of the signal received from the targets. While polarization measurements collect surface characteristics, such as roughness and shading, they are frequently uncorrelated with SAR intensity imagery and offer information on the materials in the scene. PolSAR imaging depends on the electromagnetic properties of the objects in the image, such as their complicated permittivity and the object's roughness concerning the wavelength of the radar beam. Longer wavelengths are more effective at penetrating clouds and the ground. The wavelengths of L-band (20 cm) radar, for instance, are longer than those of C-band (6 cm), X-band (3 cm), and Ku band (2 cm).

In their study, Maleki Saeideh. *et al.* (2019) [49] introduced a semi-empirical technique that leverages eight images. These images were acquired across three different frequencies, polarizations, and incidence angles. The study evaluated the efficacy of various SAR configurations in distinguishing land cover classes using the Support vector machine (SVM) technique. The study considered the impact of wavelength, polarization, and incidence angle when combining these SAR images. Guida *et al.* (2015) [50] proposed a wavelet transform based approach and choose-max fusion approach for the fusion of S- and X-band data. The number of vanishing moments

and decomposition levels were to control the fusion parameter. Combining Daubechies wavelet transform with two vanishing moments, one decomposition level, and the choose-max fusion rule.

Availability of microwave sensors in a multiparametric mode, i.e., multifrequency/wavelength (P, L, S, C, X, and Ku band), multi-angle (10°-80°), multi-polarisation, multi-resolution data (from cm to km) and multi-temporal data has provided researchers with a significant amount of diverse data The penetration depth of microwave sensors is inversely related to their frequency band; the higher the frequency lowers the penetration depth. The deep penetration depth of microwave sensors characterized the volume scatterers, like dry soil, sand, ice, and vegetation. The microwave sensor's wave polarisation (HH, VV, HV, and VH) is sensitive to the texture and orientation of objects, which therefore emphasizes various other features. The availability of multiband and multi-polarisation microwave datasets and their nonoverlapping properties opens a domain to combine this dataset with some image fusion algorithms to explore various Remote sensing applications.

Even if examining or studying these data is beneficial, there is a growing effort and interest in fusing multi-platform data to provide a fused image that contains more information than examining individual sensor data. Nevertheless, most of these initiatives have concentrated on combining data from several sensor —for example, optical imaging systems with SAR or LIDAR data with optical. Further research is required on exclusively combining multi-frequency, multi-polarization SAR data [50].

1.6   Remote sensing image fusion of microwave data

In optical image, the reflectance of an item within the detectors' spectral range is represented by its pixel value. On the other hand, microwave sensors lack spectral

resolution, limiting landscape surface object detection. Microwave SAR image is insensitive to spectral response, complicating data processing and interpretation. Due to the nonoverlapping nature of these constraints with optical images, SAR and optical imaging provide complementary information. The fusion of SAR and optical datasets enables the creation of a composite image rich in spatial and spectral data. All-season and penetration capability of SAR sensors make them better suitable for fusion with optical sensors.

The research by Amarsaikhan *et al.* (2010) [21] indicates that multi-source information from optical and SAR sensors enhances the interpretation and classification of land cover types. It is clear from their research that using optical and SAR images in tandem has several benefits since the complimentary information from both sources can make a certain feature visible on the microwave image that is not visible on the passive sensor images and vice versa. Various aspects of image fusion methods have been well addressed by Pohl *et al.* (1998) [9], Simone *et al.* (2002) [10], Amarsaikhan *et al.* (2011) [51] and Alparone *et al.* (2004) [52].

Image fusion is a process of merging two or more images in such a way as to achieve the desired result. The complexity and result achieved also depend on the processing level of fusion. If two images have been combined at the initial level, it is known as pixel-level fusion (PLF). If the fusion is done with features of images, it is known as feature-level fusion (FLF). The higher processing level of fusion is decision-level fusion (DLF), used to combine the decisions of two or more approaches. PLF has the highest computation burden, as it is done on raw data, but contains the maximum amount of information.

The choice of image fusion method and evaluation parameters are subjective. It is a matter of research which fusion methodology and fusion evaluation parameter best

suits a particular set of microwave data and applications. Motivated by this aim, an intense literature review has been conducted for fusion and evaluation methodology for microwave data with optical data.

1.6.1 Image fusion methods for microwave data

Based on the literature review, image fusion may be categorized into five parts as shown below. All these categories are compiled with references in Table 1.3.

Table 1.3 SAR-optical PLF methods

SN	Fusion Category	Approaches	Comments
i)	Component substitution	PCA [21] [53[[54][55], GS [56], IHS [57][58][59][60], Ehler [61] [62]	Less Computation and easier to perform. Highly dependent on correlation.
ii)	Numerical techniques	HPF [62], BT [21][63], Modulation based Techniques [64]	More spectral distortion. Not found much suitable for SAR-optical fusion.
iii)	Multi-Resolution Approaches	Pyramidal decomposition [65], Wavelet [66][67], Directional Approaches: curvelet, contourlet [68] [69]	Less Spectral distortion. Sometimes computationally complex
iv)	Model Based techniques	Variational model [70], CNN based [71], cGAN [72][73]	Less susceptible to registration errors.
v)	Hybrid Approaches	NSCT+ HIS[74] , IHS/PCA + DWT/AWT[75][76][77], Modified BT[78], IHS+AWT+ EMD+ AWT + IHS [79], weighted median filter + GS[80], PCA + curvelet transform [81]	Reduce spatial and spectral distortion.

Here in Table 1.3, GS- Gram-Schmidt; IHS-Intensity hue saturation; BT – Brovey Transform HPF- High pass filter; AWT -Adaptive Wavelet transform; DWT- Discrete wavelet

transform; HPF- High pass filter; cGAN -Conditional generative network; NSCT-Nonsubsampled contourlet transform; EMD-Empirical mode decomposition

1.6.1.1 Component substitution techniques

The component substitution (CS) fusion techniques are separated into three phases. First, forward transformation is applied to the optical bands after they have been registered to the SAR bands. Second, another component of the transformed data domain similar to the SAR image is replaced by the higher resolution band. Third, an inverse transform of the original space is used to construct the fused results.

Prominent methods in CS include Ehlers fusion, PCA, IHS, and Gram-Schmidt (GS). IHS is a method for extracting spectral and spatial information from MS bands. The intensity (I) component is substituted with the histogram-matched SAR band. To create integrated MS data, the rearranged I, Hue (H), and Saturation (S) components are translated inverted into the original domain. The limitation of IHS to three bands was overcome by Tu *et al.* (2004) [82], who created the generalized IHS. Researchers have proposed the adaptive IHS method to keep developing IHS-based results to overcome problems of poor spectral quality issues [5].

To optimise the variance of the source image, PCA transforms an image by translating and rotating it into a new coordinate frame. This technique computes the PCs, then reassigns the high-resolution SAR data into the data space of the first PC and replaces it with PC1. Then, from PC1 to the original MS data, an inverse PC transform is accomplished. This technique adjusts SAR data to about the same data space as PC1 before performing the inverse PC computation [83]. The first PC in Gram–Schmidt (GS) transform may be selected freely, and the other components are computed orthogonally to the first PC. The GS transform (GS) is used to convert MS and simulated SAR, and the resultant bands are utilized in the CS method. The statistically matched SAR

replaces the first GS band. The fused image is the output of the inverse GS transform [84].

To enhance land cover mapping, Herold *et al.* (2002) [53] present a fusion of SAR and MS imagery utilising different layer additions and PCA techniques. After fusion with the SAR image, classification accuracy improves substantially. Harris et al. (1990) [58] utilise the IHS transform to combine radar and MS images. El-Deen *et al.* (2010) [85] evaluate PLF methods based on IHS, PCA and the Brovey (BT) for a PLF of MS and SAR images to enhance overall classification accuracy for seacoast shoreline extraction. Fusion based on IHS yields higher categorization accuracy. To enhance land cover categorization accuracy, Amarsaikhan *et al.* (2011) [51] suggested a combination of high-resolution SAR and MS bands. The multiplicative approach, IHS, PCA, and BT-based PLF are used to fuse source images, and the outcomes are evaluated visually and based on overall accuracy. Abd *et al.* (2016) [56] evaluate IHS, BT, and GS transform optical and SAR image fusion techniques to enhance classification results while extracting shorelines. It has been discovered that using integrated images increases the precision of coastline extraction. These methods provide a fused output that is good with spatial information. Due to spectral dissimilarity in the bands of heterogenous images, there are pixel-level discrepancies between images being fused, that may develop significant spectral distortions in the integrated output [86][87].

1.6.1.2 Numerical fusion methods

Mathematical combinations of various images are amongst the most straightforward PLF techniques. They combine the digital numbers of the images fused at a pixel-by-pixel basis using mathematical operators such as sum, multiplication, subtraction, multiplication etc. Multiplication can be a powerful fusion method and

leads to perfect results for visual interpretation if optical and radar images are combined [98].

Fusion by multiplication enhances the contrast and joins MS with textural information from the SAR data. Selection of weighting and scale variables may enhance the fused image. The BT normalizes MS data, and the resultant channels are multiplied by the intensity channel. It is not exactly a transform but a multiplication using a SAR band based on a normalization of the MS bands. A smoothing filter-based intensity modulation method modulates optical data by using a ratio between the SAR and its histogram image. It utilises modulation of an intensity channel with spatial detail to make it applicable to SAR fusion [64]. Color spectral sharpening expands the BT to accommodate for more than three input channels. The method standardises the input and divides the spectral space into color and brightness. It normalizes the data by multiplying every MS channel by SAR data and dividing it by MS input images.

The High pass filter (HPF) method collects high-frequency information, which is subsequently added to every MS band [9]. For the integration of SAR with MS, Chandrakanth *et al.* (2014) [65] use frequency domain high pass filtering. Misra et al. (2012) [88] offer a PLF method for merging low-resolution (LR) optical bands with a high resolution (HR) SAR data using the wavelet transform, a variation of the BT.

1.6.1.3 Multi-resolution approach (MRA)

It is also called the multiscale decomposition method. The MRA relies on the insertion of spatial information that is acquired from the multi-resolution decomposition of the SAR band into the resampled multispectral images. In these techniques, the fused source images are first decomposed at various scales using an appropriate multi-

resolution technique. Afterward, fusion methods are enforced to every decomposed part, and the fused bands are inverse transformed to generate the required data [86].

Wavelet-based techniques are classified into two categories. The first method involves swapping a LR sub-band for a HR sub-band. The second method is built on inserting information from HR sub-bands into LR sub-bands [89]. Another common MRA technique is the non-subsampled wavelet transform. Because of its shift-invariance, this kind of multiscale transformation is ideal for multisensory data such as SAR and MS images. Abdikan *et al.* (2012) [55] compare component replacement and wavelet based fusion techniques. The HPF method and the wavelet-based techniques provide numerically comparable results, but the wavelet method yields aesthetically superior results.

Rahman *et al.* (2010) [5] compare CS methods to wavelet-based fusion methods for increasing sub-surface and surface aligning accuracy. Alparone *et al.* (2004) [52] offers an undecimated wavelet fusion technique of SAR, panchromatic (PAN), and optical bands to increase the spatial resolution of the optical band. To begin, PAN and MS bands are merged, then texture information from SAR bands is injected into a pan-sharpened band to produce the resultant fusion output. Amarsaikhan *et al.* (2010) [21] utilise wavelet PLF to merge optical and HR-SAR data. The results are compared to BT, PCA and Ehlers fusion for improved landuse-landcover (LULC) categorization. It has been discovered that images merged using BT have a higher spatial resolution. This research also shows that using integrated satellite data increases accuracy. Lu et al. (2011) [68] combine optical and SAR data using curvelet decomposition. The results outperform IHS and the wavelet-based fusion technique.

Using a multiresolution transform adds computational complexity, but it results in improved fusion performance owing to simultaneous localization in the time and

frequency domains [86]. Wavelet-based techniques improve spectral resolution but introduce spatial distortion.

1.6.1.4 Hybrid methods

Hybrid techniques combine CS and MRA to make use of the benefits of both methods, resulting in improved spatial and spectral resolution. Hunag *et al. (*2005) [75] fuse SAR and MS image using the IHS and the DWT for better urban mapping. After transformation of MS bands to the IHS domain, the I-component and the SAR data are decomposed by a wavelet-based method. When this approach is compared to PCA, the suggested hybrid strategy outperforms PCA in terms of classification accuracy. Hong *et al.* (2009) [66] proposes a hybrid PLF technique that depends on the wavelet-based transform and IHS to merge a SAR data with MS data. The PLF method in this technique depends on the neighbourhood correlation between sensors images. The suggested hybrid technique is evaluated with traditional wavelet-based fusion and IHS methods.

Chibani Youcef (2006) [78] suggests modifying the BT to include SAR characteristics in MS images. MS bands are modified by a fraction of the new I-component to the old I-component in this technique. The newer I-component is created by combining high frequency information derived from AWT bands with SAR and inserting them into the previous component. To fuse MS and SAR images, Han *et al.* (2010) [90] offers a hybrid method that depends on combining the adaptive wavelet transform and IHS. After converting the MS data to IHS space, AWT is used to dissect the I-component and SAR data. Applying statistical methods, the decomposed sub-images are merged, and the merged sub-images are rehabilitated to give a merged I-component, which is then inverse transformed to the initial MS domain [91].

Zhang *et al.* (2020) [92] examine several fusion techniques for a hybrid approach that includes IHS transformation and non-subsampled contourlet transform. The

intensity image contains spectral data, while the texture SAR image contains spatial data. To get the most spatial and spectral detail in the fused data, these two images are merged using the PCA technique. It has been discovered that the fused data improves sea-ice recognition. Hybrid techniques combine the benefits of both MRA and CS fusion procedures. It has been discovered that hybrid fusion techniques combining MRA and CS methods result in improved SAR-optical image fusion [62].

1.6.1.5 Model-based techniques

Several model-based methods of fusing remotely sensed data had been suggested, and researchers also implemented them for PLF of SAR and optical images. Sparse representation-based techniques (SRBM) and the variational technique are two of the most used methods.

The variational fusion technique developed for PLF of MS and PAN bands were expanded for PLF of MS and SAR bands by Zhang et al. (2010b) [93] for improved comprehension of urban characteristics. The energy function is minimised in this fusion method, ensuring that colour detail from MS data and textural detail from SAR data are combined. Image fusion is approached as a restoration problem by sparse representation-based methods, which generate HR fused data from a linear integration of pixels drawn from an over-complete dictionary of HR and LR data. The sparse co-efficient of the initial data are merged according to the PLF method, and the merged data is rebuilt adopting the aforementioned dictionary. For a better comprehension of urban characteristics, the variational fusion technique developed for a fusion of MS and PAN bands is extended for fusion of MS and SAR bands [79]. This fusion method minimises the energy function, ensuring that color details from MS bands and geometry details from SAR bands are combined. Image fusion is approached as a restoration issue by sparse representation-based methods, which create HR fused data from a linear

integration of pixels chosen from an over-complete dictionary of LR and HR bands. The sparse co-efficient of original images was fused, and a fused image was created using the same method.

For merging airborne SAR and optical data, Liu *et al.* (2016) [94] propose a joint non-negative sparse technique using IHS. To begin, an I-component is retrieved by applying the IHS transformation to MS images. The sparse coefficients of the I-component are combined with the sparse coefficients of the SAR band. Fused data is produced by inverting the changed I-component. In certain cases, sparse representation methods outperform other techniques; nevertheless, dictionary creation and sparse coding are the main problems [95].

It has been noted that hybrid fusion approaches are more attractive owing to their capability to manage the issue of spatial and spectral distortion and their lower complication when compared to sparse representation techniques.

1.6.2 Fusion evaluation measures for microwave data

Image fusion has several applications, and no image fusion technique performs equally well in under every circumstance. To verify the fusion technique, the fused images were evaluated using three methods: objective, subjective, and comprehensive assessments [96]. Objective assessment has been done by quality measures (based on the presence or absence of reference data). The reduced resolution assessment is used, when reference image may not be available.

1.6.2.1 Objective evaluation (quality metrics)

Jagalingam *et al.* (2015) [97] provide a comprehensive analysis of quantitative measures used to assess fused images. A few assessment measures are described below.

1.6.2.1.1 Metrics (when the reference data is available)

When the of a reference image is available, quantitative measures such as correlation coefficient (CC), mean bias (MB), signal to noise ratio, mutual information (MI), Global Adimensional Relative Error of Synthesis (ERGAS), structural similarity index measure (SSIM), root mean square error (RMSE), spectral angular mapper (SAM), universal quality index (UIQI/Q) etc. are calculated for SAR-Optical fusion. Table 1.4 shows the evaluation metrics with references. SSIM evaluates structural preservation, ensuring that important spatial and textural details from source images are maintained in the fused output. CC measures the linear correlation between fused and source images, indicating how well the spectral content is preserved. Entropy quantifies information richness; higher entropy reflects better feature retention.

1.6.2.1.2 Metrics that do not need reference data

Under the absence of a reference image, the quantitative measures such as entropy, cross entropy, standard deviation (SD), fusion quality index (FQI), mutual information, spatial frequency (SF), etc. Table 1.5 shows the objective evaluation measures (reference data not required).

Table 1.4 Metrics (when the reference data is available)

SN	Measures	References	Main points/Formula
1.	CC	[55][66][69][70] [79][96]	Calculate the spectral feature similarity between the integrated and reference. $$CC = \frac{\sum_{i=1}^{m} \sum_{j=1}^{n}(R_{i,j}-\overline{R})(F_{i,j}-\overline{F})}{\sqrt{\sum_{i=1}^{m} \sum_{j=1}^{n}((R_{i,j}-\overline{R}))^2(F_{i,j}-\overline{F})^2}}$$ R and F are a reference, and fusion image, respectively and $\overline{R}$ and $\overline{F}$ are corresponding mean images.

2.	SAM	[96][98][99]	Calculate angle between integrated and reference images.

$$\text{SAM} = \arccos \left(\frac{\sum_{i=1}^{B} F_i R_i}{(\sum_{i=1}^{B} F_i^B)^{1/2}(\sum_{i=1}^{B} R_i^B)^{1/2}} \right)$$

B represents the number of bands.

3.	UIQI/Q4 index	[55][69][79][99]	Calculates the amount of relevant information transform from reference to integrated images.

$$\text{UIQI} = \frac{4\sigma_{FR}\overline{F}\overline{R}}{(\sigma_F^2 + \sigma_R^2)(\overline{F}^2 + \overline{R}^2)}$$

σ^2 is variance.

4.	RMSE	[66][79][100]	Evaluate the variance in pixels to get the difference between the reference and integrated images.

$$\text{RMSE} = \sqrt{\frac{1}{MN} \sum_{i=1}^{M} \sum_{j=1}^{N} (R_{ij} - F_{ij})^2}$$

M and N are rows and columns.

5.	ERGAS	[96][99][101]	Calculates the attribute of the integrated data in perspective of the normalised error of individual processed image. Higher value, more distortion in the merged image.

$$\text{ERGAS} = 100 \frac{s}{m} \left(\frac{1}{B} \sum_{i=1}^{N} \left(\frac{\text{RMSE}^2}{\text{mean}^2} \right) \right)^{\frac{1}{2}}$$

Where *s* and *m* are the SAR and multispectral image resolution, respectively.

6.	Mean Bias	[55][100][102]	Difference between mean of fused and reference image.

$$\text{Mean Bias} = \frac{\text{MS}_{\text{mean}} - \text{Fused}_{\text{mean}}}{\text{MS}_{\text{mean}}}$$

7.	SSIM	[66][100][102]	Compute the pixel patterns between the integrated and reference images locally.

$$\text{SSIM} = \frac{(2\mu_F\mu_R + C_1)(2\sigma_{FR} + C_2)}{(\mu_F^2 + \mu_R^2 + C_1)(\sigma_F^2 + \sigma_R^2 + C_2)}$$

The variables C1 and C2 are utilised to stabilise the denominator where μ is average.

| 8. | Relative SD | [55][100] | Compute Standard deviation (SD) difference between fused and reference data and divided by the mean of the reference images.

$$\text{Rel. SDD} = \frac{\text{Standard deviation(Reference} -\text{Fused band)}}{\text{Mean MS}_{\text{band}}}$$ |

1.6.2.2 Comprehensive Assessment:

It is proposed that quality measures should not be the sole means of interpreting fused images. In a few applications, objective metrics analysis of an image with a low value may provide superior class accuracy. To enhance the assessment of the fusion outcome, the analysis may be built from the application perspective [75]. The fusion image may be assessed by comparing it to the various classification findings. Abdikan *et al.* (2015) [62] investigate the impact of fusion techniques on classification accuracies by comparing the Maximum Likelihood Classifier (ML), Support vector machines (SVM) and Random Forest (RF) as statistical models. Neetu and Ray (2020) [106] compared different fusion techniques and shows result visually, statistically, and through image classification for crops classification. Table 1.6 summaries the comprehensive assessment.

The research indicates that multi-source information from optical and SAR sensors can significantly improves the interpretation and classification of land cover types. It is evident that a combined use of optical and SAR images will have number of advantages because a specific feature, which is not seen on the passive sensor images may be observable on the microwave image and vice versa because of the complementary information provided by the source.

Table 1.5 Objective evaluation measures (reference data not required)

SN	measures	Reference	Points
1.	Entropy	[65][69][79][96]	Measure the information content of resultant.
		[101]	Entropy = $-\sum_{i=0}^{L-1} p_i \, log_2 p_i$
			L and p_i are the total number of gray levels and corresponding normalized histograms, respectively.
2.	SD	[55][79][96][101]	measure the contrast of resultant
			SD = $\sqrt{\sum_{i=1}^{M} \sum_{j=1}^{N}(F - \bar{F})^2}$
3.	MI	[103][104]	compare the resemblance of reference and fused images
			MI = $\sum_{R,F} H_{R,F}(r,f) \log \left[\frac{H_{R,F}(r,f)}{H_R(r)H_F(F)}\right]$
			Where $H_R(r)$ and $H_F(f)$ represent the histogram of MS image R and the fused image F. $H_{R,F}(r,f)$ denote joint histogram of MS and Fused image.
4.	SF	[101][105]	measures the overall activity level
			SF = $\sqrt{\sum_{i=1}^{M} \sum_{j=1}^{N}[\{F(i,j) - F(i,j-1)\}^2 - \{\{F(i,j) - F(i-1,j)\}^2\}]}$

Table 1.6 Evaluation of fusion image with classification accuracy

S. No.	Classification Method	References
1.	ML	[56][61][62][75][101][106][107][108]
2.	SVM	[56][62][108][109]
3.	Random Forest	[62][108][110][111]
4.	Fuzzy classification	[108][112]
5.	Neural Network	[56][113]

1.7 Research gaps

A lot of researches are being conducted to develop newer technologies and methodologies for detection of buried subsurface landmine in view of its implications on human life. Several new method and technology have also been evolved, however there is still a lot of scope for further research in this area. From the preceding discussion so far, it may be evident that surface and subsurface(buried) object detection through microwave remote sensing is a possibility but it entails several issues. For example, it is required to curtail the selection of objects of interest because of lack of availability of remote sensing data at a specified resolution, followed by a reasonable selection of detection techniques/models. In this research, landmines and landscape objects such as artificial structures, water bodies, and forests, have been consider for analysis.

Based on the Literature review, the following research gaps have been identified:

i. Most of the work reported in the literature utilizes data in individual microwave bands or individual polarizations [10][108][67][71]. Various research has pointed out that microwave data is more suitable for estimation of depth of subsurface buried landmines. The penetration depth of microwave data

depends on the frequency band [6][18]. It is also reported that wave polarisation shows the diverse features of objects [47][49][50]. However there appears limited work to utilize the combination of two or more frequency bands and polarisations of microwave data to improve object detection. There appears merit in the exploration of fusion of multiband multipolarization microwave data for buried object detection.

ii. The polarimetry SAR (PolSAR) data extracts surface, double-bounce, and volumetric scattering components. A lot of research has been reported to use the target decomposition theorem to detect manmade and natural objects. A common problem several researchers face is the cross-polarization power due to overestimation of one of scattering components [49]. Few works have been reported regarding this problem [48][114]. However, none of this works have utilized the combination of the respective dominant scattering components of two frequency bands. Thus, the Fusion of multi-band, multi-polarization SAR data appears to have scope in PolSAR decomposition for detecting artificial and natural objects.

iii. There is ongoing research in the fusion of optical and microwave data [110][111] [113]. However not enough research appears to have taken place to explore all the aspects of image fusion and their evaluation in natural and man-made object detection. It appears that improvement in fusion results is yet to be explored with comprehensive evaluation parameters.

iv. There are a several fusion algorithms reported in the literature. However, the selection and formulation of the appropriate image fusion algorithm for a particular application has not been carried out [75].

1.8 Research objectives

This research aims to explore the improvement in object (surface or subsurface) detection using the fusion of multiband, multipolarization microwave data. The specific objectives are:

(i) Detection of Subsurface Objects using Fusion of Multiband Multipolarization Scatterometer Data.

(ii) Improvement in detection of surface objects using fusion of multiband and multipolarization SAR data.

(iii) Improvement in detection of surface objects using fusion of optical and microwave data.

1.9 Organization of the thesis

The thesis has been divided into five chapters.

Chapter 1: Introduction

This chapter will expound the complete theoretical background of the research along literature review, research gaps, and objectives followed by layout of the other chapters.

Chapter 2: Detection of Subsurface Objects using Fusion of Multiband multipolarization Scatterometer Data

This section will contain the terminology, methodology adopted for First objective along with the detailed discussion of implementation steps required to accomplish this research objective followed by outcomes of the research.

Chapter 3: Improvement in detection of surface objects using fusion of multiband and multipolarization SAR data

This section will contain the terminology, methodology adopted for second objective along with the detailed discussion of implementation steps required to accomplish this research objective followed by outcomes of the research.

Chapter 4: Improvement in detection of surface objects using fusion of optical and microwave data

This section will contain the terminology, methodology adopted for third objective along with the detailed discussion of implementation steps required to accomplish this research objective followed by outcomes of the research.

Chapter 5: Summary of results, major contribution, and future work

This part will highlight the contribution with respect to individual objective. This will be based on the inferences of the results observed from each objective. Second segment will discuss about the limitations followed by future scope of the research.

Chapter – 2

Improvement in Detection of Subsurface Buried Objects using Fusion of Multiband Multipolarization Scatterometer Data

2.1 Introduction and problem definition

Several countries are affected by millions of buried landmines on their soil. These landmines have an extended lifespan and can cause catastrophic personal damage and economic disruption even after a battle has ended [15]. Landmines are exploding weapons with little to no metallic substance housed in tiny plastic canisters. They are designed to detonate upon pressure, incapacitating unaware enemies who step on them. Similar canisters are used against tanks and other vehicles rendering them inoperable as they pass over. These are referred to as antipersonnel (AP) or antitank (ATK) mines depending upon whether the target is a human/soldier or a tank/vehicle. Landmines are frequently placed flush at shallow depths to prevent quick visual detection and bypassing by enemy soldiers and tanks/vehicles. A metal detector is currently the most popular practical land mine detection tool. Unfortunately, this straightforward tool is barely helpful for finding non-metallic mines because most of them have no or very few metallic components.

Numerous novel approaches have been proposed and researched to address the issue of non-metallic mine detection [44]. They include various microwave-based methods (such as GPR), methods based on infrared imaging, chemical sensors, etc. However, these techniques are costly and unreliable, and necessitate working in proximity to buried landmines, making them extremely dangerous. On the other hand, microwave remote sensing-based approaches are less hazardous than land- or vehicle-

based methods since they can be designed to scan the earth's surface from a standoff distance [11][33]. A detailed review of existing landmine detection techniques has been presented in Section 1.4.

Microwave remote sensor operates by emitting short bursts of EM energy into the ground and detecting reflections that occur when the energy encounters change in permittivity and conductivity [115]. These reflections are crucial for landmine detection, as they reveal variations in dielectric properties at air-surface-landmine interfaces. However, a significant challenge arises when the dielectric contrast at the air-surface interface overlaps with that of the soil-landmine interface. This overlap results in weak and indistinct backscattered signals, making the detection of landmines difficult. The difficulty lies in extracting landmine features from the diminished backscatter response, primarily because the sensor is typically situated some distance from the buried surface, and the dielectric constants of the landmine and the surface soil are often within the same range. Consequently, the extraction of landmine features within the cluttered soil environment poses the primary challenge in microwave remote sensing for landmine detection [17][41][103]. To address this issue, researchers worldwide have developed several models and signal-processing algorithms that leverage microwave detection techniques to detect landmines accurately [14][18][117].

This challenge is exacerbated by soil clutter caused by surface parameters and internal inhomogeneity. Researchers have been actively investigating EM scattering due to surface parameters and inhomogeneity structure, recognizing its significance in landmine detection. Despite extensive research, EM scattering remains a highly complex phenomenon. Various researchers have conducted detailed studies on different aspects of

EM scattering and have proposed models that account for other surface conditions [18][118].

Considering a particular emphasis on dielectric permittivity, Takahashi *et al.* (2014) [119] proposed a straightforward technique to model clutter from soil heterogeneity. The research experimented on one soil type with varied levels of heterogeneity to validate the methodology before applying it to three soil types (Laterite, magnetic sand, humus) for landmine detection testing. In a blind test, the study revealed a significant correlation between the radar system's performance and the clutter modeled based on soil heterogeneity. Notably, the research underscored how soil heterogeneity can profoundly impact radar performance, particularly at higher frequencies, leading to an increased likelihood of misidentification.

In the context of landmine detection, the primary goal is not necessarily to achieve precise calculations of the backscattering coefficient. Instead, the focus lies on enhancing mine-like features within an image to effectively distinguish between the background and potential landmines. Consequently, the perspective shifts towards exploring alternative approaches that can minimize the adverse effects of surface parameters and accentuate various mine-like characteristics in the image. The overarching aim is to enhance the ability to improve the detection of landmines without the need for an exhaustive determination of exact scattering coefficients, aligning more closely with the practical requirements of landmine detection applications.

The microwave backscatter intensity depends upon target and system characteristics. This target characteristic encompasses dielectric constants, scattering properties, orientation, surface roughness, and shape. On the other hand, system characteristics encompass wave frequency, polarisation, and incidence angle, each of

which plays a distinct role in influencing the backscatter characteristics [18]. Together, these characteristics comprehensively determine the observed backscatter intensity, with each element contributing uniquely to the overall result [120][41].

The impact of surface roughness on buried object detection is a crucial consideration in fields such as geophysics, archaeology, and landmine detection. Smooth surfaces offer more predictable interactions with EM waves, potentially enabling greater penetration before encountering the buried object. On the other hand, rough surfaces scatter radar waves, resulting in reduced penetration depth and increased detection complexity. Moreover, variations in surface roughness within a detection area can add further complications [121]. While rough surfaces can pose challenges to detection efforts, it is imperative to comprehend these effects and employ appropriate detection technologies and processing techniques to ensure accurate and reliable buried object detection across diverse real-world scenarios.

In the study by Chmielewski *et al*. (2007) [122] introduces a two-step EM detection method for identifying buried objects, focusing on AP landmines in natural soil. It addresses surface clutter by estimating the roughness profile of the interface, an unknown parameter. The procedure effectively reconstructs surface profiles amid noise, emphasizing the importance of the estimated roughness profile in the inversion process.

The polarization information in the backscattered waves from a specific target plays a crucial role in delineating its geometric structure, orientation, and physical characteristics. This, in turn, significantly influences how a radar system perceives the object within its environment. It follows that manipulating the polarimetric response of a subsurface scatterer can either amplify or diminish its visibility [123]. Data in particular

polarisation do not have adequate discrimination capability, but each polarisation enhance diverse features of object. Numerous studies have showcased the effectiveness of utilizing information across various polarizations for detecting man-made targets amidst backgrounds characterized by natural clutter [18][60][124] [125].

Information obtained from two different polarizations provides an extra discriminant, enhancing the ability to differentiate and analyze data effectively. Consequently, scenes captured in orthogonal polarizations (such as VV and HH) exhibit variations in the intensity of detected backscatter contingent on the relative smoothness of targets within the scene. Moreover, it has been observed that smoother surfaces tend to display a higher ratio value for the difference between data in two polarizations (HH and VV) and their sum. This ratio has been applied in retrieving soil moisture in microwave X-band [126], demonstrating its effectiveness in mitigating the impact of roughness. The utilization of data across multiple polarizations also furnishes ample information for characterizing scattering mechanisms originating from diverse sources [127]. Despite this, exploring data from different polarizations for enhancing the detectability of buried targets, such as landmines, by minimizing surface effects still needs to be explored. The ultimate purpose is to evolve a model that takes input data in multiple polarisations and combines them into an image array capable of highlighting desired mine-like features.

The height deviations from the wavelength are compared to determine if a surface is smooth or rough. A single surface can be classified as rough or smooth depending on which microwave band is in question. Considering that wave penetration rises with wavelength. As seen in Fig. 2.1, there is also less backscattering and the surface appears smooth. However, the surface seems rougher at low wavelengths due to significant backscattering.
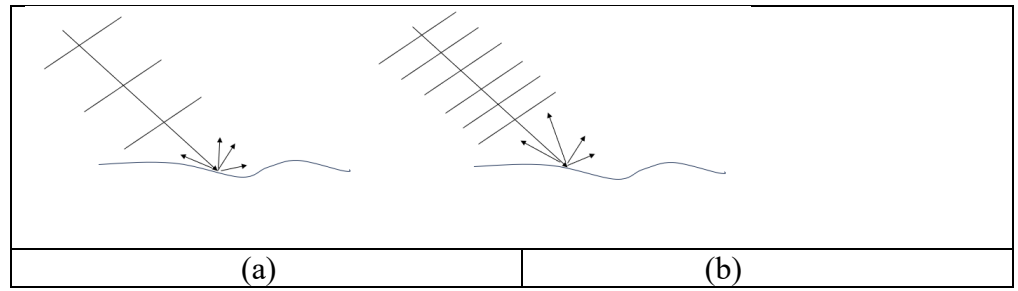
Fig. 2.1 Same surface appear (a) smooth for higher wavelength, and (b) rough surface for lower wavelength

The choice of microwave frequency band (such as L, S, C, X) in landmine detection impacts factors like penetration depth, resolution, sensitivity to environmental conditions, and equipment complexity [18]. It involves trade-offs, with lower frequencies penetrating deeper but offering less resolution and higher frequencies providing better resolution but requiring more sophisticated technology [128]. Multiband processing is sometimes showing significant improvement in landmine detection. In the paper [129], the Estatico *et al.* (2015) have extended an EM inverse scattering technique originally designed for single-frequency imaging to incorporate multifrequency processing. To validate this approach, the researchers conducted numerical simulations to reconstruct cylindrical scatterers within a homogeneous lossy medium. These simulation results were subsequently compared to outcomes achieved through standard single-frequency operating conditions.

A further concern in this context is the assessment of the minimization of surface roughness. Since there is limited literature exploring the data in multiband multipolarization to minimize surface roughness effects, no models or metrics are available to assess surface roughness minimization. However, surface roughness effects can be treated as the existence of uncertainty present in the image, preventing landmine discrimination from the background. The presence of error, inexactness, fuzziness, or

ambiguity within an image is denoted as uncertainty. Consequently, diverse measures of uncertainty can be employed to evaluate the impact of surface roughness effects. Within the array of uncertainty metrics, entropy measures, including log-energy entropy or different variations of entropy manipulations, are recognized as appropriate indicators of random effects in an image. They hence can be used to assess surface roughness minimization effects [130].

Conducting a comprehensive analysis of data acquired through various multiband and polarization channels is expected to play a pivotal role in the near future, particularly in the context of minefield detection methods employing UAV drones or satellite-based technologies [6]. The objective of this is to investigate the capability of C- and X-band microwave SCAT data, specifically in the VV and HH polarizations. The objective of this research is to explore synergistic approaches to enhance the effectiveness of landmine detection through minimization of surface roughness.

The research aims to achieve the following specific goals:

- To develop a framework to improve landmine detection by mitigating the impact of surface roughness.
- To evaluate the discrimination capability of VV and HH polarization and their fusion combination for improving buried landmine detection.
- Exploring the discrimination capability of multiband (C- and X- band) SCAT microwave data for buried landmine detection.

2.2 Data Set Description

As discussed in chapter-1, a SCAT is a complex instrument comprising several components that measure backscattered microwave radiation and derive valuable information about surface properties. A SCAT microwave system has been developed and

utilized for all the experiments of this research. Fig. 2.2 shows the SCAT experimental setup in the open field environment. A horn antenna and power meter are attached to a microwave transmitter through a circulator. An isolator with a 35-decibel isolation has produced an empirical dataset and polarizations. For the purpose of burying of mines, a wooden box sized 120x120 cm has been built and filled with dry sand. Microwave antennae has a base height of 100 cm from the ground. This arrangement can drive the antennas in both the horizontal and vertical directions. The horizontal stripes have been inscribed in 5 cm increments from 1 to 24 (Fig. 2.3). The antenna and circulator undergo lateral movement along the Y-axis, ranging between position 1 to 24, at each horizontal point along the X-axis, position between 1 to 24. The experiments have been carried out in the open ground exposed to sunlight.
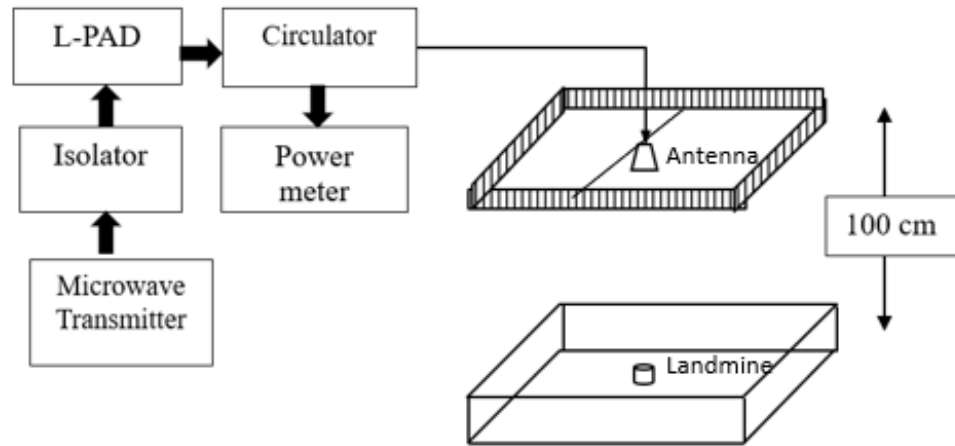
Fig. 2.2 Block diagram of SCAT system (L-PAD: min. loss matching pad)

This study focuses on a live antitank (ATK) landmine that, although lacking a fuze, still has explosive material. This mine is deliberately buried at the central point of the configuration under investigation. The design parameter of experiments is given in Table 2.1. All the measurements of these experiments have been collected in far-field regions (Fig.2.3). A wooden profilier is used to vary the soil surface roughness from 1cm to 5 cm as shown in Fig. 2.3 (a), (b) and (c).

(a) open-field SCAT experimental setup
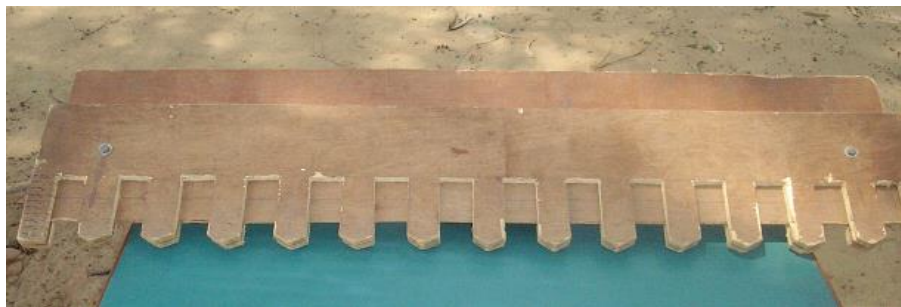
(b) indigenous wooden profiler

(c) rough surface - 2 cm

(d) rough surface – 3cm

Fig. 2.3 SCAT setup with wooden profiler [131]

A Live antitank has been placed at the center of experimental setup. Fig. 2.4 shows the dimension of live antitank mine. Table 2.1 summaries the design parameter of this study. This live landmine data has been taken from Indian Institute of Technology, Roorkee [131].

Fig. 2.4 Live Antitank Mine (weight:7 kg, height:0.07m, length: 0.25m, and width: 0.25m)

Table 2.1 Design parameters of Experiments

Design Parameters	Details
Frequency Band	C- and X band
Polarisation	VV and HH
Soil composition	Dry sand
Surface Texture	Smooth and Rough Surface
Surface roughness depth	1,2,3,4, and 5 cm
Mine placement	Buried at the central point
Type of Landmine	Live antitank Mine

2.3 Theoretical framework/model: methodology

Anti-tank mines come in multiple dimensions and shapes and can be encased in plastic, metal or wood. While microwaves have a relatively good penetration capability compared to other parts of the EM spectrum, the actual depth of penetration depends on the wavelength and condition of the object involved, such as the moisture content of the material, the density and composition of the material, and the roughness or texture of the

surface. Materials with high water content, such as wet soil or human bodies, can absorb and attenuate microwaves more effectively, reducing their penetration depth.

SCAT emit microwave pulses towards the Earth's surface and measure the backscattered radiation. The scattered signals contain information about the surface roughness and soil moisture. By analyzing the characteristics of the backscattered signals, SCAT can estimate the shape and range of buried object. Ground-based SCAT can be customized and optimized for specific research or application needs. The instrument parameters, such as the frequency, incidence angle, and polarization, can be tailored based on the desired measurements and the characteristics of the target environment. This flexibility allows for more focused and specialized observations [18].

The SCAT system consists of the components: Transmitter, antenna, receiver, oscillator, signal processor and data acquisition system. The polarization parameter of a SCAT refers to the polarization state of the transmitted and received microwave waves used in the measurement process. It characterizes the orientation and alignment of the electric field vector of the EM waves. The SCAT transmits and receives EM waves in Vertical and Horizontal polarization. By transmitting and receiving microwave signals with different polarizations, SCAT can analyze the backscattered radiation and extract information about surface properties. The polarization characteristics of the backscattered signals can reveal details about the surface roughness, soil moisture, and other parameters of interest. Polarization measurements provide additional information about surface characteristics, enabling more accurate retrievals and improved discrimination between different surface types [116].

Based on a critical literature review and observation, a theoretical model has been presented in this section for improving landmine detection using SCAT data. The

proposed landmine detection model comprises five essential steps. The landmine feature extraction is the first step, relying on image processing methods.

Segmentation of a suspected area having a landmine after raw data preprocessing is the first step. Data preprocessing encompasses several image processing techniques that refine raw data, simplifying the extraction of the desired attributes from the resulting image. The efficient implementation of landmine feature extraction has been proposed for reducing false alarms. The second step involves a theoretical model for factors affecting backscatter from a landmine. The theoretical analysis would lead to minimizing the factors adversely affecting the landmine detection. Further, an approach to minimize affecting factors roughness has been proposed in the subsequent step. The data fusion approaches have been utilized as a prominent component for obtaining the desired outcome. Finally, the model has been evaluated through a rigorous evaluation parameter, followed by another validation using signal processing algorithms. Here, X- and C-band SCAT data of live antitank landmine has been taken for study. The landmine is buried under rough and dry sand at roughness depths of 1,2,3,4 and 5cm. Fig. 2.5 summaries the proposed theoretical model.

2.3.1 Landmine Feature Extraction: Image Preprocessing and Segmentation

An advanced image processing technique is proposed to extract significant features related to the buried landmines from raw image data generated from the SCAT system. The extraction consists of two significant subtasks: image preprocessing and segmentation. The primary objective of this step is to classify SCAT data into landmine-like or non-landmine-like, which further reduces the false alarms.

Landmine Feature Extraction: Image Preprocessing and Segmentation	For reducing false alarm through increasing Signal to clutter ratio
Parameters affecting backscatter	
Selection of parameters to be minimised	
Proposed approach for minimise the parameters	Theoretical framework for improvement in buried object detection
Evaluation and also validation of proposed approach through signal processing analysis to assess the improvement in buried object detection	

Fig. 2.5 Proposed Theoretical framework

2.3.1.1 Image Preprocessing

The monostatic SCAT system received backscatter power as linear convolution of impulse responses (of antenna, clutter, and landmine) with transmitted power [18]:

$$P_R(\text{i}) = P_T(i) * h_A(i) * h_C(i) * h_L(i) * h_C(i) * h_A(i) \tag{2.1}$$

Here, $h_A(i), h_C(i)$ and $h_L(i)$ are impulse responses of the antenna, clutter, and landmine, respectively, whereas $P_R(\text{i})$ and $P_T(i)$ are the received and transmitted power by the SCAT antenna. The Landmine impulse response is calculated by deconvolution of the received signal. Here, clutter reduction and its modelling are complex tasks.

The preprocessing of SCAT backscatter requires the primary signal processing tasks:

i. Calibration

A calibration was performed on raw data using a ratio with a perfect reflector such as aluminum (reflectivity coefficient »1). An aluminum plate measuring the dimensions of the wooden sand frame has been laid down on the sandpit, and the backscatter value has been recorded. Calibration of raw data has been calculated from the following equation:

$$E_{calibrate} = \frac{E_{observe}}{E_{AL}} \qquad (2.2)$$

Where $E_{observe}$ is received observed backscatter value, whereas E_{AL} is backscattered power received from aluminum metal.

ii. Normalization

Normalization brings all the data in the same range. The following equation would calculate the normalization of the calibrated data:

$$E_{normalise} = \frac{E_{observe} - E_{minimum}}{E_{maximum} - E_{minimum}} \qquad (2.3)$$

Here $E_{maximum}$ and $E_{minimum}$ are the maximum and minimum backscatter values.

iii. Deconvolution

At the SCAT antenna receiver, deconvolution has been performed on normalized data. The specific choice of filter for this deconvolution step is intricately linked to the configuration and settings of the SCAT parameters [132]. A Convolution kernel filter has been applied to reduce the impact of scattered field overlap from adjacent pixels. It has been observed that the 5×5 convolution filter performs better for the X- and C-band SCAT systems.

$$W_{3\times3} = \begin{bmatrix} 1 & 1 & 1 \\ 1 & 2 & 1 \\ 1 & 1 & 1 \end{bmatrix} \qquad (2.4)$$

$$W_{5\times5} = \begin{bmatrix} 1 & 1 & 1 & 1 & 1 \\ 1 & 1 & 2 & 1 & 1 \\ 1 & 2 & 3 & 2 & 1 \\ 1 & 1 & 2 & 1 & 1 \\ 1 & 1 & 1 & 1 & 1 \end{bmatrix} \qquad (2.5)$$

The kernel deconvolution filter of window size 3×3 and 5×5 has been shown into equation 2.4 and equation 2.5.

The physical size of a landmine is generally tiny, so the backscatter received from the buried landmine appears to be stretched over just a few pixels. As a result, two separate methods, full-frame and local-frame processing, have been evaluated. The SCAT system generated data within a 24x24 image elements frame, as discussed in Section 2.2. and this raw data is subsequently preprocessed in both full-frame (24x24) and local-frame(8x8) configurations to enhance the extraction of the landmine feature.

2.3.1.1.1 Full-frame Preprocessing

The complete raw data, which comprises a 24x24 matrix, is processed through a sequence of data preprocessing steps as previously outlined. The full-frame processing allows for analyzing the raw backscatter image without involving additional image manipulation tasks. One benefit of this approach is that it provides insight into the characteristics of the original data.

This full-frame preprocessing can occur because the preprocessing steps, such as filtering or normalization, could smooth or normalize the data, reducing the contrast between the landmine and its surroundings. Nevertheless, when dealing with buried landmines, where the backscatter from the landmine might not exhibit notable distinctions from its surroundings, full-frame processing could potentially result in the absence of critical landmine attributes.

To address this limitation, researchers should take additional considerations into account. For instance, alternative approaches involve localized analysis or focusing on specific regions of interest rather than applying preprocessing to the entire image.

Targeting specific areas where the landmine is expected to be present makes it possible to preserve and enhance the relevant features associated with it, even if the overall contrast in the image is low.

2.3.1.1.2 Local-frame preprocessing

Separating landmine-like attributes from non-landmine-like attributes in a heterogenous environment is necessary for landmine feature extraction. The formation of clutter in landmine detection can be attributed to several factors, including differences in dielectric properties at the interfaces between various materials, surface irregularities, and the small size of the landmines themselves. The limited variations in dielectric properties between the landmines and the surrounding medium also contribute to this issue. Processing in a local-frame may be more beneficial to identify pixels with landmine-like properties because the landmine backscatter in a SCAT measurement is typically localized to a small number of pixels alone. The local-frame processing can be implemented by generating the new image, dividing it into frames, transferring the frames, and applying data preprocessing steps. Table 2.2 exhibits the implementation steps for local-frame processing.

Table 2.2 Implementation steps for local-frame processing

Step 1: Generate a new image
• Create an identity(I) matrix of 24x24 size as the raw data.
• Multiply the identity matrix by the raw data's mean backscatter value.
• Visualize the new data as a 3D plot, resulting in a plot where all data points lie on the same plane at a constant value, which is equal to the mean backscatter value.

• Scale down the new image by multiplying it with a fraction between 0.5 and 0.8. The precise value of the fraction is determined through the analysis of each experiment.
Step 2: Divide the raw image into frames
• Determine the optimal frame size based on landmine size, potential presence of other targets, and clutter.
• In this case, an 8x8 pixel frame size is suitable because of the size of the target (landmine).
• Divide the raw image into non-overlapping blocks of the chosen frame size.
Step 3: Process each frame in the new image
• Iterate over each frame in the raw image.
• Transfer the frame to its corresponding location in the newly framed image.
Step 4: Perform data preprocessing steps on the new image
• Apply various image processing methods outlined earlier to enhance the image for landmine detection
Step 5: Repeat steps 3 and 4 for all windows in the raw image

2.3.1.2 Segmentation

Image segmentation is necessary for object detection to precisely locate and identify objects inside an image [133]. Dividing the image into several zones provides pixel-level masks that help define object borders and handle occlusion. Other benefits of segmentation are getting rid of unnecessary data, separating foreground from background elements, and reducing false positives. An image is segmented as a stage towards extracting a desired object or region. Depending on the application's requirements, level

subdivision should finish once the object of interest has been isolated. Extracting the pixels that make up the landmine is necessary for landmine detection, but they might need to be more readily available for various reasons. However, it might be conceivable to outline and divide a zone as closely as possible to the area the landmine covers. Thresholding can be used for automated segmentation of a suspected minefield-containing zone, although this method calls for selecting a threshold value, such as 't' [134]. Selecting an appropriate threshold value, 't,' remains a daunting task, primarily since the landmine features within the data occupy a limited number of pixels and are further complicated by the potential overlap in backscatter intensities between the landmines and their immediate surroundings. Pare *et al.* (2020) [135][136] classified different thresholding approaches. The segmentation of images and thresholding approaches for image analysis are covered in Goh *et al.* (2017) [137]. This research examines the viability and effectiveness of the Otsu approach for image thresholding under different environmental conditions. The investigation results demonstrate that object position has no discernible impact on segmentation performance but that the intensity difference, object size, and noise level are the main factors that determine the effectiveness of image segmentation. Additionally, a verification utilizing real-image data is included in the research to show that the proposed conditions may correctly predict the image thresholding outcome. One clustering-based approach (Otsu thresholding [138]) has been selected for further data processing of SCAT data. Its goal is to select the appropriate threshold value that maximizes variance across the classes while minimizing variance within each class.

The convoluted data has been subjected to thresholding using Otsu's methods for identifying a suspected region buried with a landmine. The segmented region is expected

to contain the landmine, and the backscatter values in this region have been considered for further analysis

2.3.2 Parameters affecting backscatter from landmine

The value of SCAT backscatter is subject to system parameters (incident angle, frequency band, and polarisation of microwave data) and target parameters (surface roughness, scattering phenomena, and dielectric constant). Among these system parameters, incident/viewing angle is fixed for the experiments. The system parameter that significantly adds to the information in the backscatter are the frequency band and polarization state of microwave data.

(i) Scattering mechanisms

Scattering mechanisms refer to how EM waves interact with surfaces, particularly how they are reflected or dispersed by rough and smooth surfaces. EM waves scatter from rough surfaces in various ways due to the imperfections and microstructures these surfaces possess. The two primary scattering mechanisms connected to rough surfaces are: Lambertian and Bidirectional reflectance. A lambertian surface is an ideal diffuser since it scatters EM waves evenly in all directions. Regardless of the incidence angle, wave is equally reflected in all directions when it hits a lambertian surface. These surfaces are simpler to model and analyse due to their predictable dispersion behaviour. The bidirectional reflectance scattering on real-world rough surfaces is not always uniform. Instead, they have different reflectance characteristics depending on the angle of incidence and observation. It describes the various angles at which an EM wave is scattered or reflected by a surface. On a rough surface, the energy scatters evenly in all

directions, with a large amount returning to the radar. It causes radar images of rough surfaces to seem lighter.

Smooth surfaces, commonly referred to as specular surfaces, have a low degree of surface roughness, which produces more consistent and predictable reflection patterns. The primary scattering mechanisms connected to smooth surfaces is specular scatter. Smooth surfaces with some roughness but imperfect secularity is called glossy surfaces. Another wave scattering, known as volume scattering, results from independent elements of the medium if microwave radiation passes through the top surface of any objects (such as vegetation). The scattering of microwave energy within a volume or medium is known as volume scattering, and it typically entails many bounces and reflections from various components within the volume. The image's brightness may drop or rise depending on how much energy is reflected in the SCAT during volume scattering.In many situations, the behaviour of a surface can vary between smooth and rough, and this variability is contingent on the frequency band of the incident waves.

(ii) Multi-layer surface effect

Microwave propagation under the surface (sand) involves the interaction of multilayer surfaces, and air-sand-landmine interfaces have been used in these experiments. Fig.2.6 shows the schematic representation of multilayer microwave propagation for buried landmine detection.

The landmine is buried under dry sand at the depth of 'H'. Here E_i is the incident electrical field transmitted from SCAT, and E_R is the total backscatter signal received by SCAT. The backscatter available at the SCAT from a subsurface

landmine is on-linear integration of all the reflections, received clutters from multilayer interfaces, and scattering components. The E_R received from scattering by the landmine-sand-air layers, reflection from the landmine, diffraction, and specular and volume scattering. The backscatter signal, as it is received, multiple layers, with each layer being distinguished by its unique dielectric constant. Which further limits the detection of buried landmine detection.
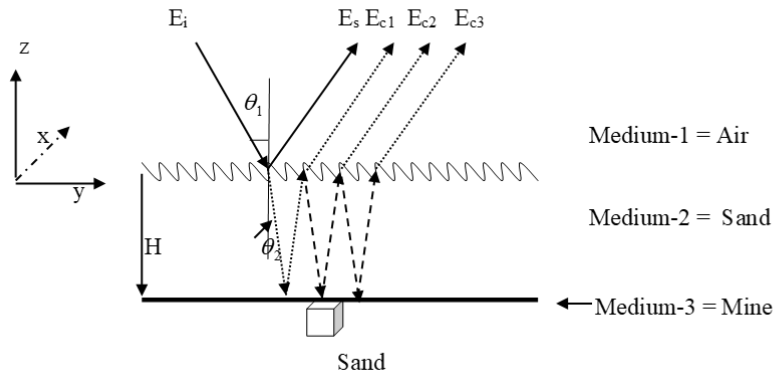
Fig. 2.6 Multilayer wave propagation and reflection in an air-soil-landmine interface

(iii) Surface roughness

The target's surface roughness is made up by numerous small scatterers distributed across its surface. The quantity of backscatter accessible at the SCAT end is often primarily determined by the surface roughness. It regulates the interaction between the target surface and microwave energy. Surface roughness is described by root mean square (rms) height, which is represented in terms of EM wavelength.

The statistical fluctuation of the random components of surface height in relation to the reference surface is described by the surface height standard deviation. A surface is categorized as "rough" when its height variances surpass

the wavelength, while it is classified as "smooth" when these variances do not exceed the wavelength. Surface roughness depth is another name for this RMS height. However, Charlton *et al.* (2006) [139] provide the surface roughness for both smooth and rough surfaces mathematically.

Rough Surface:

$$h > \frac{\lambda}{4.4*\sin \alpha} \qquad (2.6)$$

Smooth Surface:

$$h < \frac{\lambda}{425*\sin \alpha} \qquad (2.7)$$

where h = height of surface roughness, λ= wavelength, α=grazing angle.

In general, it has been observed that surface roughness increases the backscattered intensity. In an S-band image with a wavelength of 7.5 to 15 cm, it seems dark when the surface roughness is of the order of 5 cm, but in an X-band image with a wavelength of 2.4 to 3.75 cm, the same surface appears bright due to increased backscattering [18].

(iv) **Wave Polarisation**

SCAT antenna usually transmits plane-polarized radiation. Its associated electric field oscillates in a single plane perpendicular to the direction in which the wave propagates. The electric field of the transmitted/received wave oscillates in the vertical or horizontal plane depending on how the antenna parameters are designed. The oscillations of the transmit and received waves can lead to several polarization mode combinations. In this experiment, the polarization modes used are VV and HH, with the transmitter and receiver being polarized vertically and

horizontally, respectively. Co-polarized waves share the same polarization in both the transmitting and receiving directions. Due to the instrument's power limit, this research did not consider cross-polarization mode (VH and HV). The backscatter value differs in different polarization and depends on the target orientation and incidence angle. The nature of the data collected in the various polarizations is very diverse, and the necessary landmine-like attributes might be embedded in either of the polarizations or extracted by combining them using a suitable approach.

Most scattered energy, typically accessible at the SCAT end, has the same polarization as the transmitted wave when a polarized wave is scattered by a rough surface like soil. The wave is repeatedly scattered at the interfaces of the two mediums, the air, and soil, when it passes through a surface, leading to a significant depolarization. Both horizontally and vertically transmitted waves incur varying degrees of depolarization [140]. Additionally, the levels of penetration are varied for waves with various polarizations. For instance, co-polarized (HH or VV) waves typically penetrate much further than cross-polarized (VH or HV) waves [120]. Depolarization thus varies depending on the polarization type, scattering, and penetration. Therefore, the microwave data gathered in various polarizations contains noticeably varying amounts of information about the target since the received polarization may differ from the transmitted polarization. Similar to this, depending on the smoothness of the surfaces, a scene captured in two orthogonal polarisations exhibits fluctuations in the intensity of observed backscatter. According to research by Singh D. *et al.* (2005) [126], the polarization discriminant ratio, which compares the differences in data between two polarizations, is typically higher for smooth surfaces.

The backscattered wave can contribute to horizontal and vertical polarizations when a horizontally polarized wave strikes a target. A wave that is incident vertical is subject to the same rules. Therefore, each transmitted wave generates a different backscattered wave based on the target properties. As a result, the target response can be calculated from the microwave data in two polarizations utilizing two orthogonal polarizations, commonly VV and HH [141].

2.3.3 Selection of parameters to be minimised

As already mentioned, the SCAT system's target and system parameters determine the backscatter intensity in microwave data. Most landmine detection techniques use dielectric differences between a landmine and its surroundings. Due to surface abrasion, dispersion, layered media, and other factors, these restricted variations are likely to suffer. As a result, all effects that reduce the return from the landmine, create a loss of dielectric fluctuations, or could lead to false alarms must be removed and are referred to as undesirable effects. Due to the complexity of mechanisms resulting in diminished backscatter, it takes work to model or eliminate their effects. Table 2.3 shows the dielectric constant value and surface roughness for X-band microwave data. It may be possible to minimize some of the effects. In the following subsections, an overview of the undesired effects which need to be minimized is discussed.

Table 2.3 Experiment parameter in X-band ($\lambda = 3$ cm, $\alpha = \pi/2$) data

Dielectric Constant	
Air	1
Dry sand	3 to 5
landmines	4 to 10
Surface roughness(cm)	
Smooth surface	h < 0.12
Rough Surface	h > 0.68

Multi-layered propagation effect

A smooth surface generates specular reflections, whereas a rough surface scatters equal refection in all directions [11]. The backscatter wave reflected from the buried landmine passes through multiple layers of distinct dielectric constants. EM wave propagation through different layers to and from buried landmines has been shown in Fig. 2.6, which shows the multiple interactions at the medium interfaces. The backscatter available at the SCAT from a subsurface landmine is non-linear integration of all the factors mentioned with multilayer scattering.

Daniels J. *et al.* (2003) [115] introduced a model for estimating the electric field reflected from a target buried beneath a smooth surface has been adopted to estimate the backscattered electrical field from subsurface landmines buried under smooth surfaces.

Analyzing surface scattering and the multi-layered propagation effect is necessary for subsurface landmine detection, as mentioned in earlier section. Landmine detection will benefit from an accurate calculation of backscatter under these conditions, however modeling different components of scattering and the multi-layered propagation effect may be difficult and complex. On the other side, it is feasible to enable discriminating between the buried landmine and the background leading to its identification by reducing surface roughness and boosting landmine-like features.

The backscattering coefficient $\sigma(\theta_i)$ of a surface(smooth/rough) can be represented in terms of dielectric and roughness function [18]. The mathematical representation of $\sigma(\theta_i)$ is shown in equation 2.8.

$$\sigma(\theta_i) = F_{rt}(\epsilon_s, \theta_i) * F_s(\rho(\xi), \theta_i) \qquad (2.8)$$

Where θ_i denotes the incidence angle. The dielectric function $F_{rt}(\epsilon_s, \theta_i)$ explains the backscatter coefficient's dependence on the surface's relative dielectric constant. The

roughness function $F_s(\rho(\xi), \theta_i)$ explains the surface roughness dependence of the backscatter coefficient.

However, equation 2.8 only considers surface roughness and ignores the multilayer propagation effect. The difference between the theoretical and observed backscatter can be explained by scattering at the surface and the multilayered propagation effect, which are parameters represented by the undesired effects parameter. The backscattering coefficient can also be expressed according to dielectric constant of different media.

$$\sigma(\theta_i) = F_{rt}(\epsilon_1, \epsilon_2, \epsilon_3, \theta_i) * U_{effects} \tag{2.9}$$

$F_{rt}(\epsilon_1, \epsilon_2, \epsilon_3, \theta_i)$ is the dielectric function that includes the dielectric constants of air-soil-landmine multilayered interfaces. $U_{effects}$ is a factor that includes all the parameters that may affect the backscatter value at the SCAT system. As surface roughness is dominating factor, so these are known as surface roughness effect. Therefore, the purpose of the research that follows is to investigate various approaches and provide a model to reduce all undesirable impacts and improve landmine attributes.

2.3.4 Fusion approach of multipolarization data

The σ^0_{VV} (VV polarization backscatter value) and σ^0_{HH} (HH polarization backscatter value) polarization data in radar tell us about a target's shape, orientation, and composition by revealing how it interacts with radar waves of different polarizations. The dielectric properties of the target material play a vital role in this interaction. In essence, these data help us "see" and understand the physical characteristics of targets. Data from a single polarization in radar can be effective in detecting objects resembling landmines, especially when they are buried beneath smooth surfaces. However, when these landmine-like objects are hidden under rough or uneven surfaces, it becomes challenging

to identify or emphasize them, even after applying image preprocessing techniques. This difficulty arises from the adverse effects of surface roughness, as explained in the previous section. This further encourages combining or fusion of the σ_{VV}^o and σ_{HH}^o data may be better suited to reduce the effects of surface roughness.

As mentioned in Section 1.6, Fusion is merging or combining two or more data to achieve the desired response using some transformation and manipulation. The fusion of multipolarization data may also involve polarization subtraction and ratioing. The significance of polarization image subtraction and ratioing lies in their ability to suppress certain information while highlighting others. However, whether this leads to the enhancement of landmine-like features remains to be explored. Polarization discrimination ratio (PDR) is another popular image transform that has produced good results in soil moisture estimation in microwave remote sensing [126]. PDR can enhance specific concealed information that otherwise may not get improved. Thus, three primary polarization fusions approaches have been considered in the present chapter i.e., Polarization Ratio (σ_{VV}^o /σ_{HH}^o), Polarization Subtraction (σ_{VV}^o -σ_{HH}^o), and PDR ((σ_{VV}^o - σ_{HH}^o)/(σ_{HH}^o+σ_{VV}^o)).

The data from each polarization has been meticulously processed through well-defined steps, as depicted in Fig. 2.7. This comprehensive preprocessing included calibrating the raw data, applying normalization techniques, and conducting convolution operations. The VV and HH data has been preprocessed and evaluated to identify a suspected region separately and then subjected to various fusion approaches. The process of fusion of polarization data is subsequently carried out on the convoluted data across all depths, and a thorough and detailed analysis has been performed.

2.3.5 Assessment of surface roughness minimization

The undesired effects in equation 2.9 can be modelled as uncertainty in an image. The uncertainty usually refers to an image's error, inexactness, fuzziness, and ambiguity. From information theory, uncertainty arises out of randomness and fuzziness is modelled using entropy model. Surface roughness effects can be measured by extending these entropy measurements. Entropy measures randomness, uncertainty instability, fuzziness, imbalance system disorder, etc. For a random variable X with N available events $x_i \in \{x_1, x_2, ..., x_N\}$ with corresponding probabilities $p_i \in \{p_1 ... , p_N\}$; its Shannon entropy H(x) is:

$$\text{Entropy} = H(x) = -\sum_{i=1}^{N} p_i \log(p_i) \tag{2.10}$$

In this chapter, Shannon log energy entropy has been employed as a metric for the reduction of surface roughness [130].

2.4 Implementation of Proposed model

The experimental data, as discussed in Section 2.2 earlier, has been acquired in C- and X-band with VV and HH polarizations. Implementation and analysis discussed in this section follows the theoretical framework proposed in the Section 2.3. The implementation model consists of two stages. Landmine feature extraction using image processing approaches is the first stage of the implementation. The second stage improves the probability of landmine detection in multipolarization data by minimizing surface roughness through numerical fusion and evaluating using entropy measures. Fig. 2.7 depicts a flow diagram summarizing a set of image processing procedures defined for execution. Data preprocessing has been done in two ways: full-frame and local frame-based preprocessing. In each instance, surface roughness minimization has been evaluated using an entropy-based approach after getting the transformations and

segmenting landmine-like features. Complete implementation of this chapter has been performed using MATLAB software.
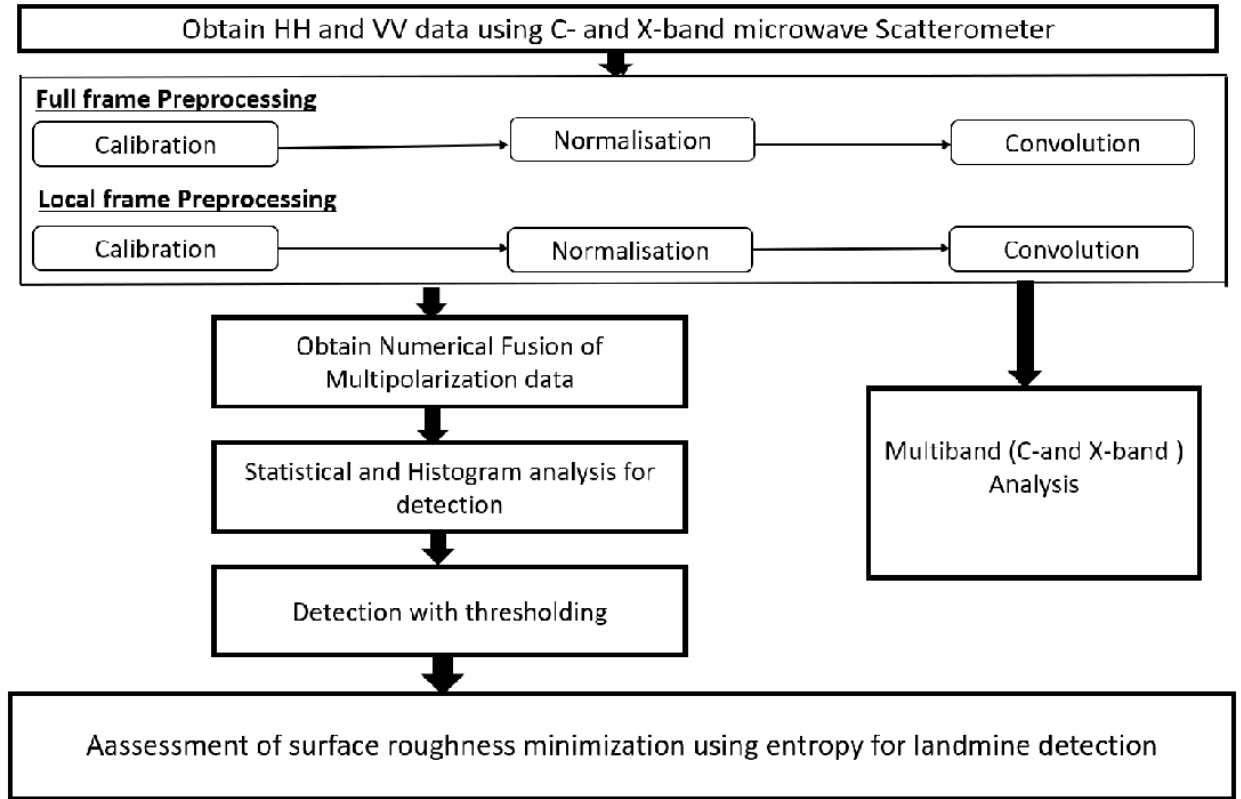
Fig. 2.7 Flow chart of this chapter

2.5 Results and discussion

Improving the detection of buried landmines can be achieved by minimizing the parameters that affect the backscatter value of the landmine. Based on the discussion about the theoretical model (Section 2.3), it is considered that surface roughness is one of the crucial parameters affecting backscatter from a buried landmine, making its detection challenging. In this section, analysis has been carried out to evaluate surface roughness effects. Data produced in VV and HH have been subjected to multi-polarization fusions and fusion approach for enhancing the detection has been proposed. Multi-polarization

fusion analysis has been done with X-band SCAT data under smooth and rough surface conditions. The performance of approaches has been evaluated through data entropy.

2.5.1 Effect of surface roughness (smooth and rough)

Surface roughness is one of the system parameters affecting the detection of landmines, discussed in section 2.3, and taken as an important element of this research work. Table 2.4 shows statistics assessing data generated by the X-band SCAT system under two distinct surface conditions: smooth and rough soil. Fig. 2.8 shows the visual representation of the data at a surface roughness depth of 1cm. The statistics directly provide valuable insights into the interaction of EM waves with both smooth and rough soil surfaces, enabling a better understanding of the scattering behaviour under these conditions.

The evaluation of statistics parameters exhibits the following consequence:

(i) The backscatter in VV polarisation (σ_{VV}^o) for smooth surfaces has been found to be higher than the HH polarisation (σ_{HH}^o).

(ii) Rough surfaces have higher backscatter values in both HH and VV polarization, and this difference becomes greater as depth increases for both polarisations.

(iii) The difference in backscatter between rough and smooth surface has also been found to be comparatively higher for VV polarisation. The standard deviation has, however, been found to be lesser in the case of rough surfaces in both polarizations when compared with the smooth surface. Still, the standard deviation in VV polarization has always been higher than that of corresponding (*i.e.,* smooth/rough surface) HH polarization. It indicates a loss of smaller backscatter values in favour of higher ones. This results in the loss of certain discriminating features in the case of rough surfaces,

which are essential in subsurface landmine detection because mine features are likely to appear as slight variations in backscatter values due to limited dielectric contrast between sand and landmine. It makes the task of landmine detection extremely difficult.

Table 2.4 Statistics assessment for live ATK landmine under smooth and rough surface condition

Statistics	Smooth Surface				Rough Surface			
	VV		HH		VV		HH	
	Raw	Deconvol	Raw	Deconvol	Raw	Deconvol	Raw	Deconvol
Min	10.40	1.25	8.40	0	13.50	2.11	9.90	0.87
Max	21.90	18.62	16.10	6.00	19.88	16.06	14.30	18.23
Mean	14.55	7.93	11.47	0.73	15.41	7.93	14.51	6.53
Skewness	1.34	0.93	0.46	2.61	0.45	0.70	1.26	1.07
Kurtosis	4.92	3.58	4.85	3.10	3.07	2.22	4.19	4.09
Std Deviation	2.01	3.39	1.32	1.10	1.08	3.24	0.86	3.32

(iv) The statistical moments, skewness and kurtosis are known to be outlier sensitive and hence may help indicate the presence of landmine in the data. Positive skewness suggests that the data exhibits a rightward skew. There is no change in the direction of skewness in both cases, i.e., smooth, and rough surface conditions, but the value changes marginally. On examining skewness at different depths, no pattern is observed. Similarly, no pattern is noticed in the case of kurtosis when the same is examined at different depths. A similar statistical and visual pattern is observed at all Surface roughness depths. Based on the above conclusion, further landmine detection analysis has been initiated, specifically focusing on the rough surface conditions.

	Smooth surface	Rough surface
VV Raw		
HH Raw		
VV Conv		
HH Conv		
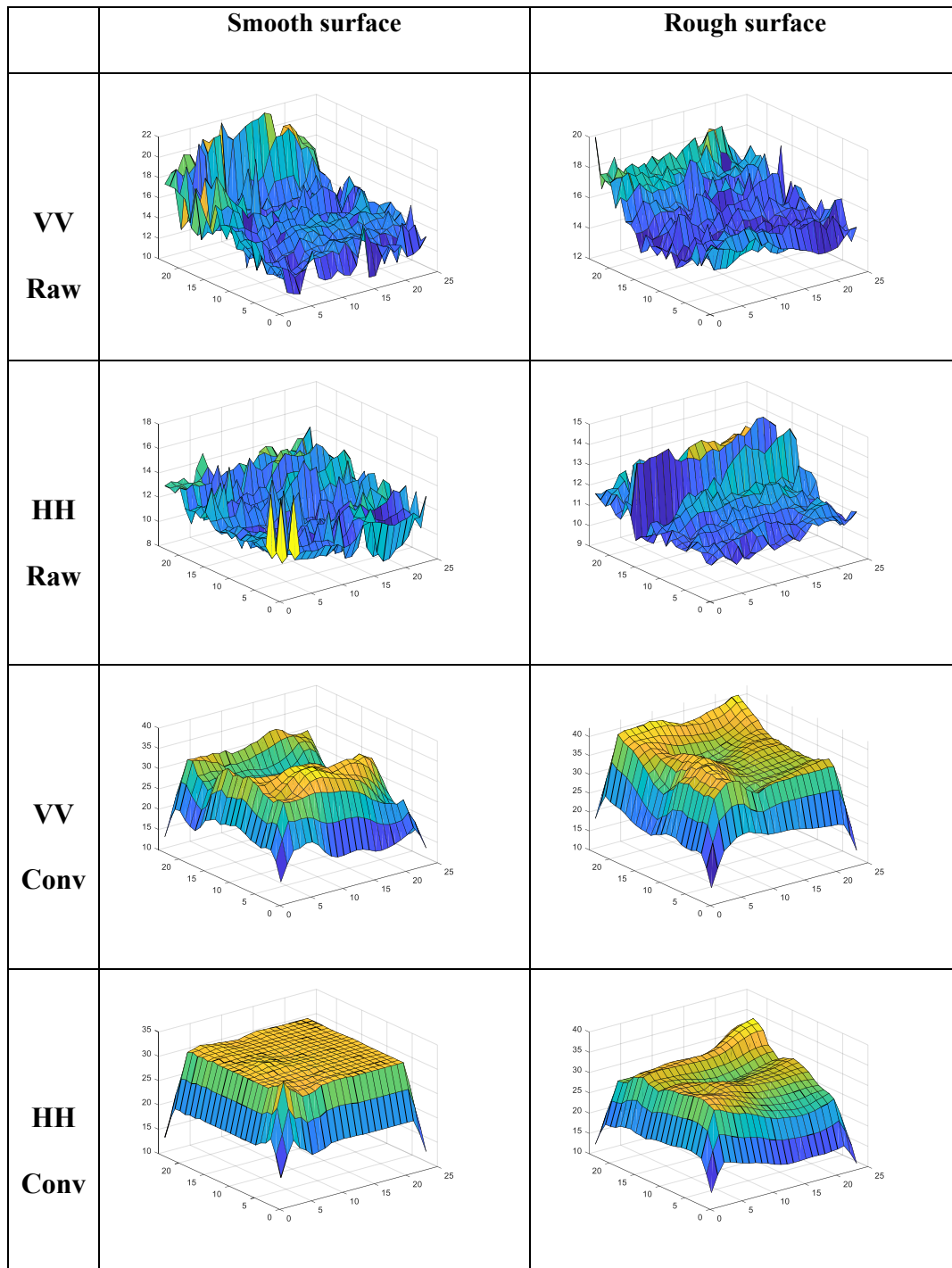
Fig 2.8 Surf diagram of Smooth and Rough Surface data for ATK with 1.0 cm Roughness Depth
(Image Dimensions: 24x24, Z-Axis Represents Backscatter Intensity

2.5.2 Analyzing polarization impact on X-Band data at varied surface roughness depth

In this subsection, an examination is conducted on the analysis of SCAT data transmitted and received with VV and HH polarizations. The emphasis is placed on

69

statistically comparing the raw data captured through these two polarizations, as outlined in Table 2.5.

This comparison aims to uncover the intricate impacts of polarization on X-Band data, particularly regarding variations in Surface Roughness Depth (SRD). Through this analysis, one aims to gain a deeper understanding of how these polarizations affect the data and their significance in detecting buried landmine.

The following observations have been made in Table 2.5:

- Significant variation is visual in the backscatter value between VV and HH polarised SCAT data.

- The VV polarization generally has a higher backscatter value and standard deviation than HH polarization.

- The standard deviation value also indicates that both the polarization has   some variation in their value irrespective of surface roughness depth.

The Kurtosis and Skewness parameter also shows variations, but some significant changes are visual at a surface roughness depth of 2cm. There are multiple changes in the direction of skewness present mostly in HH polarization.

This section concludes that raw VV and HH polarization data have some significant variation in backscatter value, which needs to be explored. The research indicates discernible differences in the amount of information contained within the VV and HH data sets. Given this divergence, it is imperative to investigate and implement a combined approach, such as fusion, to effectively augment the overall information content obtained from these data sources. This strategy can not only harmonize the disparate information but also contribute to a more comprehensive and integrated analysis.

Table 2.5 Comparative statistics of VV polarisation with HH polarisation for X-band data at different Surface Roughness Depth (SRD)

SRD (cm)	Band	Minm	Maxm	Mean	Medi--an	Std Devi.	Kurt--osis	Skew--ness
1	HH	9.900	14.300	11.510	11.375	0.143	11.785	-0.24
	VV	13.500	19.88	15.405	15.132	0.148	3.373	0.225
2	HH	1.300	15.700	11.733	11.300	0.267	4.020	-1.667
	VV	16.00	21.600	19.005	19.08	0.108	9.957	1.528
3	HH	10.400	13.600	11.783	11.750	0.0875	1.7034	-0.357
	VV	13.80	22.200	16.558	16.525	0.164	2.483	-0.265
4	HH	10.532	13.386	11.780	11.700	0.0855	1.832	-0.235
	VV	14.20	19.900	16.682	16.625	0.163	2.307	0.063
5	HH	11.050	13.600	12.251	12.240	0.055	4.983	0.621
	VV	14.450	17.300	15.800	15.810	0.058	3.980	0.235

2.5.3 Multipolarization fusion of X-band SCAT data

Based on the polarization analysis outcome, the VV and HH polarization data are combined through numerical fusion methods, as mentioned in Section 1.6. In this Section, three numerical polarization fusions of SCAT data have been analyzed for surface roughness minimization, and a novel polarization fusion method is proposed. All the results have been calculated under Full-frame data preprocessing and Local-frame data preprocessing to simplify evaluation work as discussed in the proposed theoretical model.

2.5.3.1 Analysis of Polarization Fusion with Full-frame image Preprocessing

The effect of polarization fusion has been investigated independently at all surface roughness depths to better understand their features and improve subsurface landmine detection. These are mentioned in succeeding paragraphs –

2.5.3.1.1 Data preprocessing

The Full-frame (24 x 24) image of raw σ_{VV}^{o} and σ_{HH}^{o} has been subjected to the preprocessing stage to reduce clutter and noise, as outlined in theoretical framework (Section 2.3). As shown in Fig. 2.7, several preprocessing steps are used for preprocessing the VV and HH polarized data. To provide a visual representation of these preprocessing stages, we have included graphs for each step in Fig. 2.9. The charts for raw, calibrated, and convoluted data for HH polarization are displayed in Fig. 2.9 (a), (b), and (c). In contrast, the plots for VV polarization are shown in Fig. 2.9 (d), (e), and (f). The raw data in both polarizations is noticeably more congested, and no pattern is visible. In contrast, the deconvoluted image exhibits a noticeable pattern in both polarizations. The deconvoluted data from various surface roughness depths show similar patterns. It indicates that data preprocessing improves the landmine features extraction by minimizing noise/clutter and antenna overlap.

Table 2.5 summarizes the statistics of data for live ATK data obtained in *VV* and *HH* polarization under rough surfaces at a depth of 1.0 cm. It is worth noting that the standard deviation and mean of the data in VV and HH are not the same. Compared to HH polarization, VV polarization has higher backscatter values and a higher standard deviation. However, the deconvoluted data in each polarization reveals a decrease in backscatter values but an increase in standard deviation, indicating a better discriminating capability. The findings show that the VV and HH polarizations contain significantly

different amounts of information. Data preprocessing puts them into the same range and combines them into clusters that can be segmented. The results show the same trend at different surface roughness depths.

HH   **VV**

Raw image

(a)   (d)

Calibrat-ed image

(b)   (e)

Convol-uated image

(c)   (f)
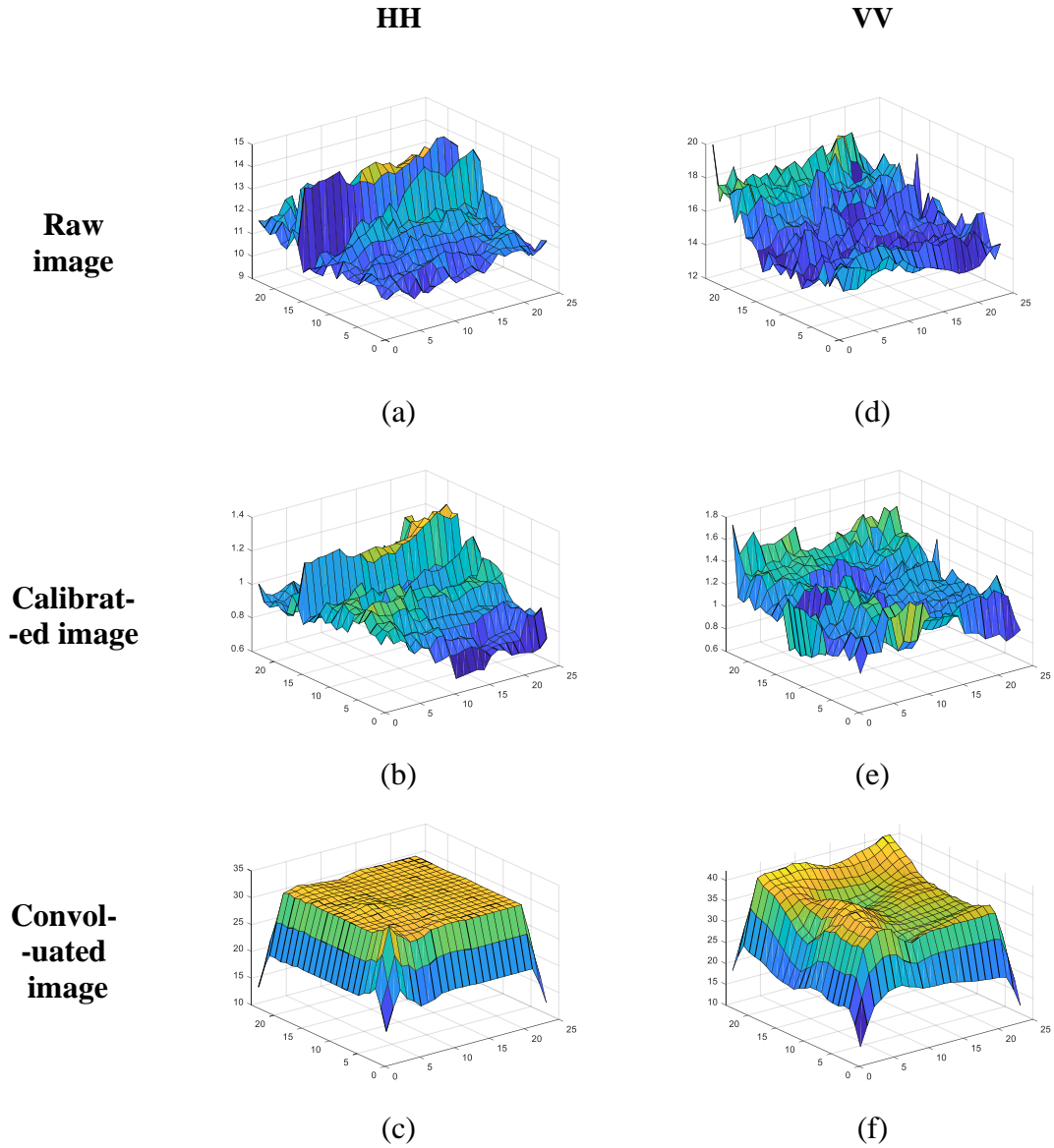
Fig. 2.9 Preprocessing for ATK with 1.0 cm Roughness Depth (Image Dimensions: 24x24, Z-Axis Represents Backscatter Intensity)

2.5.3.1.2 Evaluation of Fusion Approaches

The research findings highlight significant differences in the data obtained from two distinct polarizations, VV and HH, indicating that VV polarization contains more

distinguishing traits. The information content of the data would rise if the data from the two polarizations were integrated using appropriate fusion techniques, which would aid in the segmentation of landmine features. Combining data from two polarizations using a fusion approach would boost the information content of the data, which could be valuable for landmine feature segmentation. As a result, a fusion approach must be developed that simultaneously adds the information content of data in both polarizations and eliminates or decreases noise/clutter from any source.

Statistical Analysis

After preprocessing, the convoluted data has been processed to three polarisation fusion approaches as mentioned in Section 2.3.3 and the fundamental statistics parameters for the polarization fusion approaches have been obtained, as shown in Table 2.6. When the statistics parameters for the polarisation fusion data are compared to those for the deconvoluted data in Table 2.6, while the data's standard deviation (or spread) has increased, the mean backscatter value for the fused data has been severely shortened.

Table 2.6 Composite Statistics table for Antitank Mine at surface roughness depth of 1cm

Statistics	Data Raw HH	Conv HH	Raw VV	decon VV	Polarization Subtraction (VV-HH)	Polarization ration VV/HH	PDR	Proposed Fusion Approach
Mean	11.51	6.53	15.41	7.93	4.95	0.05	2.53	15.37
Min	9.90	0.87	13.50	2.11	-1.32	-9.39	0.01	2.71
Max	14.30	18.23	19.88	16.06	7.59	13.53	17.29	36.63
Std Dev	0.86	3.32	1.08	3.24	1.51	3.96	3.29	7.39

Because the backscatter primarily comes from the sand surface, and the landmine is only likely to generate slight variations in backscatter, the preceding fusion approaches,

which result in dispersion further from the mean, may result in the loss of landmine characteristics.

Histogram Analysis

The resulting histograms for VV and HH polarisations and their combinations have been employed in additional analysis with the objective of differentiating landmine features from clutter. The histograms of the deconvoluted data in each polarization have been compared to the histograms of the polarization fused data. The histograms of the preprocessed image (deconvoluted) in VV and HH polarization are displayed in Fig. 2.10 (a) & (b), while Fig. 2.10 (c), (d), and (e) show the histograms of the polarization fusion images (VV-HH, VV/HH, and PDR respectively).

(i) **Histogram of HH and VV polarisation**

Fig. 2.10 (a) and (b) show that the backscatter intensities in HH and VV polarization are more widely dispersed. Backscatter intensities in VV polarisation are more widely distributed than in HH. The VV polarisation has higher discriminating features than HH, in the same line as concluded in Section 2.5.2. Variations in the backscatter induced by the buried landmines are likely to be identified in data where backscatter intensities are widely separated at smaller intervals due to low dielectric contrast.

As a result, in any data fusion, it is important to preserve and, if feasible, improve the discriminating property of the data that emerges in one of the two polarizations.

(ii) **Histogram of VV-HH, VV/HH and PDR**

Compared to the histogram of VV and HH data, the histogram of VV- HH (Fig. 2.10 (c)) demonstrates that it has fewer discriminating features since smaller backscatter values with only a few pixels appear to have been lost.

The histogram for the ratio fusion VV/HH is shown in Fig. 2.10 (d); it can be observed that, while it is widely spread out and appears to have a significant discriminating capability, it only preserves backscatter intensities associated with a few pixels.
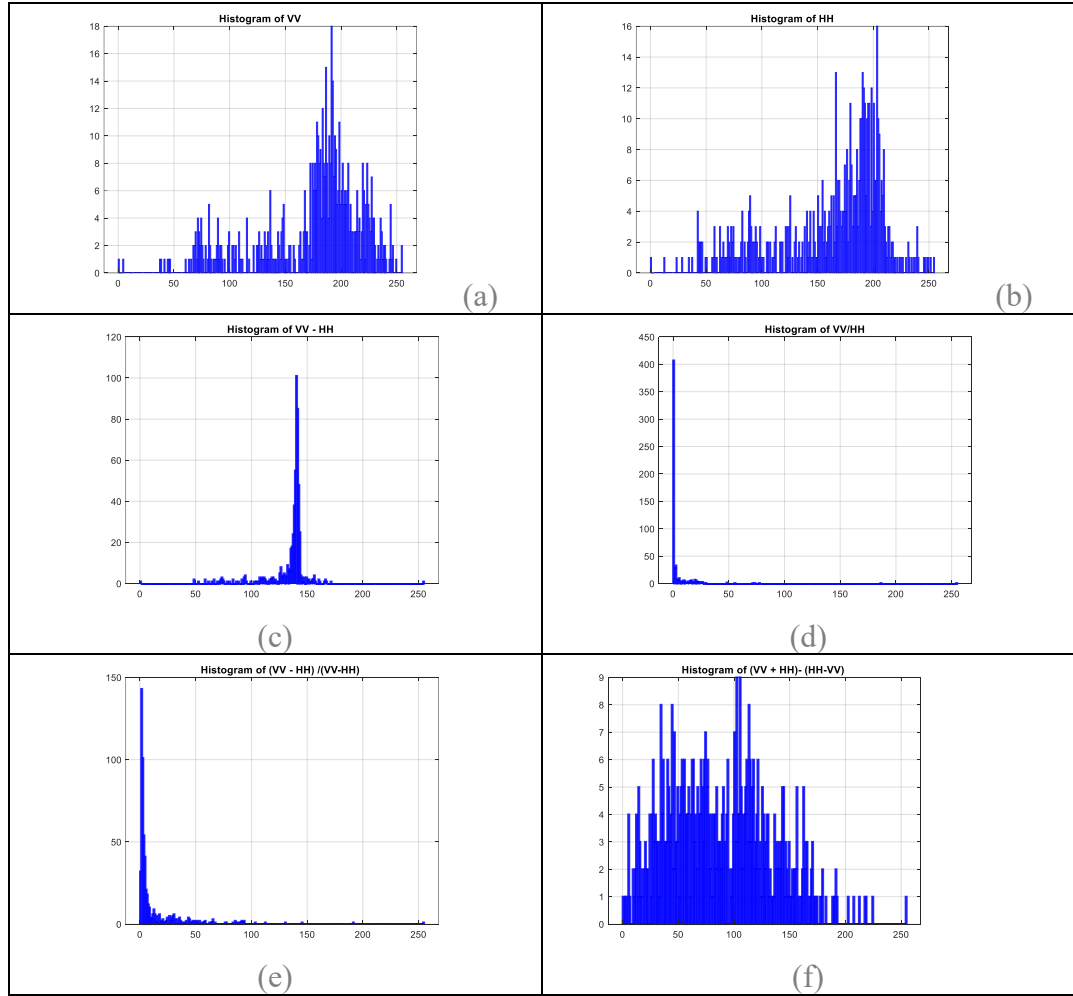
Fig. 2.10 Histogram (x-axis shows the scaled backscatter intensities in the range of 0-255 and the y axis represents (a) the count of pixels for given backscatter value for VV, (b) HH, (c) VV-HH, (d) VV / HH, (e) PDR and (f) Proposed fusion

Similarly, although the histogram of ((VV-HH)/(HH+VV), i.e., PDR looks to have the most discriminative features, it is concentrated in the left corner, indicating that it only contains pixels with low backscatter intensities.

76

As a result, none of these three polarisation fusion approaches maintain all the discriminatory characteristics present in the original data. They do not eliminate surface roughness effects to the greatest extent possible.

Based on the above findings, a proposed fusion of polarisation data, i.e., $[(VV + HH) - (VV - HH)]$, is likely to preserve the key distinguishing characteristics of the original data while reducing some of the surface roughness effects. Data segmentation using these proposed fusion approaches has also led to better outcomes, as shown in Fig. 2.9, compared to HH and VV polarisation. Therefore, it has been examined and compared to other techniques. This proposed fusion has the highest standard deviation, indicating that the data is widely dispersed and that most distinguishing traits from the original data have been preserved (Table 2.7). Fig. 2.8(f) shows the histogram of this proposed fusion, which offers higher information content and distinguishing features with backscatter values spread at substantially smaller intervals. It is backed up by the fact that the standard deviation is more heightened.

Segmentation Analysis

The segmentation of this data using thresholding is also significantly better than that accomplished using data from either of the polarizations separately (Fig. 2.11). The improvement is probably due to the preservation of identifying characteristics and the reducing undesired surface roughness effects. Even though the above statistics demonstrate a significant improvement in detection, it still suggests the presence of an object in the segmented zone, as the number of pixels segmented is significantly more than that of a buried landmine. The most likely number of pixels segmented is substantially more than that of a buried landmine.

This is most likely due to slight variations in backscatter intensities in the vicinity of a buried landmine. As a result, data preprocessing based on local images was employed for further analysis, and the proposed fusion has been applied.

a   b   c
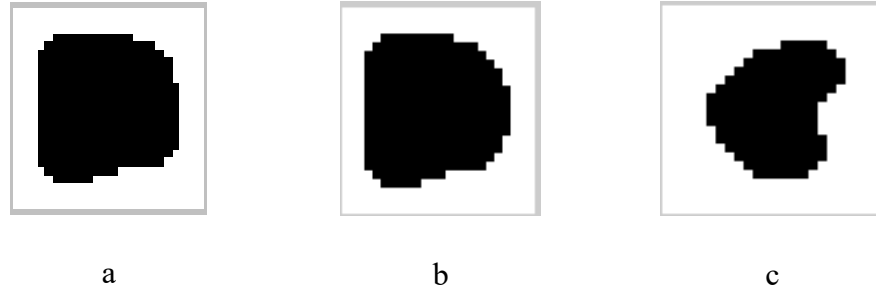
Fig. 2.11 ATK landmine Feature Extraction using segmentation (a) HH (b) VV and (c) proposed fusion approach (horizontal and vertical axes are the dimensions of the image 24x24)

2.5.3.2 Proposed polarization fusion with local-frame preprocessing

Local-frame processing has been utilized in this section, as discussed in Section 2.3 to reduce the effect of clutter and noise received from background. This data preprocessing method aims to confine all image processing processes to a smaller frame so that modest variations in backscatter intensity emitted by subsurface landmines are not submerged in the stronger backscatter of the surroundings during data modification. Experiments have been carried to determine the appropriate frame size. As a result, only the data extracted in an 8x8 frame is preprocessed. Histograms for all polarization fusions, including the suggested ones, are shown in Fig.2.10. It's worth noting that the proposed polarization fusion contains the most discriminating features and backscatter values in the range of unprocessed data. The Fig. 2.12 shows the histogram analysis for local-frame processing. It also appears from histogram (Fig. 2.12 (e)), that proposed fusion approach has maximum discrimination capability. Fig. 2.13 demonstrates the segmentation accomplished using the Local-frame based preprocessing approach for polarization fusion. The segmentation achieved employing maximum entropy-based thresholding for

the proposed polarization fusion (Fig.2.13) appears to segment the landmine characteristics accurately. These results can be compared to those obtained utilizing the entire image data preprocessing method previously outlined. It's worth noting that the
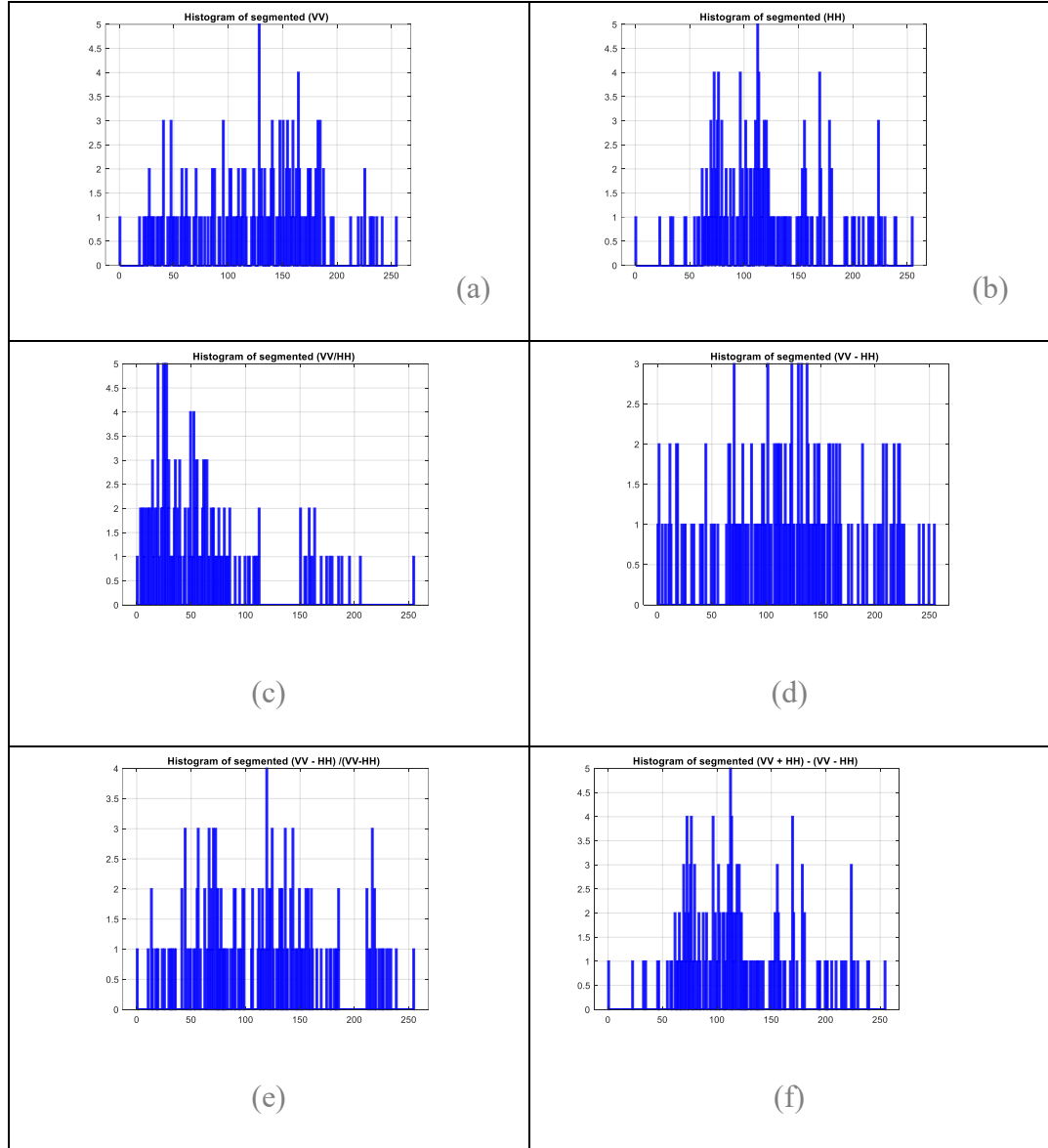
Fig.2.12 Histogram of Local-frame processing of HH, VV, polarization fusions and proposed fusion data (X-axis shows the scaled backscatter intensities in the range of 0-255 and *Y*-axis displays the number of pixels for a given backscatter value)
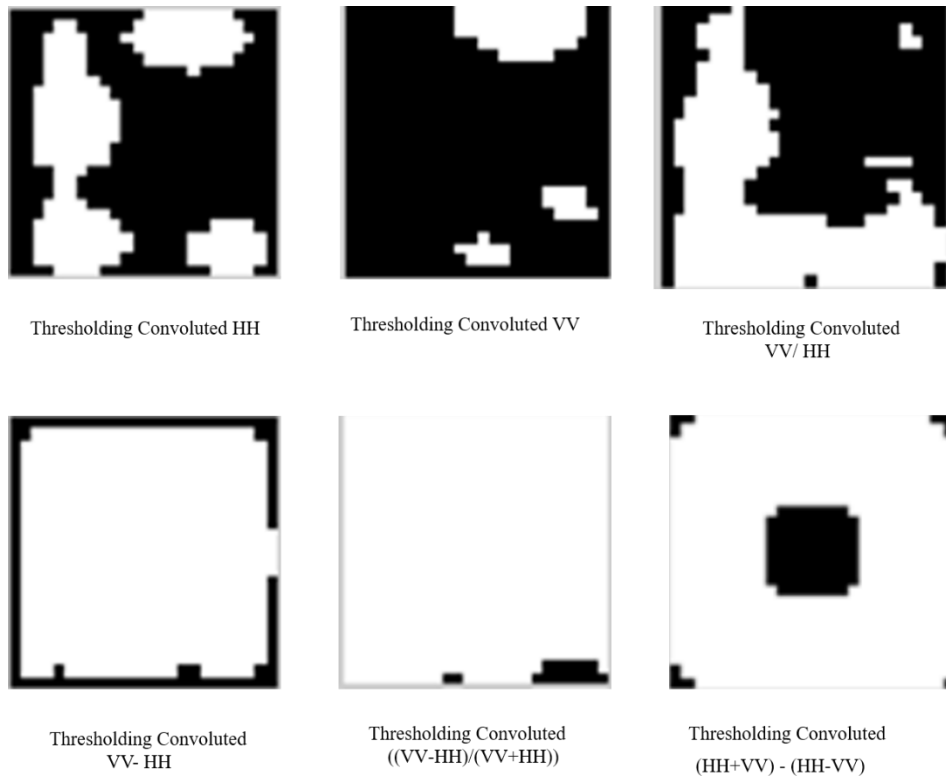
Fig.2.13 Segmentation of HH, VV, polarisation fusions and Proposed fusion

proposed polarization fusion method keeps both the more discriminating features and the backscatter in the original data's range. For the proposed fusion strategy, the segmentation performed using thresholding appears to segment the mine characteristics the most precisely, as shown in Fig. 2.13.

2.5.4 Investigation of entropy-based surface roughness minimization

Entropy has been employed as a metric to assess the effectiveness of various multipolarization fusion approaches to minimize surface roughness. In Table 2.7, shows the entropy values corresponding to different polarizations and their respective multipolarization fusions across various surface roughness depths. Each distinctive colored bar within the graph corresponds to data derived from individual polarizations and multipolarization fusion approaches. This visual depiction elucidates the relationship between entropy values and the diverse polarization strategies employed in surface

roughness minimization. The entropy for VV and HH polarizations has consistently demonstrated disparity at all roughness depths. Specifically, in both HH and VV polarizations, the entropy derived from Fuse data consistently records values lower than the overall entropy within the dataset. This research underscores that each fusion method implemented successfully attains a certain degree of surface roughness minimization.

Moreover, it is noteworthy that the entropy associated with VV polarization consistently registers smaller values than its HH counterpart. In the context of VV polarization, it is observed that only the fusion technique ((HH+VV) - (VV-HH)) achieves a lower entropy compared to VV alone. This finding emphasizes the effectiveness of this particular fusion method in minimizing entropy and enhancing the characterization of surface roughness.

Table 2.7 Entropy value for polarisation fusion approaches

SRD →					
Pol. Fusion ↓	1 cm	2cm	3cm	4cm	5cm
HH	2856	2906	2950	2906	3006
VV	1950	1676	2150	2706	2806
VV-HH	2816	2646	2706	3178	2912
VV/HH	2912	2506	2678	2832	2563
$\dfrac{VV - HH}{VV + HH}$	2618	2506	3856	2106	2006
(HH+VV) – (VV-HH)	1312	1550	1332	1558	1588

2.5.5 Multiband (X- and C- band) SCAT data analysis

X-band and C-band microwave data have been generated from the SCAT system, as mentioned in Section 2.2. X-band wavelength varies from 2.4 to 3.75 cm, but in this experiment, it is 3 cm, whereas the C-band wavelength varies from 3.75 to 7.5 cm, but in this experiment, a 6 cm wavelength has been used. As mentioned in Section 2.3, the surface roughness and smoothness are also a function of microwave wavelength, which subsequently affects the landmine detection performance. This experiment is pivotal for refining the methodology and enhancing the accuracy of landmine detection techniques in diverse environmental conditions. Fig.2.14 shows the surf plot of raw and preprocessed C-band SCAT data.

This subsection explores the discrimination capability of the C- and X- bands to establish the multiband microwave approach for landmine detection. An experiment has been carried out, during which the SCAT recorded data in X- and C-microwave bands at surface roughness depths of 1, 2, 3, 4, and 5 cm for VV and HH polarizations. Further a comparative analysis of statistical parameters has been done at Table 2.7.

Table 2.8 presents a comprehensive statistical evaluation of raw VV-polarised C- and X-band microwave data, offering valuable insights into their backscatter characteristics. Notably, the backscatter values associated with C-band data consistently appear lower than those across various surface roughness depths of X-band data.

The C-band has a higher Standard deviation value than the X-band, except at a surface roughness depth of 3cm. A higher value of standard deviation indicates higher discrimination features.

C-Band HH	C-Band VV

Raw
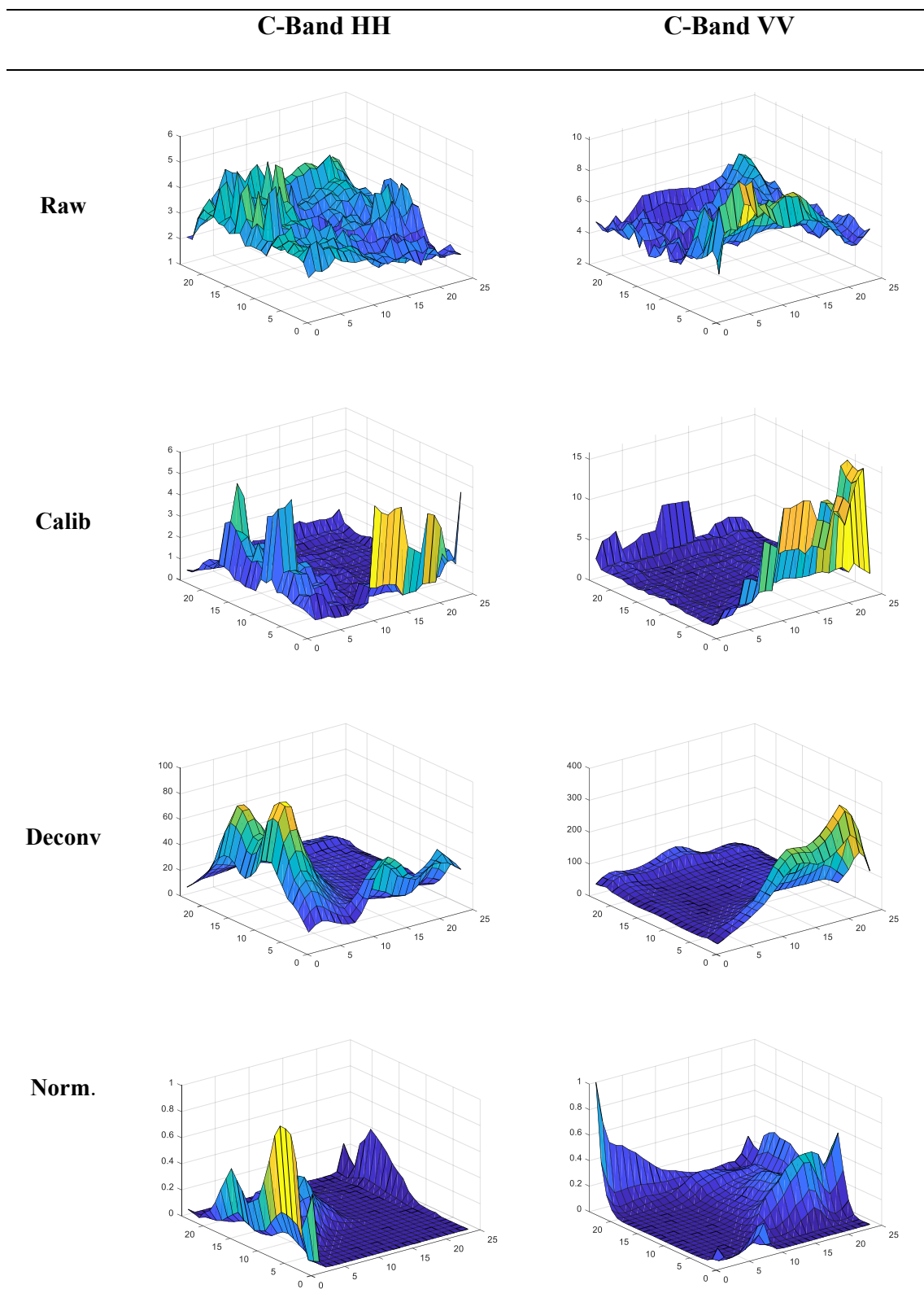
Calib

Deconv

Norm.

Fig. 2.14 Surf plot of raw and preprocessed C-band data (raw, calibrated, deconvoluted, normalised)

Table 2.8 Comparison of statistics of VV polarisation C- and X-band data at different Surface Roughness Depth (SRD)

SRD (cm)	Band	Min	Max	Mean	Medi- -an	Std Devi.	Kurt- -osis	Skew- -ness
1	C	3.340	10.180	5.323	4.9200	0.432	3.524	3.524
	X	13.500	19.88	15.405	15.132	0.148	3.373	0.225
2	C	4.500	8.700	6.667	6.625	0.112	10.602	10.610
	X	16.00	21.600	19.005	19.08	0.108	9.957	1.528
3	C	3.500	8.300	5.923	6.200	0.118	2.482	2.482
	X	13.80	22.200	16.558	16.525	0.164	2.483	-0.265
4	C	4	7.600	5.414	5.250	0.109	12.278	-1.559
	X	14.20	19.900	16.682	16.625	0.093	2.307	0.063
5	C	3.780	7.920	5.401	5.222	0.109	4.175	0.316
	X	14.450	17.300	15.800	15.810	0.058	3.980	0.235

The statistical parameters of kurtosis and skewness play a pivotal role in assessing the distribution and shape of the data. In this context, the statistical analysis reveals that C-band data exhibits higher values for kurtosis parameters. At the same time, X-band data has a higher value of skewness. These parameters are outliner sensitive and indicate the distribution's shape and the asymmetry of the data. Higher values suggest a more peaked and asymmetric distribution, signifying a richer and more distinct information content in SCAT data.

Fig. 2.18 shows the plot of backscatter intensity of X- and C- band microwave data at each pixel index (24x24), a pattern is visible in the plot, which significantly contributes in improvement in landmine detection.

VV	HH

Comparison of Pixel Values between X and C Band, VV pol at SRD = 1 cm

Comparison of Pixel Values between X and C Band, HH pol at SRD = 1 cm

Comparison of Pixel Values between X and C Band, VV pol at SRD = 2cm

Comparison of Pixel Values between X and C Band, HH pol at SRD = 2cm

Comparison of Pixel Values between X and C Band, VV pol at SRD = 3cm

Comparison of Pixel Values between X and C Band, HH pol at SRD = 3cm

Comparison of Pixel Values between X and C Band, VV pol at SRD = 4cm

Comparison of Pixel Values between X and C Band, HH pol at SRD = 4cm

Fig. 2.15 Scatter plot of backscatter value of X- and C- band SCAT data at SRD = 1,2,3,4, and 5 cm (X-axis of plot is Pixel value whereas Y-axis indicates Pixel value (backscatter intensity))

The Following observations have been drawn from Fig. 2.15:

- The value of backscatter intensity is higher for X-band SCAT data than for C-band in both the VV and HH polarisation. The wavelength of the X-band is smaller than the C-band, so despite lower penetration depth, they exhibit higher backscatter due to less absorption at these surface roughness depths.

- The gap of backscatter value between the X- and C- bands increases as the surface roughness depth increases, except at the VV polarisation wave at a surface roughness depth of 3 cm. It indicates that the microwave absorption increases as surface roughness depth increases.

- For VV polarisation at surface roughness depth, the difference in backscatter value does not follow the same pattern as the 3cm wavelength taken for X-band SCAT data. It further enhances the discrimination capability.

Moreover, a key observation arises when considering the trade-off between spatial resolution and backscatter value. Despite the C-band data demonstrating lower backscatter values, the decision-making process is affected by the spatial resolution

factor. The information content alone may not be the sole determinant; the spatial resolution of the data is also a critical consideration.

It emerges upon integrating statistics and data visualization that X-band SCAT data apparently provides superior trade-off between spatial resolution and backscatter value for landmine detection applications. The amalgamation of higher information content, as reflected in kurtosis and skewness values, coupled with an optimal spatial resolution, positions X-band SCAT data as the preferred choice in this context. However, C- band microwave band data appears to have higher discriminating features.

Unlike conventional single-band or single-polarization methods, the proposed multi-band, multi-polarization fusion significantly reduces surface roughness effects and improves detection sensitivity, especially for non-metallic mines.

2.6 Conclusion

This chapter explicitly addresses the primary motivation of enhancing the detection of buried subsurface objects, particularly landmines, in environments like India's western borders, where traditional technologies have shown limitations.

The study begins with an analysis of Surface roughness effects, which cause decreased backscatter from a subsurface landmine, have been studied in this chapter. Further, polarization fusion approaches and multiband SCAT data have been evaluated to reduce surface roughness and improve buried landmine detection. The proposed multipolarization fusion approach has been shown to maintain most of the distinguishing features of VV and HH polarizations while reducing undesired effects. The proposed fusion approach minimizes roughness-distortion while maintaining key polarization features, which is a crucial need for desert challenging terrain regions that are common in India's border regions. The fusion methodology gives the best consistent detection

results when SCAT backscatter is preprocessed using the local-frame oriented strategy and then applied to the proposed fusion approach. The results thus obtained when compared with the segmentation. The processed data is then subjected to thresholding for segmentation of landmine features. The results thus obtained when compared with the segmentation achieved using data in individual polarization indicate high segmentation accuracy. An analysis focused on minimizing surface roughness reveals improvements with all fusion approaches. Yet, to ensure proper segmentation accuracy, the fusion must yield an entropy value lower than the entropy observed in either polarization for surface roughness minimization to be considered acceptable. It is appears that the fusion of microwave data adds more information to buried landmine detection. Outcomes establish the effect of multiple polarization numerical fusion on buried landmine detection.

In the last part of this study, it is multiband SCAT data encompassing in both C- and X-bands have been evaluated. The primary aim was to investigate the potential for constructing a robust model for multiband fusion. A detailed statistical analysis of the multiband microwave scatterometer data showed that X-band data exhibits more pronounced and discernible features than C-band data. This analysis highlighted a significant tradeoff, revealing a careful balance between spatial resolution and backscatter value in multiband SCAT data. In essence, achieving a higher spatial resolution comes at the cost of sacrificing some backscatter information and vice versa.

The pivotal insight derived from our analysis leads to a significant conclusion: adopting a combined or fusion approach for multiband multipolarization microwave SCAT data significantly enhances the efficacy of landmine detection. This suggests that integrating information from different bands and polarizations provides a holistic view that surpasses the limitations of individual bands, thereby improving the accuracy and

reliability of landmine detection methodologies. This immediately supports the thesis's goal of developing domestic, remote sensing-based methods for detecting subsurface objects in challenging terrain.

Chapter-3

Improvement in Detection of Surface Objects using Fusion of Multiband and Multipolarization SAR Data

3.1 Introduction and problem definition

Measuring the parameters of both man-made and natural surface objects poses a formidable challenge, especially during adverse weather conditions like rain or fog. The SAR system is a fitting solution for these requirements, offering a reliable means to monitor Earth's surface properties consistently and swiftly in all-weather situations. PolSAR is recognized as the most powerful tool for acquiring high-resolution microwave images by integrating the concept of SAR with the vector nature of polarized EM waves. The backscatter value is sensitive towards the incoming SAR wavelength and polarization, making it easier to extract physical and geometrical characteristics of objects through the polarimetry characteristics of SAR data. As discussed in Section 1.5, the interest in PolSAR data has increased during the last few decades, especially after the launch of several spaceborne missions equipped with polarimetric capabilities. With the advancement of PolSAR research, remote sensing of both reachable and unreachable regions has become achievable [48].

Polarimetric target decomposition (PTD) is used in PolSAR data analysis to understand the scattering mechanisms of different objects or materials within data. PTD exploit the polarimetric information contents of SAR images. PTD is used to decompose the SAR return signals into individual scattering components, providing information about the targets' physical properties and spatial distribution. The foundation of surface object detection is the accurate interpretation of the fundamental scattering mechanism,

as different kinds of natural and man-made objects involve different types of scattering. The three primary types of scattering processes are the single (surface), double, and multiple bounces (volume) scattering. Oceans, rivers, lakes, and bare soil have a single bounce. When a horizontal flat surface is close to a vertical surface, like buildings and other vertical structures, a double bounce can be seen between the adjacent surfaces; in forest canopies and vegetated zones, randomly oriented scatters inhomogeneous media result in a multiple-bounce scattering effect [142]. Fig. 3.1 shows the schematic representation of the surface, double-bounce, and volume scattering components.

SINGLE BOUNCE SCATTERING (ROUGH SURFACE)

$$T_{11} = |HH + VV|^2$$

DOUBLE BOUNCE SCATTERING

$$T_{22} = |HH - VV|^2$$

VOLUME SCATTERING

$$T_{33} = 2|HV|^2$$
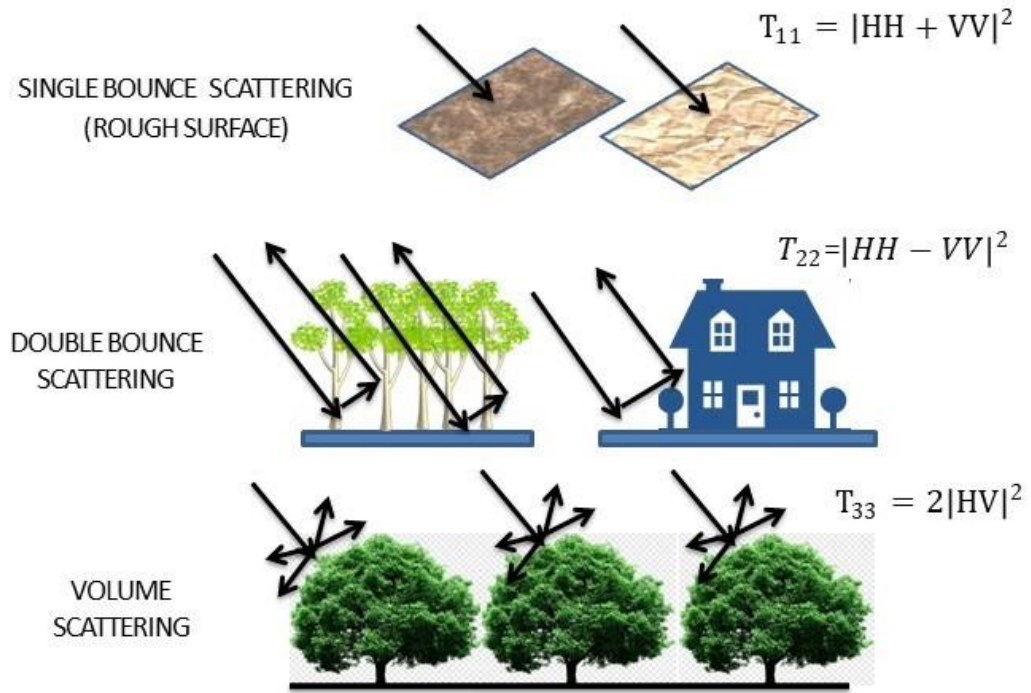
Fig. 3.1 Scattering components of PolSAR data [48]

PTD methods are further categorized based on available data, and work has to be done. Coherent target decomposition methods, including Freeman-Durden and Cloude-Pottier techniques, are tailored for coherent polarimetric SAR data, preserving amplitude and phase details to delineate surface, double-bounce, and volume scattering mechanisms.

Incoherent decomposition approaches are less prevalent but find utility when coherence information is compromised, often due to speckle noise [48][143]. The model-based approach involves decomposing the calculated matrix of covariance or coherency into a linear combination of models representing various physical scattering phenomena. Model-based decomposition techniques are popular because of their straightforward mathematical methodology and intuitive physical interpretation [144] [145]. Nevertheless, a significant drawback of the model-based decomposition techniques is the appearance of negative power [145]. This issue arises from overestimating a scattering component at a particular pixel. It can lead to negative contributions from the remaining scattering components, ensuring the overall power or span is constant. So many works have been done by researchers to reduce the overestimation of scattering components [146][147][148].

In the hybrid decomposition method proposed by Cloude *et al.* (2009) [149], the determination of volume scattering power is derived based on Freeman's scattering model. In addition, the single and double-bounce scattering powers are calculated using the information in the eigenvalue and eigenvectors. However, besides the cross-polarization, the power resulting from the interaction between surface and volume scattering mechanisms persists, necessitating its elimination for accurate interpretation of the scattering mechanisms. Maurya *et al.* (2018) [147] proposed a hybrid model aimed at enhancing the versatility of the hybrid Freeman decomposition model. This hybrid decomposition involves reducing cross-polarization power by employing deterministic matrix transformations. These transformations are applied by the predominant scatterer, aiming to eliminate a significant portion of the cross-polarization power generated by the

interaction between orthogonal states of polarization. The hybrid-based approach exhibits some results but still needs to find a way to remove cross-polarization coupling [147].

The radar backscattering characteristics are closely tied to the structure of the target and its orientation relative to the radar illumination. In urban environments, specifically, oriented man-made structures contribute significantly to generating cross-polarization power. This phenomenon introduces ambiguity in the interpretation of scattering mechanisms. Conventional model-based decomposition techniques, which attribute cross-polarization mainly to volume scattering, may inaccurately classify oriented urban structures as volume-scattering contributors. To address this challenge, a practical approach involves accurately modelling the cross-polarization power originating from urban areas [48].

The interactions between PolSAR wave and surface objects are complicated in nature, and specific SAR frequency and polarization combinations may produce different signals. The SAR wave can penetrate the upper canopy of vegetation at the C-band and primarily interacts with leaves and small branches. The backscatter of the C-band SAR is influenced by crown characteristics, including factors like leaf size, density, and orientation. Conversely, the L-band, with its deeper penetration into the canopy, may involve scattering from both the ground surface and tree trunks [152]. The occurrence of HV polarization at a specific frequency is closely associated with key forest parameters, such as biomass and height. In built-up areas, predominant scattering mechanisms often involve double-bounce interactions from vertical building walls and dihedral corner structures on the ground. On the other hand, ground-trunk backscattering, which has a strong echo like the ground-trunk backscattering in L-band, can occasionally be perceived as the double-bounce scattering mechanism. Fig.3.2 shows the schematic representation

of L- and C- band SAR wave with vegetation tree. On the other hand, the C-band double-bounce scattering component of man-made objects is weak. Because of this, it is challenging to distinguish between man-made and natural objects using single-frequency PolSAR. Therefore, to detect man-made targets, multiband PolSAR data needs to be explored [150][151].

(a)   (b)
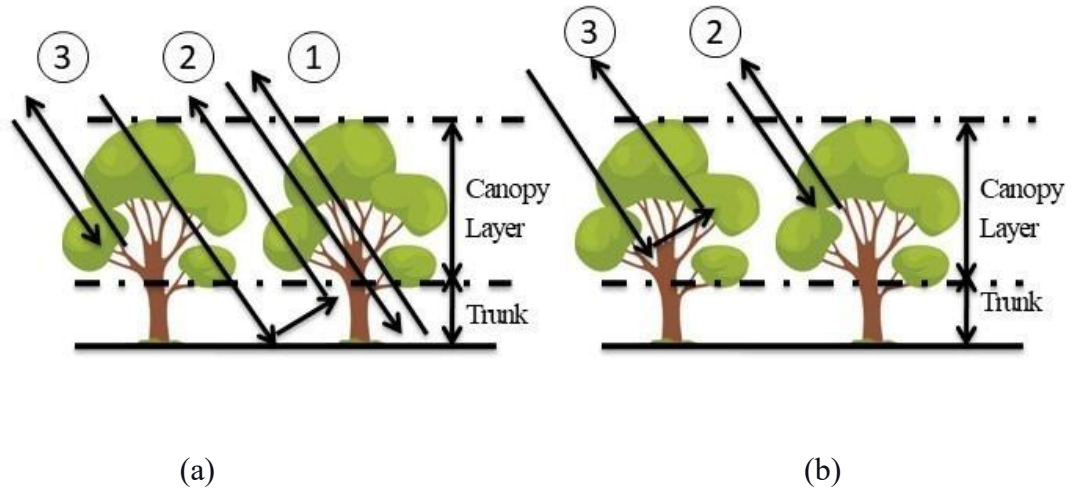
Fig 3.2 SAR interaction with vegetation [151], rays (1) surface-scattering, (2) double-bounce scattering, and (3) volume-scattering; a) L-band backscatter b) C-band backscatter

The single-frequency and single-polarisation PolSAR data limit the extraction of the composite physical and geometrical information [151]. With the availability of multi-frequency and multi-polarization SAR data, extensive research is underway to leverage the diverse characteristics of these datasets. Several researchers found that utilizing the multiband SAR data, enhance the detection and classification of surface objects. The study by Lang *et al.* (2014) [150] shows that differential performance in sea-ice detection is caused by the different frequencies of the L-band and the C-band. Longer wavelengths enable the L-band to excel in surface-volume scattering, whereas the C-band demonstrates superior capabilities in identifying ground types close to object surfaces. Combining SAR data at different frequencies resolves detection ambiguities. Huang *et al.* (2018)[151] used

regression model on Sentinel-1 and ALOS decomposed images to improve ground biomass. Cross-polarized radar waves are more vulnerable to volume scattering from object features or depolarization carried with multireflection at corners. An object exposed to a multiband, polarization-varying microwave radar system produces various images with varying informational content. With the diverse capability of C- and L-band PolSAR, there is a need to explore the fusion of both datasets to remove the overestimation of scattering power.

Image fusion and its applications are in high demand in remote sensing nowadays to achieve desired results by harnessing the capabilities of multiple images, which were impossible with a single image. Image fusion techniques and their evaluation are discussed in Section 1.6. PCA is one of the most extensively used image fusion techniques based on dimension reduction capability and has been utilized in processing PolSAR data. Prior research has indicated the utility of both L- and C-band polarimetric quantities, whether employed independently or in conjunction. However, earlier studies concentrated on a set of polarimetric parameters, typically fusing multiple specific parameters [154].

The selection of appropriate fusion parameter between two PolSAR image, is a matter of further research and needs further investigation L- and C- bands images are decomposed into surface, double-bounce and volume scattering through hybrid decomposition methods. Experiments have been done with L- and C- -band SAR images individually, and their ability to reduce cross-polarisation power has been assessed through the hybrid decomposition method. The dominant scattering component is selected based on the decomposed image of the PolSAR image; the man-made and natural objects are classified using the SVM classifier before and after the fusion of L- and C-band San Francisco city data.

Through an exploration of select polarimetric analysis results using the PTD theorem, this research aims to enhance the detection of both man-made and natural objects by fusing C- and L-band PolSAR data. This improvement is achieved by mitigating the issue of overestimation in scattering components.

This research aims to achieve the following specific objectives:

- To evaluate the effectiveness of L- and C-band data in mitigating the overestimation of scattering components using a hybrid decomposition technique.

- To explore the optimal fusion parameter for the C- and L-band PolSAR data based on their ability to reduce the cross-polarisation power.

- To assess the fusion of L- and C-band data to enhance the accuracy in detecting man-made and natural objects.

3.2 Study Site and Data set

The city of San Francisco (USA) has been taken as a study site for this research. Due to its prominence and dense population, numerous remote sensing applications have shown interest in San Francisco. The San Francisco area's C- and L- band data of Radarsat-2 and ALOS-1 PALSAR (VV. VH, HH, and HV) have been downloaded from the IETR portal [155]. Fig. 3.3 displays the raw image of the city of San Francisco, situated in North America. Established in the 1770s, the city experienced rapid growth, ultimately becoming the largest city on the west coast of the United States. Its original layout adhered to a grid pattern imposed on hilly terrain. 1906, a devastating earthquake led to the city's destruction, prompting a comprehensive reconstruction effort. Renowned for its meticulous urban planning, San Francisco boasts high population density and limited space for expansion. Notably, the city features the expansive Golden Gate Park in

its western region, covering an approximate area of 4.12 km^2. The L-band ALOS-1 PALSAR image (captured on 28th March 2009) and C-band RADARSAT-2 image (captured on 10th April 2010) of the San Francisco area are used for this study. The study area prominently includes urban buildings, forest, water, and vegetation.

<div align="center">(a)   (b)</div>
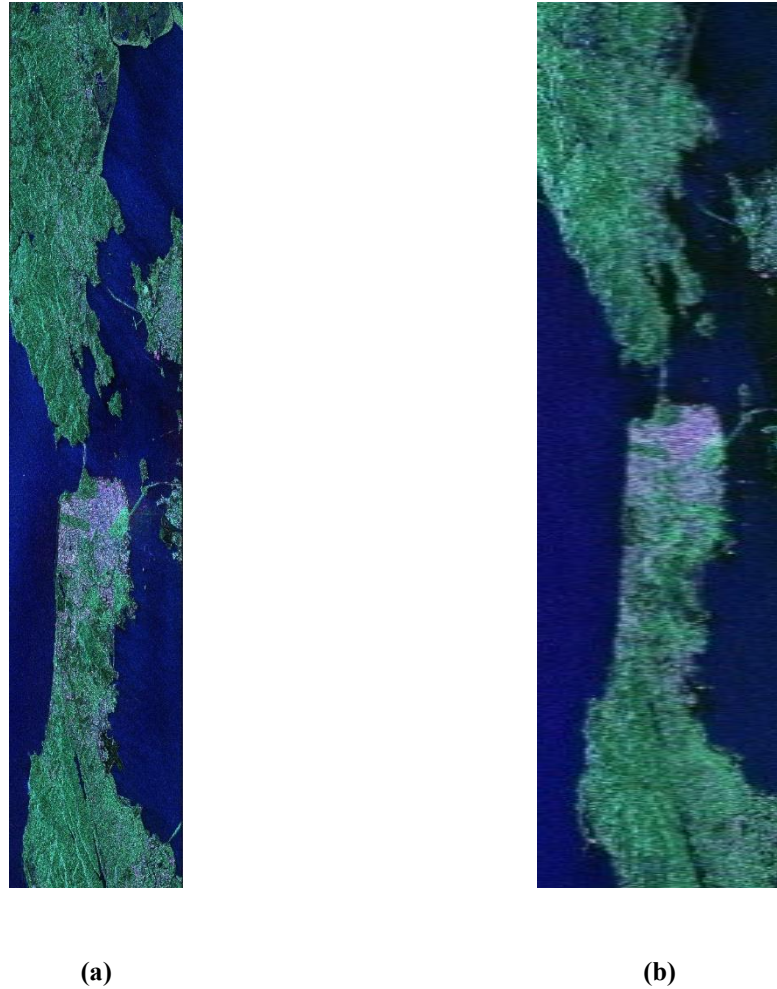
Fig. 3.3 Raw SAR data after multillooking (a) Radarat-2 and, (b) ALOS-PALSAR

3.2.1 Radarsat-2 (5.406 GHz) Data

This study takes the C-band Radarsat-2 image over the San Francisco bay region in the fine quad-beam mode. Table 3.1 shows the data specification of the Radarsat-2 sensor. The Pauli RGB of the San Francisco area is displayed in Fig. 3.2(a).

Table 3.1 Radarsat-2 data specification

Specification	Details
Datatype	Single Look Complex (SLC)
Mode	Fine Quad 9 (FQ9)
Polarisation	Quad Pol. (VV, VH, HV and HH)
Orbit	Ascending
Date of Acquisition	09th April, 2009
Revisit time	24 days
Data format	CEOS
Swath Width	500 km
Resolution	30 m

3.2.2 L-band SAR Data

Table 3.2 shows the technical specification of the L-band ALOS PALSAR-1 dataset.

Table 3.2 Technical specification of L-band ALOS PALSAR-1 dataset

Specifications	Details
Datatype	SLC
Level	1.1
Mode	PLR
Polarisation	HH, HV, VV and VH
Spatial Resolution (meter)	30 m
Swath width	30 km
Date of acquisition	11th Nov,2009

3.3 Theoretical modelling

3.3.1 Hybrid decomposition theorem

The scattering phenomenon at the target can be characterized by establishing a connection between the complex amplitude of the incident field ($\mathbf{E}_i$) and the backscattered field ($\mathbf{E}_s$), as expressed in eq. (3.1) [48]

$$\mathbf{E}_s = [S]\ \mathbf{E}_i \tag{3.1}$$

And,

$$[S] = \begin{bmatrix} S_{HH} & S_{HV} \\ S_{VH} & S_{VV} \end{bmatrix} \tag{3.2}$$

Here, S_{ij} denotes the scattering coefficients. Notably, the diagonal elements of the scattering matrix pertain to 'co-polar' terms, signifying the same polarization between the scattered and incident waves. In contrast, the off-diagonal elements relate to the orthogonal polarizations and are called 'cross-polar' terms [48].

In radar signal processing, the scattering matrix is commonly used to describe ideal scenarios with a single, pure target. In practical scenarios, distributed targets are more relevant, as illuminated by a fixed polarisation and frequency wave, backscattered returns lose coherence, resembling partially polarized waves. Analysing scattering from distributed targets is improved by describing the target through 2$^{\text{nd}}$ order moments of fluctuations, leading to polarimetric coherency and covariance matrices. A coherency matrix is a mathematical depiction of polarimetric characteristics used in radar. It is derived from the scattering matrix, which explains the interaction and dispersion of EM waves with a target in various directions. The fully polarimetric 3x3 coherency matrix [T] can be generated as [149]

$$[T] = \begin{bmatrix} T_{11} & T_{12} & T_{13} \\ T_{12}^* & T_{22} & T_{23} \\ T_{13}^* & T_{23}^* & T_{33} \end{bmatrix}$$

$$= \begin{bmatrix} \frac{1}{2}|S_{HH}+S_{HV}|^2 & \frac{1}{2}(S_{HH}+S_{VV})(S_{HH}-S_{VV})^* & (S_{HH}+S_{VV})S_{HV}^* \\ \frac{1}{1}(S_{HH}-S_{VV})(S_{HH}+S_{VV})^* & \frac{1}{2}|S_{HH}-S_{VV}|^2 & (S_{HH}-S_{VV})S_{HV}^* \\ S_{HV}(S_{HH}+S_{VV})^* & S_{HV}(S_{HH}-S_{VV})^* & 2|S_{HV}|^2 \end{bmatrix}$$

$$\tag{3.3}$$

The diagonal elements of the coherency matrix denote the correlation of components within the Pauli target vector. Consequently, these diagonal elements represent real values, representing the span or total power. On the other hand, the off-diagonal elements of the coherency matrix depict various correlations between distinct components of the Pauli target vector.

The total power or span for coherency matrices is computed as:

$$Span = |S_{HH}|^2 + 2|S_{HV}|^2 + |S_{VV}|^2$$

$$= T_{11} + T_{22} + T_{33} \tag{3.4}$$

The main reason for its matrix's extensive use in the literature is the ease of interpretation of the scattering phenomena via formulation of a target decomposition scheme through a coherency matrix. The PTD theorems establish a connection between PolSAR observations and the intrinsic properties of the scatterer being studied. The categorization of PTD theorems can be broadly divided into coherent and incoherent decomposition techniques. Coherent decomposition methods express the measured scattering matrix as a combination of canonical scattering mechanisms. Notable contributions in this category have been made by researchers. Pauli decomposition is the most frequently employed technique [149]. Coherent decomposition methods are mainly suitable for pure targets, relying on the decomposition of the measured scattering matrix. However, most targets in real scenarios are distributed, so incoherent decomposition methods prove more appropriate for effective decomposition [48]. Incoherent decomposition techniques leverage information inherent in the coherency matrix. These techniques can be categorized into two main groups: eigenvector-based and model-based decomposition [48]. Eigenvector decomposition methods involve quantitatively examining the eigenvalues and eigenvectors of the coherency matrix. Meanwhile, model-

based methods entail decomposing the coherency matrix into a sum of physical scattering models.

Freeman and Durden initially introduced the model-based decomposition of PolSAR data through their three-component scattering model, commonly referred to as Freeman-Durden's decomposition (FDD) method [144]. Every resolution element or pixel in a PolSAR system is measured for the scattering matrix. This matrix fully determines the scattering process for deterministic or point scatterers. However, in the context of distributed scatterers, the scattering matrix remains no longer deterministic yet random because of the complexity of the scattering process, which is caused by the coherent nature of SAR systems. Typically, this random quality in SAR data is called speckle noise. As outlined in the literature on speckle filters for PolSAR data, various filtering options have been introduced and confirmed through validation. These alternatives aim to minimize or eliminate speckle noise in PolSAR data.

In most model-based decomposition techniques, the hostile scattering powers for co-polarized scattering mechanisms (surface and double bounce) are mainly generated by overestimating the volume scattering contribution. In recent years, much literature has reduced the overestimation of scattering components by introducing new scattering models or proposing coherency matrix transformations. New scattering models reduce the overestimation of volume scattering contribution either by better characterization of vegetation or by modelling the cross-polarization power generated from sloped and oriented scatterers. In unitary transformations, the exaggeration of volume scattering is mitigated by rotating the coherency matrix through an angle determined through the minimization of cross-polarization power [156][157]. By using both methods, the number of overestimated pixels can be decreased.

The adequate literature category where the primary concern is removing pixels having overestimation power belongs to hybrid decomposition. In the hybrid decomposition category, eigenvector and eigenvalue information are utilized together with the physical scattering models to overcome the overestimation problem. This category was commenced by Cloude *et al.* (2009) [149]. After that, many excellent works have been reported where the overestimation problem of the model-based decomposition method is targeted [158][159].

In 2010, Cloude *et al.* (2009) [149] proposed a hybrid three-component decomposition method. In this method, surface and dihedral scattering models are characterized by eigenvalues and eigenvectors of the coherency matrix. In contrast, the volume scattering matrix is the same as that of the FDD method. Claude's three-component decomposition method can be described as

$$[T] = [T]_S + [T]_d + [T]_V \tag{3.5}$$

Here [T] represents the measured coherency matrix, while $[T]_S$, $[T]_d$, $[T]_V$ denote the matrices corresponding to surface, double-bounce, and volume scattering mechanisms.

$$[T]_S = m_s \begin{bmatrix} cos^2\alpha_S & cos\alpha_S \, sin\alpha_S \, e^{j\Phi_S} & 0 \\ cos\alpha_S \, sin\alpha_S \, e^{j\Phi_S} & cos^2\alpha_S & 0 \\ 0 & 0 & 0 \end{bmatrix} \tag{3.6}$$

$$[T]_d = m_d \begin{bmatrix} cos^2\alpha_d & cos\alpha_d \, sin\alpha_d \, e^{j\Phi_d} & 0 \\ cos\alpha_d \, sin\alpha_d \, e^{j\Phi_d} & cos^2\alpha_d & 0 \\ 0 & 0 & 0 \end{bmatrix} \tag{3.7}$$

$$[T]_V = m_v \begin{bmatrix} \frac{1}{2} & 0 & 0 \\ 0 & \frac{1}{4} & 0 \\ 0 & 0 & \frac{1}{4} \end{bmatrix} \tag{3.8}$$

The coefficients of scattering power for surface, double-bounce, and volume scattering processes are denoted m_s, m_d, and m_v in the corresponding equations.

The α_S and α_d are function of angle of incidence and surface's dielectric constants. Here Φ_S and Φ_d are the scattering phase for surface and double-bounce mechanisms, respectively [2]. The single and double-bounce scattering postulating orthogonality into equation 3.6 as

$$\alpha_S + \alpha_d = \frac{\pi}{2}, \text{ and } \Phi_d - \Phi_S = \pm \pi \tag{3.9}$$

Now equation (3.5) can be reducing as

$$[T] = [T]_{sd} + [T]_v \tag{3.10}$$

where $[T]_{sd}$ is the combined matrix for single- and double-bounce scattering mechanisms, given by

$$[T]_{sd} = \begin{bmatrix} m_s cos^2\alpha + m_d sin^2\alpha & cos\alpha\ sin\alpha\ e^{j\Phi}(m_d - m_s) & 0 \\ cos\alpha_s\ sin\alpha\ e^{-j\Phi}(m_d - m_s) & m_d cos^2\alpha + m_s sin^2\alpha & 0 \\ 0 & 0 & 0 \end{bmatrix}$$

$$\tag{3.11}$$

In hybrid Freeman decomposition method, m_v is calculated first from (3.6) as

$$m_v = 4\ T_{33} \tag{3.12}$$

The other two scattering power coefficients m_d and m_s, are given in (3.13) which can be computed as the eigenvalues of the remaining rank-2 coherency matrix left after subtracting the volume scattering contribution.

$$m_{d,s} = \frac{T_{11} + T_{22} - 3\ T_{33} \pm \sqrt{(T_{11} - T_{22} - T_{33})^2 + 4\ |T_{12}|^2}}{2} \tag{3.13}$$

The main objective behind this decomposition method is the removal of cross-polarisation power [147].

3.3.2 Scattering characteristic analysis of objects in L- and C-band PolSAR data

SAR penetrates the forest canopy and thus provides a signal from its physical structure, in contrast to multispectral sensors, which only offer information from the top of the tree cover. The surface objects' scattering mechanisms are significantly impacted by variations in the frequency and polarization of SAR signals. The interaction of SAR with natural objects such as agricultural vegetation and forests is a complex phenomenon, and a particular integration of frequency and polarisation may generate different information. Being a large wavelength, the L-band SAR can penetrate tree cover and gather backscattered from stem, trunk, and ground. L-band SAR interaction with man-made and natural objects exhibits surface, double-bounce and volume scattering. However, the value of scattering components depends upon several reasons, including objects' roughness and dielectric characteristics.

However, SAR with wavelengths shorter than the C-band cannot penetrate through vegetation, including tree branches and leaves. Thus, when a C-band radar is used to scan a forest-cover, the upper leaves of the trees backscatter the SAR signal. In the C-band, the vegetation area has high entropy processes. The scattering mechanism of the vegetation area is made up of volume scattering, odd-bounce scattering, and even double-bounce scattering from ground-trunk or man-made targets because the L-band SAR signal can reach the ground. The L-band forest area comprises a combination of low and high entropy processes. (Fig.3.2). The C-band also exhibits significant sensitivity to soil surfaces, which exhibit greater roughness in the C-band compared to longer wavelengths.

Consequently, this results in a reduced contrast in backscatter between forest and non-forest areas compared to L-band SAR [49].

Nevertheless, interpreting SAR signals over distributed target regions is more challenging than optical signals. This ambiguity frequently leads to the erroneous detection of deforestation and degradation events in false alarm scenarios. Several research studies have exhibited the integration of C- and L-band SAR backscatter through image fusion approaches to reduce the ambiguity in the detection/classification of surface objects [160][161].

3.3.3 Image fusion of L- and C- band PolSAR data

Combining or fusing two remote-sensing images is a complex task and requires implementing several image preprocessing techniques. The selection of appropriate image fusion techniques requires a careful analysis.

Image fusion is a process that merges two or more sensor images to extract additional information [10]. PCA, HSV, Brovey Transform and GS Transform fusion methods are among the most reported image techniques; a detailed literature review has been discussed in Section 1.6 for remote sensing image fusion. The PCA technique has been chosen for this research due to its ability to perform well in large-size distributed remote sensing datasets. Image fusion has been evaluated by the capability of improving the classification accuracy of man-made structures and natural objects. Several image processing techniques to classify the image have been reported in the literature. SVM is one of the most reported methods for PolSAR data analysis, so it is taken in this research.

3.3.3.1 PCA

The PCA image fusion aims to exploit the variations present in the input images to create a fused image that maximizes the representation of essential features while minimizing noise and redundant information [162]. The PCA procedure takes a set of correlated multispectral bands and transforms them into a set of uncorrelated bands using the statistical properties of the imagery. A correlation matrix is used to derive eigen values and eigen vectors that transform the original correlated data set into an uncorrelated data set. The successive principal components are orthogonal and uncorrelated. PCA reduces the dimensionality of the highly correlated dataset, such as multispectral data. The component with the highest variance is principal component-1(PC1). The PC1 contains the complete information. The first three principal components contained over 95% of the total variance of the fused image and were taken for the fusion [9]. The SAR intensity is matched to the PC1 of the multispectral dataset and then replaced with the SAR component. After an inverse PCA transformation, a high spatial-resolution MS image is formed [163][164]. Fig. 3.4 shows the image fusion process.
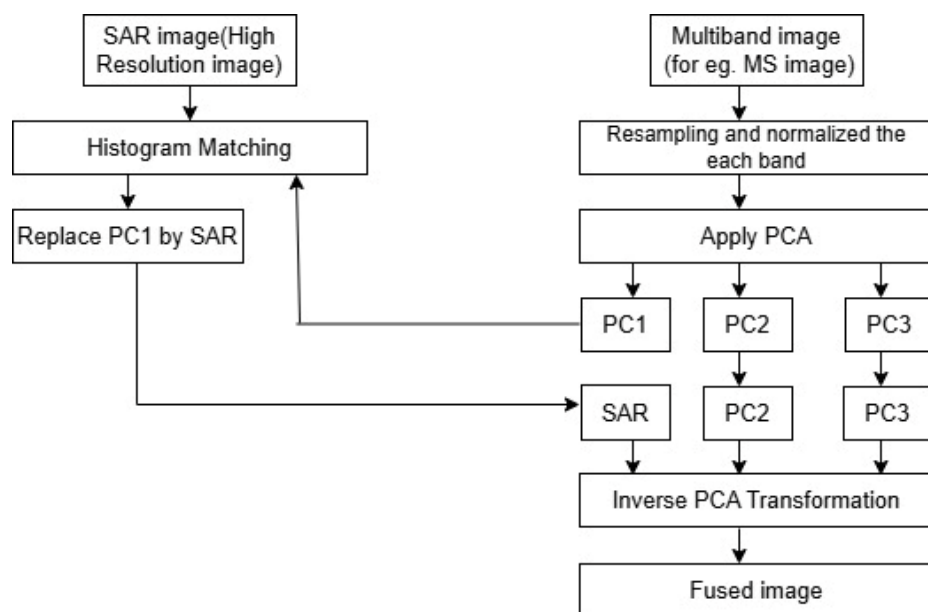
Fig. 3.4 Image fusion process

The process of classifying a given collection of data into groups according to the characteristics seen in the training set of data is called classification. SVMs, or support vector machines using a collection of labelled training data, the support vector machine (SVM) is a supervised learning technique that creates input-output mapping functions. The mapping function may take the form of a regression function or a classification function, which determines the category of the input data.

3.4 Implementation

As discussed in Section 3.2, the experimental data has been collected in the C- and L-band with VV, VH, HV, and HH polarizations. The implementation and analysis discussed in this section follow the theoretical modelling in Section 2.3. The implementation model consists of three stages. Fig. 3.4 depicts a flow diagram summarizing a set of image processing procedures defined for execution and Fig. 3.6 shows the flow diagram of hybrid decomposition.
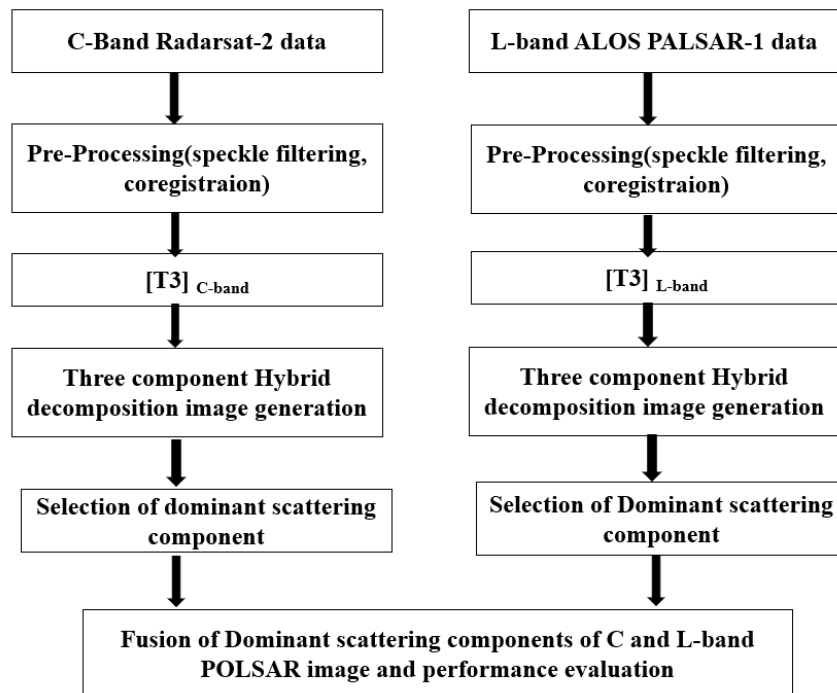
Fig. 3.5 Flowchart of research work

Extraction of scattering components from C- and L-band image using hybrid decomposition techniques is the first stage of the implementation. The T3 matrix has been generated for both datasets. The decomposition techniques are evaluated by computing mean scattering power of surface, double-bounce and volume scattering of three preselected patches of man-made and natural objects. Here, man-made structures, vegetation and water are selected to evaluate scattering power components. All the processing has been done on both PolSAR data separately.
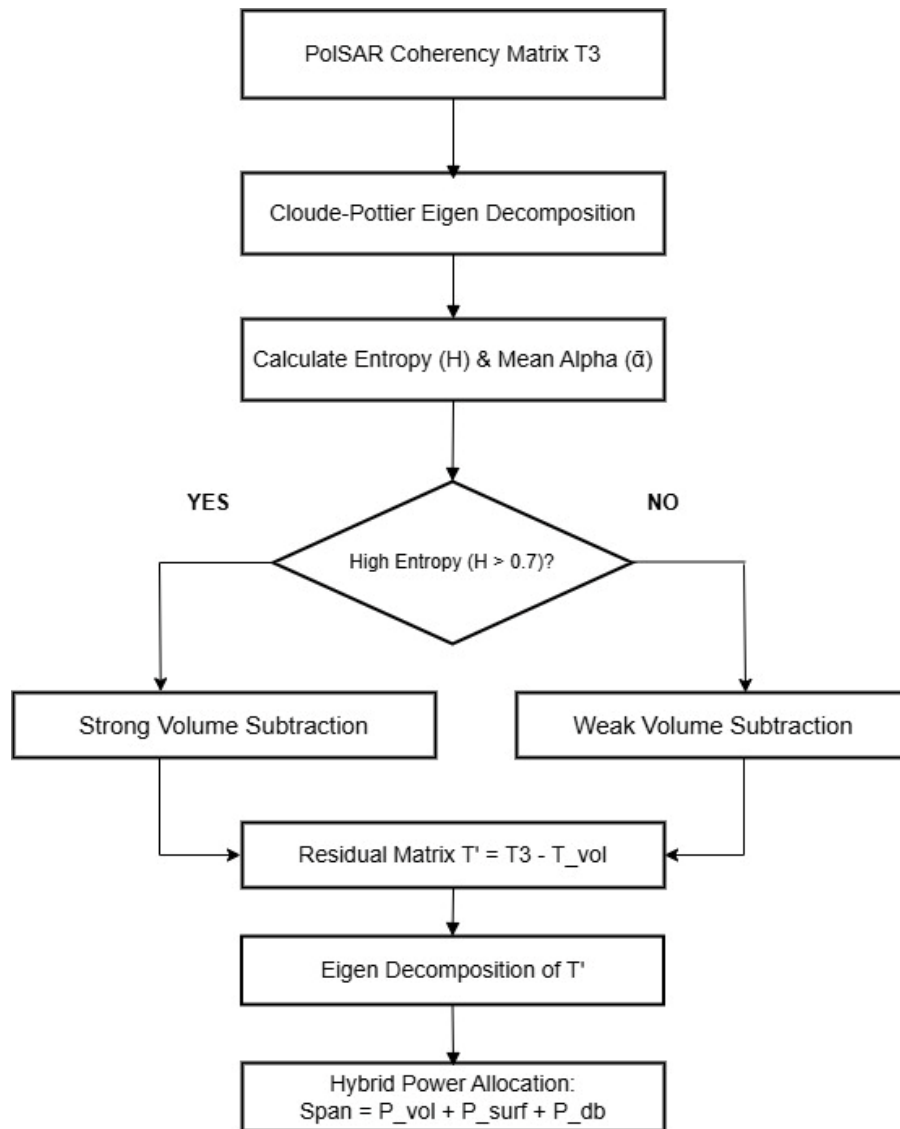
Fig. 3.6 Hybrid Decomposition flow diagram

The second implementation stage selects the appropriate scattering component parameters from C- and L-band data for fusion. The parameter selection has been done to address the overestimation of any scattering component to others.

The final implementation step is the image fusion of L- and C- -band PolSAR data. All the fusion processing has been done on decomposed images. Both data are preprocessed with the following preprocessing steps before fusion:

(i) Speckle filtering

(ii) Multilooking

(iii) Ellipsoid correction

(iv) Reprojection to common coordinate

(v) Coregistration of both datasets

(vi) Subset of common area

The Lee-Sigma speckle filter of 5x5 window size has been used as a speckle filter. Two rows and one column are used for the multilooking of the dataset. In this research, PCA fusion techniques are used. The classification accuracy of man-made structures and natural objects has been taken as a factor of image fusion evaluation. SVM has been used to compute classification accuracy.

3.5   Results and discussion

In this work, the experiments have been implemented on two different multi-parametric PolSAR data of the same geographical region (San Francisco, U.S.A.). The first dataset is collected from L-band ALOS-1 PALSAR, and the second is from the C-band RADARSAT-2 sensor. The improvement achieved by implementing the proposed fusion model is evaluated by overall classification efficiency by analyzing three different surface objects. The results of proposed fusion model have been discussed in this section.

3.5.1 Analysis of scattering components using hybrid decomposition method

Scattering component analysis is done separately on both datasets, and results are discussed in subsequent subsections.

3.5.1.1 L-band data

The L-band San Francisco image contains man-made objects (such as buildings and roads) and natural objects (such as Water, Forest, and vegetation). Fig. 3.5 (a) displays the multilook (row =2, column =1) Pauli RGB composition of raw L-band data. The coherency matrix T3 has been generated, and its matrix elements T11, T12, T21, T22, T23, and T33 have been shown in Figs. 3.5 (b)-(g), respectively. The diagonal elements of T3 are representation of surface, double-bounce, and volume scattering components. Where off-diagonal elements representation of cross-polarisation coupling. Fig. 3.5 (b) highlights the man-made structure (urban); it is simply an indication of the cross-polarization coupling of the T21 matrix element.

A study region is cropped from raw data of L-band PolSAR consisting of man-made and natural objects to reduce computation complexity and storage. The study region mainly includes buildings, forests, dry grasslands, farmlands and water bodies. The hybrid decomposition approach (as mentioned in Section 3.3.1) is compared with FDD method to show the improvement in the reduction of overestimation of the polarisation scattering component. Fig. 3.6 shows the three-component hybrid decomposition of PolSAR data. For visualization, the FCC decomposed image of the research area by the hybrid decomposition method is shown in Fig. 3.7. The decomposed image (Fig. 3.6 b) shows a bright glow across the Golden Gate Bridge. It simply indicates dominant double-bounce scattering in the double-bounce scattering component. It merely shows the cross-polarisation of the T23 matrix element. Fig. 3.6 (b) shows a bright glow in urban areas,

(a) RGB (b)T11 (c) T12 (d) T13 (e) T22 (f) T23 (g) T33
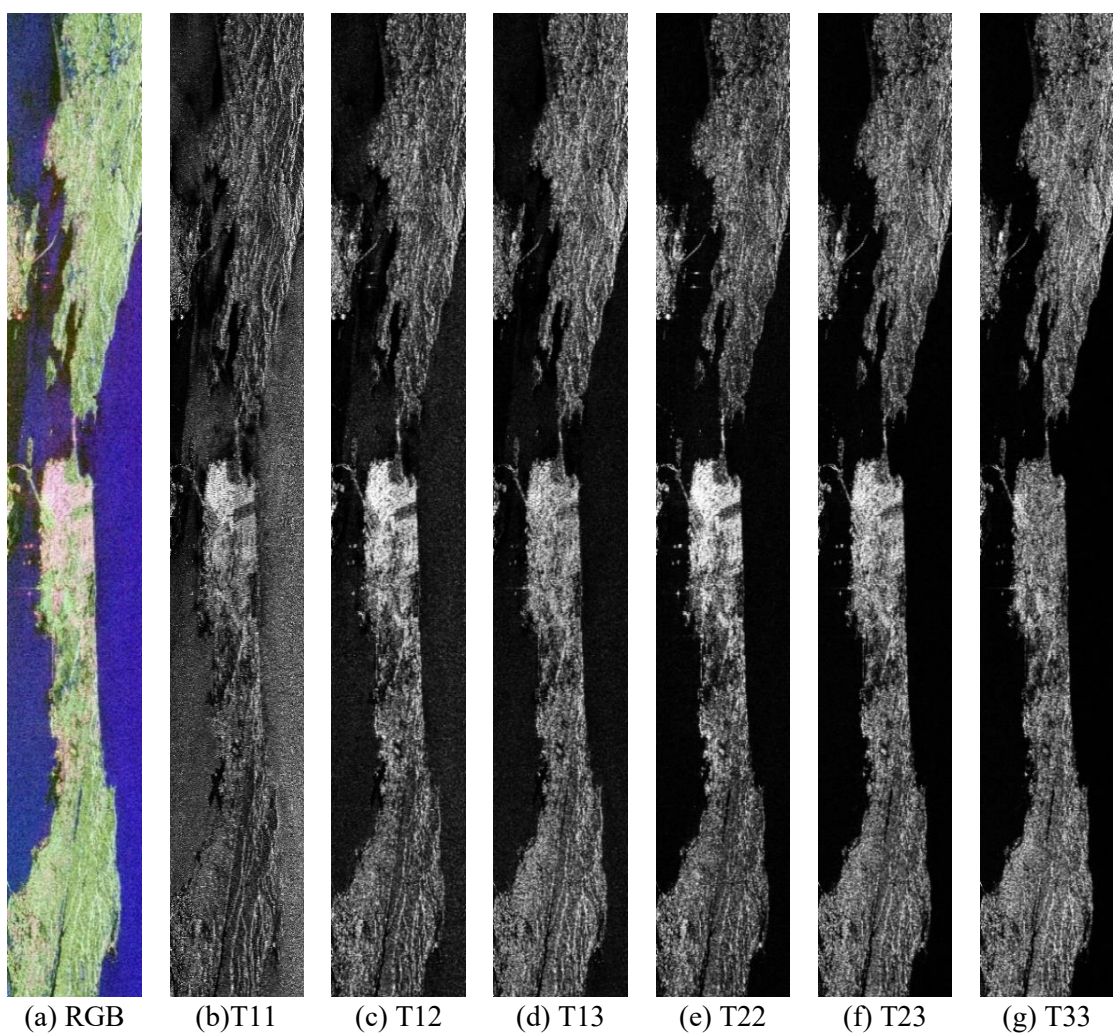
Fig. 3.7 Pauli composition and T3 matrix elements (T11, T12, T21, T22, T23, and T33) of L-band Quad Pol. PolSAR data

(a) Double-bounce scattering (b)Volume scattering component c)Surface scattering component
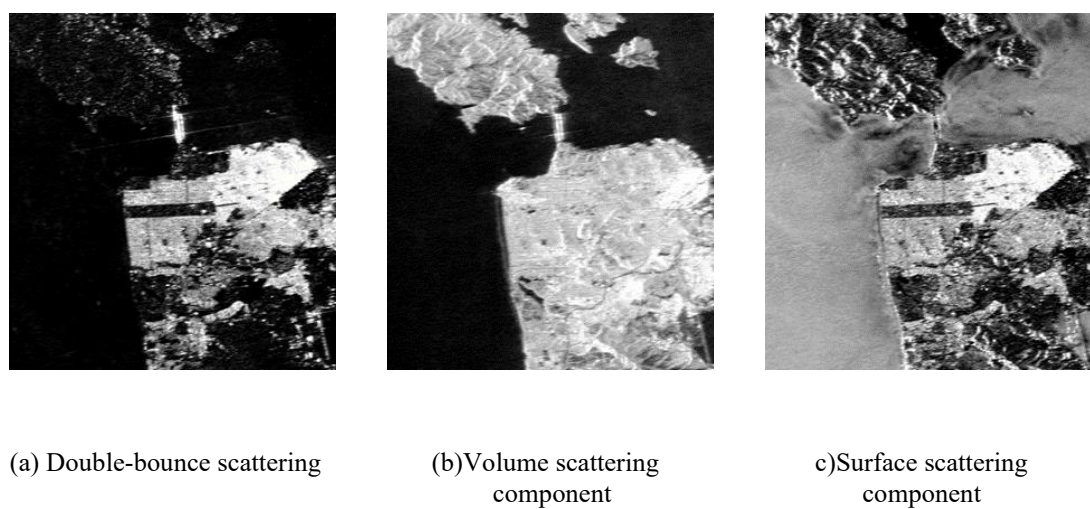
Fig.3.8 Three component Hybrid decomposition of L-band San Francisco image

indicating the cross-coupling of double bounce scattering in the decomposed image of surface bounce. The matrix element T21 is overestimated inside Fig. 3.6 (b). It indicates the overestimation of the double-bounce scattering component at the expense of surface and volume scattering components.
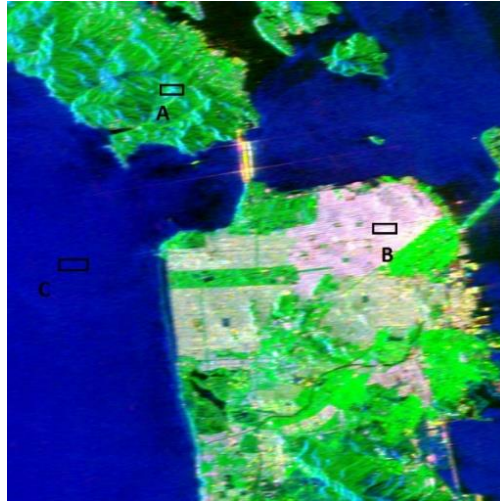
Fig. 3.9 FCC Hybrid three component decomposition image L-band ALOS image (red: double-bounce scattering, green: volume scattering, blue: surface scattering)

The quantitative analysis has been carried out in terms of normalized scattering powers mean for the three surface patches. The mean scattering power for three surface patches, forest (A), man-made structure (B), and water (C) are evaluated for both decomposition techniques (Fig. 3.7). The means of normalised power of surface scattering (m_s), double-bounce scattering (m_d), and volume scattering (m_v) are calculated and shown in Table 3.3.

Table 3.3 clearly indicated that hybrid decomposition reduces the overestimation of cross-polarisation coupling in comparison to freeman decomposition. Surface scattering power clearly dominated in patch C in both decomposition model, there is minimal

intermixing of cross polarisation scattering components, the Fig. 3.5 (b) also supports the clear dominance of surface scattering component.

Table 3.3 Scattering power components for L-band SAR data

Scattering component	Decomposition Techniques	Patch-A (vegetation)	Patch-B (man-made structure)	Patch-C (water)
Surface Scattering	FDD	0.2590	0.1750	0.9010
(m_s)	Hybrid decomposition	0.2788	0.2155	0.9505
Double-bounce	FDD	0.3255	0.5325	0.0595
Scattering (m_d)	Hybrid decomposition	0.3088	0.6755	0.0325
Volume Scattering	FDD	0.4155	0.2925	0.0395
(m_v)	Hybrid decomposition	0.4124	0.1090	0.0170

Table 3.3 shows that patch B, intermixing of scattering component is clearly visible in FDD (volume scattering power m_v mixed with m_s). This intermixing of component is significantly reduced by hybrid decomposition approach. In case of patch A, intermixing of scattering power components is maximum for both decomposition approach. However, the hybrid decomposition method shows better result in discriminating m_s, m_d, and m_v components. From Table 3.3, hybrid decomposition apparently improves the detection of man-made and natural objects.

The hybrid PolSAR decomposition outperforms traditional Freeman-Durden or Yamaguchi models alone by combining their strengths, resulting in better scattering discrimination and classification accuracy.

3.5.1.2 C-band radarsat-2

The C-band San Francisco image contains the same geographical area taken here to analyse improvement in detecting man-made and natural objects using polarimetric

decomposition, as presented in Section 3.5.1.1. Fig. 3.8 (a) displays the multilook (row=2, column=1) Pauli RGB composition of raw C-band data. The coherency matrix T3 has been generated, and its matrix elements T11, T12, T21, T22, T23, and T33 have been shown in Figs. 3.8 (b)-(g), respectively. From Fig. 3.8 (e), a double-bounce element T22 is coupled with T23. An overestimation of volume scattering is visible in the T11 element.

A study region is cropped from raw data of C-band PolSAR consisting of man-made and natural objects to reduce computation complexity and storage. The hybrid decomposition approach (as mentioned in Section 3.3.1) is compared with FDD to show the improvement in the reduction of overestimation of the polarisation scattering component. Fig. 3.9 shows the three-component hybrid decomposition of PolSAR data. For visualization, the FCC decomposed image of the research area by the hybrid decomposition method is shown in Fig. 3.10.

Fig. 3.9 (a) indicates the double-bounce scattering dominance in the golden-gate bridge region; it simply shows the existence of a man-made object. In Fig. 3.9(b), the volume scattering component is coupled with double-bounce scattering, simply indicating cross-polarisation coupling of T23 element. The overestimation of double-bounce is visible in C-band data.

The quantitative analysis has been carried out in terms of normalized scattering powers, similar to Section 3.5.1.1 and for the three surface patches. Table 3.4 shows the value of scattering power for all three components used in this research.

Table 3.4 shows that both decomposition methods compute water bodies (patch C). Like L-band analysis, hybrid decomposition reduces the overestimation and cross-polarisation of scattering components. Table 3.4 shows a cross-polarization coupling at patch B. An overestimation of T12 and T32 is computed into patch B. Patch A, vegetation,

indicates the cross-polarization coupling of surface and double bounce scattering at volume scattering. In urban environment, the polarization orientation shift is instigated by the presence of oriented man-made structures. The term Real(T23) is linked to these shifts in polarization orientation.

(a) Pauli Composition   (b) T11   (c) T12   (d) T13

(e) T22   (f) T23   (g) T33
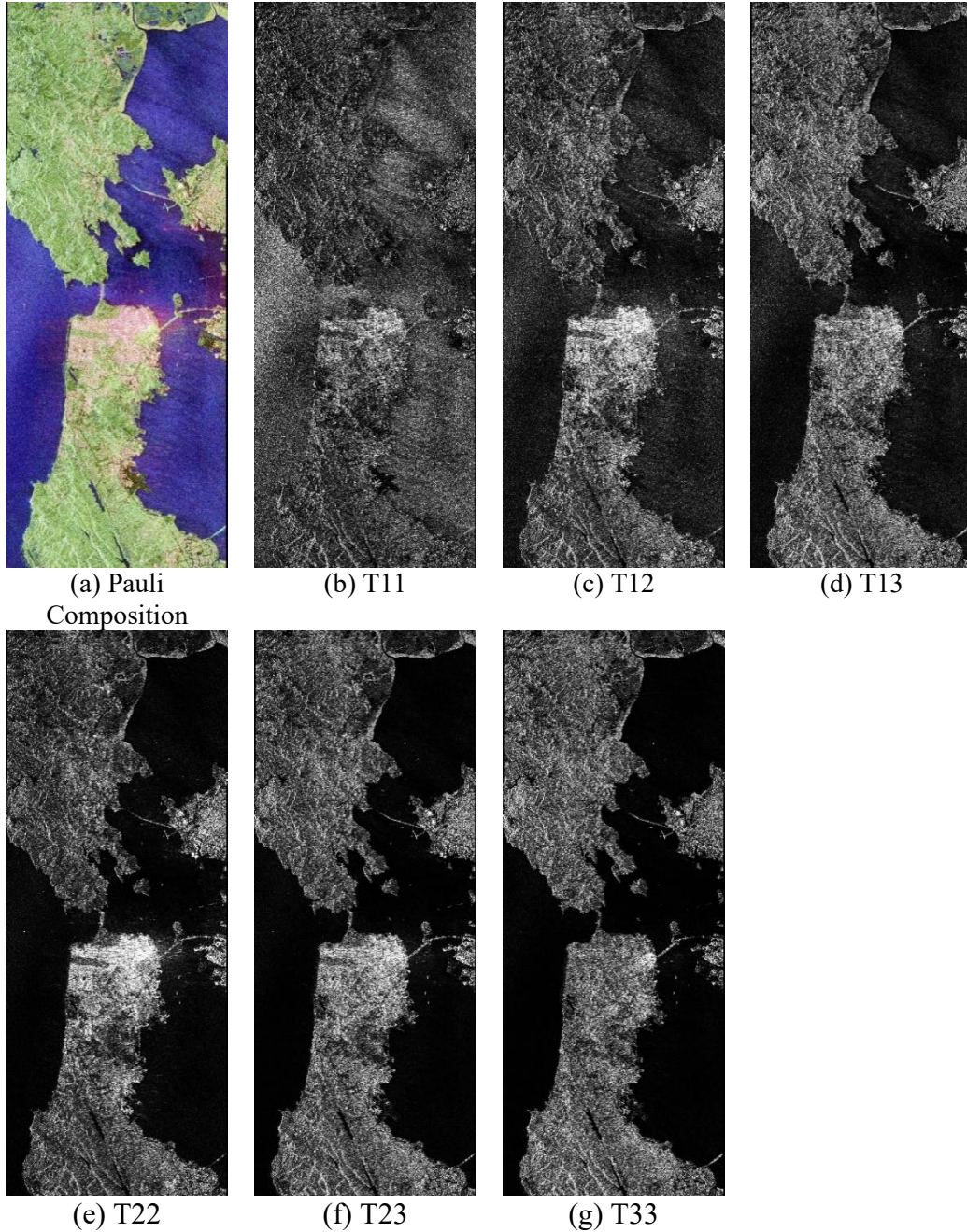
Fig. 3.10 Pauli composition and [T3] matrix elements [T11, T12, T21, T22, T23, and T33] of C-band Quad Pol. PolSAR data

(a) Double-bounce scattering   (b)Volume scattering component   c) Surface scattering
                                                                        component
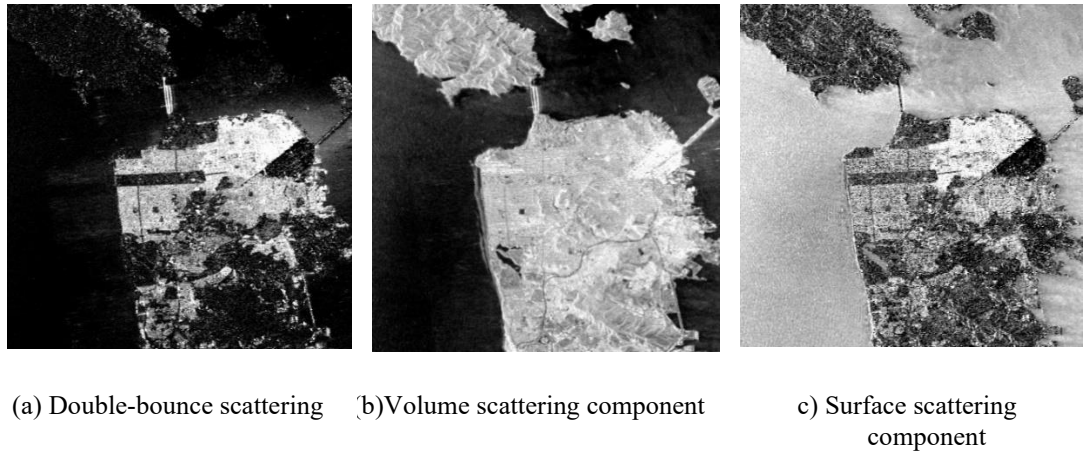
Fig.3.11 Three component Hybrid decomposition of C-band San Francisco image

Fig. 3.12 C-band FCC Hybrid three component decomposition image

Similar to analysis of L-band decomposition, the hybrid decomposition model significantly reduces the overestimation of scattering components in all three patches in comparison to the FDD method. Hence, the hybrid decomposition method apparently improves the detection of man-made and natural objects.

3.5.2 Selection of fusion parameters of L- and C-band data

From Table 3.3 and Fig. 3.7, decomposed L-band data is affected by overestimating surface and volume scattering. A coupling of cross-polarisation surface and volume scattering power appears. However, double-bounce scattering component

power dominates the result. An overestimation of double-bounce scattering components appears in patches B and C.

<div align="center">

Table 3.4 Scattering power components for C-band SAR data

</div>

Scattering component	Decomposition Techniques	Patch-A (vegetation)	Patch-B (man-made structure)	Patch-C (water)
Surface Scattering (m_s)	FDD	0.2060	0.3170	0.9125
	Hybrid decomposition	0.2144	0.3125	0.9550
Double-bounce Scattering (m_d)	FDD	0.3225	0.4385	0.0395
	Hybrid decomposition	0.2542	0.4515	0.0175
Volume Scattering (m_v)	FDD	0.4715	0.2445	0.0480
	Hybrid decomposition	0.5314	0.2335	0.0270

In contrast to the L-band, the surface and volume scattering power dominates in the analysis of decomposed C-band data, as seen in Table 3.4 and Fig. 3.10. Patch A is the cross-polarisation coupling of surface and volume scattering. At the same time, patches B and C have less cross-polarisation coupled.

As surface and volume scattering of the C-band are dominated in the hybrid decomposition image, this result supports the theoretical model due to the short wave of the C-band. The volume scattering component is prominently dominant in the decomposed images. As the C-band PolSAR image has fewer negative power pixels (as two scattering components dominate), two scattering components, i.e. surface scattering component and volume scattering component, have been taken as fusion parameters. In the L-band, only double-bounce scattering components dominate the results. Hence, only the double-bounce scattering component has been selected as a fusion parameter.

3.5.3 Analysis of fusion of C-band and L-band PolSAR data

As discussed in Sections 3.5.1 and 3.5.2, the hybrid decomposition of PolSAR data improves the detection of man-made and natural objects. But it is also reported that there is cross-polarisation of scattering components; to reduce this cross-coupling of scattering components, fusion of L- and C- bands is done.

Both hybrids decompose images and are preprocessed before the fusion. All the preprocessing steps are mentioned in Section 3.4. The PCA fusion algorithms are utilized here to fuse the double-bounce component of the L-band with the surface and volume scattering component of the C-band data. Fig. 3.11 displays the outcome of the PCA fusion approach.
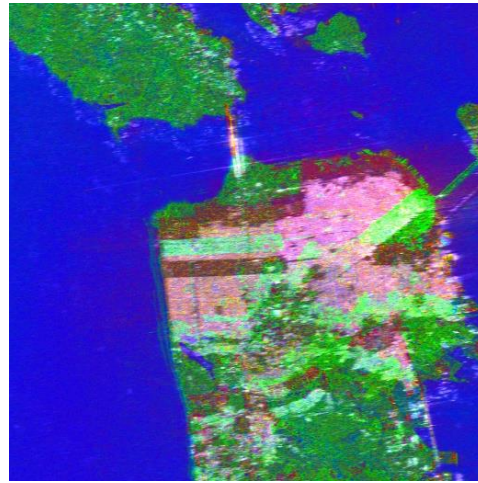
Fig. 3.13 PCA fusion image of L- and C- band image

To show the improvement after the fusion, ALOS, RADARSAT-2, and fusion images are SVM classified for detecting three surface classes, i.e. man-made structure, vegetation, and water body. Fig. 3.12 shows the classified images of (a) L-band, (b) C-band, and (c) PCA fusion image. All the images use the same set of training pixels; Fig 3.12 (d) shows the pixel cluster used for this study.

<div align="center">

(a) ALOS   (b) RADARSAT-2

(c) Fusion image   (d) Training cluster

</div>
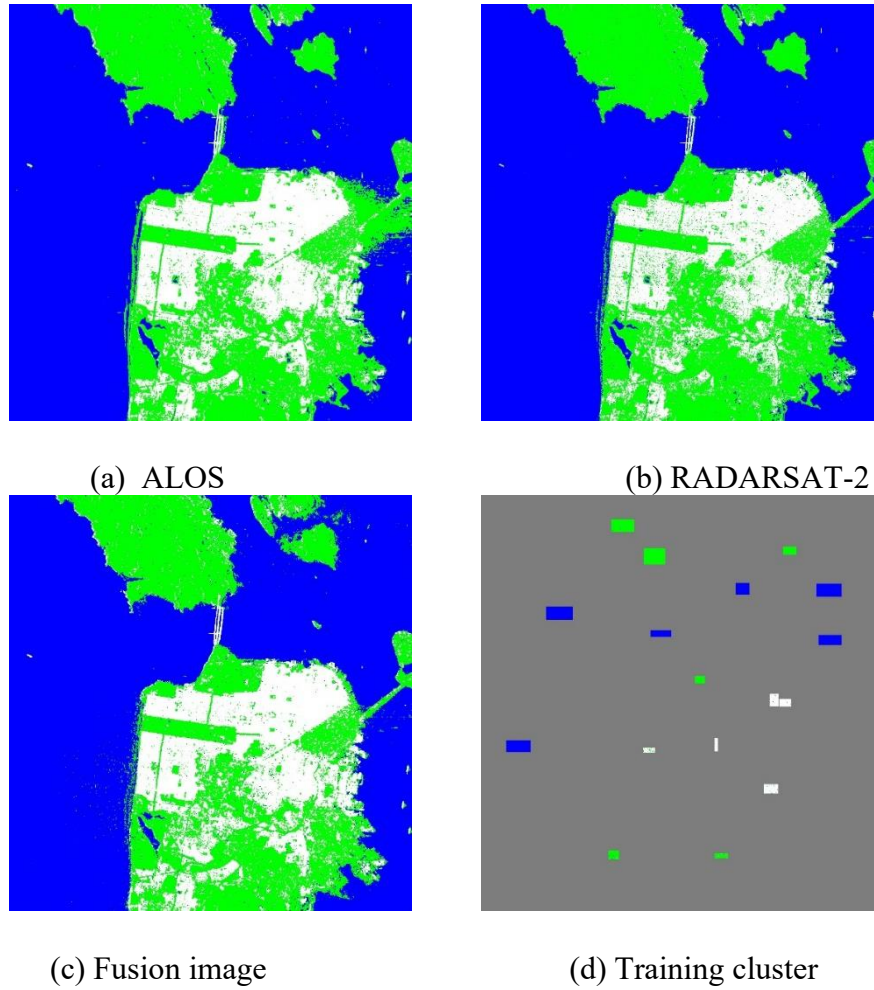
Fig. 3.14 SVM classification of Man-made structure, vegetation, and water (a) L-band, (b) C-band, (c) Classification of PCA fusion image of L-and C-band, and (d) SVM colormap cluster (white- manmade structure, green- vegetation and, blue- water bodies)

Table 3.5 summarises the classification outcome of all the images here. The accuracy of the L-band PolSAR image is less for vegetation (volume scattering) and water body (surface scattering) than the C-band image. The accuracy of the C-band is less for man-made structures in contrast to the L-band image. The fusion image has higher accuracy in all three classes than the L- and C-band images. Fusion image reduces the cross-polarization coupling, improving all three scattering components. The SVM classification shows that a fusion of L- and C- band images enhance the detection of man-made and natural objects.

Table 3.5 SVM Classification accuracy (%) of L-band, C-band and, PCA fusion image

Image	Vegetation	Man-made structure	Water
L-band	94.50	95.74	98.40
C-band	97.28	93.08	99.85
Fusion image	98.75	98.27	100

3.6   Conclusion

This chapter points out the detection and categorization of surface-level man-made and natural targets, which are essential for surveillance, border control, and environmental monitoring in cluttered environments. This study is based on surface scattering components and their decomposition to improve the detection of man-made and natural objects. A hybrid PTD theorem has decomposed the L- and C- band images into surface, double-bounce and volume scattering. The separation of three scattering components has been taken in this study toimprove man-made and natural object detection. This improvement is achieved by mitigating the issue of overestimation in scattering components. It is found that a significant cross-polarization coupling among the three components exists. Experiments have been done with L- and C- band SAR images individually, and their ability to reduce cross-polarisation power has been assessed through the hybrid decomposition method. The dominant scattering component is selected based on the decomposed image of the PolSAR image and mean power scattering values.

A fusion approach is proposed in this study to remove the overestimation of scattering components. The surface and volume scattering of C-band data and a double-bounce component of L-band data are fused with the PCA algorithm. The man-made and

natural objects are classified using the SVM classifier before and after fusing L- and C-band San Francisco city-data. The result shows that the fusion approach enhances the detection of man-made and natural objects.

Therefore, this chapter has an important contribution to make toward the ultimate goal of designing next-generation detection methods from remote sensing, which can be effectively applied in real-world applications – like border monitoring, camouflage hide-out, infrastructure mapping, and monitoring enemy terrain – where accurate discrimination of surface characteristics is of critical significance.

Chapter-4

Improvement in Detection of Surface Objects using Fusion of Optical and Microwave Data

4.1 Introduction and problem definition

In recent decades, multi-sensor satellite image fusion has received considerable attention in remote sensing applications ranging from surface object detection, urban mapping, change detection, military applications, flood mapping, and agricultural applications [7][9]. Multi-sensor image fusion strategies focus on exploiting the image from different regions of the EM spectrum to achieve the desired result, which is impossible using an individual sensor in terms of detection and identification accuracy [10] [165][166]. Multi-sensor fused data are also used to improve various image processing steps such as geo-registration, image sharpening, feature extraction, image segmentation, image change detection, and distinguishing natural and man-made objects [10][167]. With recent research advancements and the availability of airborne and space-borne remote sensing images, multi-sensor data fusion is increasingly being emphasised.

4.1.1 Multi-sensor fusion

Many remote sensing-related problems are being addressed by fusing data acquired from active and passive remote sensors, which otherwise was impossible using either of the sensors [98]. Microwave remote sensing (especially SAR) exhibits all-time all-weather characteristics, which makes them suitable for combining with other diverse datasets, such as Multispectral, Hyperspectral, Lidar, etc., to embed the complementary information into the dataset [9][10].

Optical images contain details about the reflecting and emissive properties of surface objects, whereas microwave images contain information about the texture, roughness, and dielectric characteristics of objects [3] [23]. Two differently constituted objects may look similar in Optical imagery despite difference in their spectral characteristics. However, SAR imagery which is not sensitive to spectral characteristics but is capable of assessing other object parameters such as its dielectric constant, texture *etc* may help distinguish the two objects. Similarly, optical imagery is frequently affected by adverse climates and absence of sunlight during night-time. In contrast, SAR imagery is capable of detecting the physical attributes of the viewed scene.

At the same time, optical data is considerably simpler for human operators to understand and generally offers more information [53]. SAR data, however, includes amplitude and phase information, allowing for a high-precision assessment of 3D topography and deformations. Due to the non-overlapping nature of these constraints, SAR and Optical imaging provide complementary information. The fusion of these datasets enables the creation of a composite image having high spatial and spectral information. Various researchers have exhibited the benefits of fusing an optical image with a SAR image [21][92].

The complementary nature of these two data types is hypothesized to provide enhanced information on landscape objects. For example, optical energy reflected by vegetation is dependent on leaf structure, pigmentation and moisture. In contrast, SAR data energy scattered by vegetation depends on the size, density, orientation and dielectric properties of elements comparable to the size of the radar wavelength.

Optical products are commonly available as multispectral images consisting of multiple bands of data, which can offer different information on land properties based on

its spectral reflectance, as well as be used to accentuate land cover through various indices. In contrast, radar signals are typically only generated at a single wavelength and interact with structural land properties.

4.1.2 Issues in surface object detection using optical and SAR images

Multisensory image fusion aims to combine complementary information in one image that provides a better understanding of the objects observed. Integrating SAR and optical data is an essential example of utilizing complementary sensor information [94][95][96]. While SAR-optical fusion can provide enhanced information and improve data interpretation, several challenges and issues are associated with this fusion process [168]. Table 4.1 summarises the few prominent issues faced by researchers during the fusion of SAR and Optical data.

Table 4.1 Key issues of SAR and Optical image fusion [9][10][96][98][102]

Fusion Issues	Details
Data availability	For fusion, both sensors' data should be of the same time/day. Generally, limited data (especially open source) is available for fusion which affects the research for limited applications.
Sensor-specific characteristics	SAR and optical sensors have specific characteristics, such as speckle noise in SAR images and atmospheric effects in optical images. These characteristics must be adequately addressed during the fusion process to ensure accurate and reliable results.
Heterogeneous data	SAR and optical images have fundamentally different properties, such as resolution, scale, and spectral characteristics. Integrating these heterogeneous data sources can be challenging and requires careful calibration and pre-processing.

Co-registration	SAR and optical images have differences in geometric and radiometric information, leading to misalignment or misregistration. This misregistration can introduce artifacts and affect the quality of the fused image.
Fusion algorithms	SAR and optical fusion are implemented using PLF, FLF , and DLF techniques. The choice of the fusion algorithm can significantly impact the quality and effectiveness of the fused image. Selecting an appropriate algorithm for a specific application is a challenging task.
Spatial and spectral resolution	SAR images provide high spatial resolution but lack detailed spectral information, while optical images offer rich spectral information but lower spatial resolution. Balancing the preservation of spatial details and spectral fidelity in the fused image is a complex trade-off.
Validation and evaluation	Assessing the accuracy and quality of fusion results is a difficult task. Validating the fused image and comparing it with ground truth or reference data is essential to ensure the reliability of the fusion process. A composite evaluation of fusion data is still a critical issue.
Computation Cost	SAR and optical images often contain giant data sets. Which further increases the amount of data. Reducing this redundancy and computation cost while preserving relevant information is still critical to image fusion.
Compatibility of Fusion algorithm and classification techniques	Classification algorithms are sometimes embedded with the fusion of images. Performance of parametric/nonparametric methods and supervised/unsupervised methods are also application dependent and therefore the performance may vary significantly.

Addressing these challenges requires domain knowledge, advanced algorithms, selection of evaluation metrics and carefully selected pre-processing techniques. Ongoing research aims to improve the fusion methods and develop robust models for SAR and optical image fusion in various applications, such as land cover classification, agricultural monitoring, change detection, and surface and subsurface object detection and recognition [9][11].

The concurrent availability of SAR and optical data can vary depending on the specific satellite missions and data acquisition schedules. SAR and optical sensors operate on different principles and have distinct advantages and limitations, which can affect their availability together. Due to the different imaging capabilities and operating principles, SAR and optical data are often acquired independently. They may be available at different times for a specific location. However, there are efforts to coordinate satellite missions to acquire SAR and optical data in close temporal proximity to facilitate complementary analysis and fusion of the datasets. In recent years, European Space Agency's (ESA) Sentinel-1 and Sentinel-2 missions, are designed to acquire SAR and optical imagery over the same geographic areas in a coordinated manner. While they may not capture data simultaneously, the temporal resolution between acquisitions is usually 12 days. In addition, temporal resolution and open-source data availability are the key advantages of the moderate spatial resolution Sentinel SAR and optical mission satellite. Hence, SAR Sentinel-1A and Optical Sentinel-2A have been utilized in this study to extract man-made and natural objects [10][11].

Pre-processing of SAR data is an essential principal step of the fusion process. Speckle reduction filtering and co-registration are two key pre-processing steps for fusion. SAR data are corrupted due to coherent backscattered signals, i.e., speckle noise.

126

Speckle is generated by the constructive or destructive interference of the coherent returns scattered from terrain elements. Speckle, though a radiometric feature of the imaged object, appears as multiplicative noise statistically independent of the image intensity and as spatially correlated. Speckle noise can be modelled as multiplicative random noise in the spatial domain. A speckle reduction filter can increases the signal-to-noise ratio while preserving the textural information of image. Traditionally, two approaches have been employed for speckle reduction, multi-look processing and adaptive spatial filtering. Multi-look processing entails incoherent blending of multiple looks during SAR image production while adaptive spatial filtering is based on evaluating the local statistics around a specific pixel [165]. The most acclaimed filters in this category are the Lee filter, Refined-Lee filter, Enhanced Frost filter, and many more. Non-local filter algorithms, gaussian denoising [9], and block matching utilizing a 3D filter comprised of non-local filters are recent advances in speckle reduction [10]. Some studies [71] used a CNN technique to filter the SAR and found significant results. The speckle filter window can be any size between 3×3 and 33×33, with an odd number of cells arranged in both directions [98]. Depending on how complicated the filter's algorithm is, a larger filter window means a larger portion of the image will be used for calculation, which takes more time. Important details will be lost due to oversmoothing if the filter window is too large. Conversely, speckle reduction could not work well if the filter window was too tiny. In the conditions under consideration, a 3×3 or a 7×7 filter window typically produces good results but needs to be explored.

The technique of geometrically aligning SAR and optical images is known as co-registration. Chen *et al.* (2020) [81] presents a review of image registration methods used in remote sensing. SAR and optical sensor co-registration are challenging tasks and

another significant source of fusion errors. Though georeferenced, images captured with different sensors suffer from an issue of poor alignment since the data captured at the instant of two satellites are different, they only sometimes trend differently [81]. Generally, image fusion techniques can be divided into three different processing levels: the pixel level, the feature level and the decision level [9]. Pixel-level fusion (PLF) is performed at the lowest processing level on a pixel-by-pixel basis. Feature-level fusion requires extracting features depending on their surroundings, such as the intensities of pixels, textures, and shapes. Decision-level fusion combines information at a higher interpretation level, merging the results from multiple algorithms to yield a final fused decision [10]. Despite computationally hectic and time-consuming tasks, PLF contains the maximum information available in raw SAR and Optical data.

Evaluating the quality and performance of SAR-optical PLF techniques is an essential aspect of assessing the effectiveness of the fusion process. The authors have extensively reviewed the available literature and discovered a general need for literature encompassing all essential elements of SAR-optical PLF methods and quality assessments, i.e., subjective, objective, and comprehensive evaluation. Even now, the comprehensive evaluation needs to be explored more to evaluate fusion methods, which leads to further investigation. Therefore, a pivotal study and analyze PLF methods and evaluation methodologies in all three domains (subjective, objective, and comprehensive) for SAR and optical images are needed [9].

Classification of fused SAR and optical data can be challenging due to the increased complexity of the data. The fusion process aims to extract complementary information from both data sources, which can provide more discriminative features for classification. However, handling the increased dimensionality and finding appropriate

classification algorithms that can effectively utilize fused data remains challenging. The analysis of fused data helps in the knowledge and interpretation of the observed region [86]. The performance of fusion and image classification algorithms influence each other, which needs to be explored.

For surface object distinction, several classification methods are available, each with a unique statistical strategy, benefits, and drawbacks. Therefore, it is imperative to examine which classification method can manage the high volume of features that arises from introducing an ideal mix of picture fusion with surface/landscape object detection/classification and the non-normal distribution characteristic of SAR data.

The fusion procedure has been usually embedded into the classification procedure in different machine learning methods that fused the SAR and optical data differently. Komiel *et al*. (2015)[169], investigated the assessment of image classification techniques when combined with an image fusion technique for detecting changes in surface water. The proposed approach given by Komiel *et al.* (2015)[169], shows significant improvement in the detection of change in surface water after fusing multitemporal Landsat optical images. The quality and nature of extracted information from the SAR and Optical fused data are vigorously impacted by the classification techniques attributes [169]. Various researchers presented and evaluated the separate investigation of image fusion algorithms and image classification techniques, and significant results have been achieved [165]. Much research focuses on the performance of image classification techniques and image fusion algorithms separately [170], so a combined approach of image classification methods and image fusion algorithms can be explored.

Based on the preceding literature review, the following specific objectives have been considered:

(i) To assess the impact of speckle filtering algorithm and their window size on the fusion of SAR and optical data.

(ii) To assess the fusion techniques through a subjective, objective, and a proposed comprehensive approach for SAR and optical fusion data.

(iii) To Explore the impact of image fusion on image classification techniques.

(iv) To explore the various combinations of fusion and classification techniques to achieve an optimal combination for accuracy improvement in classification.

4.2 Data Set and study area

4. 2.1 Study site

The Mathura-Agra Region of Uttar Pradesh, India, has been chosen as a study site. The Indian government has selected Mathura as a heritage city under a heritage development plan. Mathura city has landscape coordinates at 27º29'33''N 77º40'25'' E, and its elevation is around 174 meters (571 feet) above sea level. The Yamuna River flows through the city of Mathura and its surroundings. This region is also the centre of attraction for environmental enthusiasts for its proximity to Keoladeo National Park, Bharatpur. Keetham Lake and Sur Sarovar Bird Sanctuary are other significant environmentally rich sites in this study area. Mathura Petroleum Refinery is a significant man-made industrial establishment in this region. The climate of Mathura has a humid subtropical climate. There are several issues that the region is facing nowadays due to rapidly increasing urbanization. Farming, barren, and forest land have quickly diminished daily because of urbanization. The district of Mathura is being selected as a study site because of free, open-source data availability, and the region is familiar to the author. This study includes free access to SAR sentinel-1A and optical sentinel-2A images for man-

made and naturals landscape objects. Fig. 4.1 shows the landscape view of the Mathura-Agra region used for this research.

4.2.2 Sentinel-2A Optical data

The Sentinel-2A is a part of the two-satellite constellation program of the European Space Agency (ESA) [171]. The Sentinel-2A multispectral image is freely available through Copernicus open-access hub. A Sentinel-2A, level 1C, top-of-atmosphere image is taken for this study. The Sentinel-2A was captured on October 07, 2017(ESA Sentinel-2A). The Sentinel-2A Multispectral (MS) sensor provides 13 bands in the optical, NIR, shortwave-infrared (SWIR) parts of the electromagnetic band, out of which Band-1, Band-9, and Band-10 have a 60-meter resolution, Bands-(5, 6, 7, 8A, 11) and Band-12 have a 20-meter resolution, Bands-(2,3,4) and Band-8 have a10-meter resolution. Fig. 4.1a shows a false-color composite of sentinel-2A multispectral image utilizing Band-3 (Green), Band-4 (Red), and Band-8 (NIR). The followings are the specifications of the Sentinel-2A image:

Data Format = JPEG 2000

Revisit Time=10 days

Swath Width = 290 km

Radiometric Resolution= 12 bits per pixel

Data mode= Push-broom mode

4.2.3 Sentinel-1A SAR data set

The SAR Sentinel-1A C-band (5.405 GHz) image is taken as the microwave dataset for this study (ESA Sentinel-1A). The Sentinel-1A is also available freely through Copernicus open-access hub program. Table 4.2 summarises the details of Sentinel-1A SAR dataset.
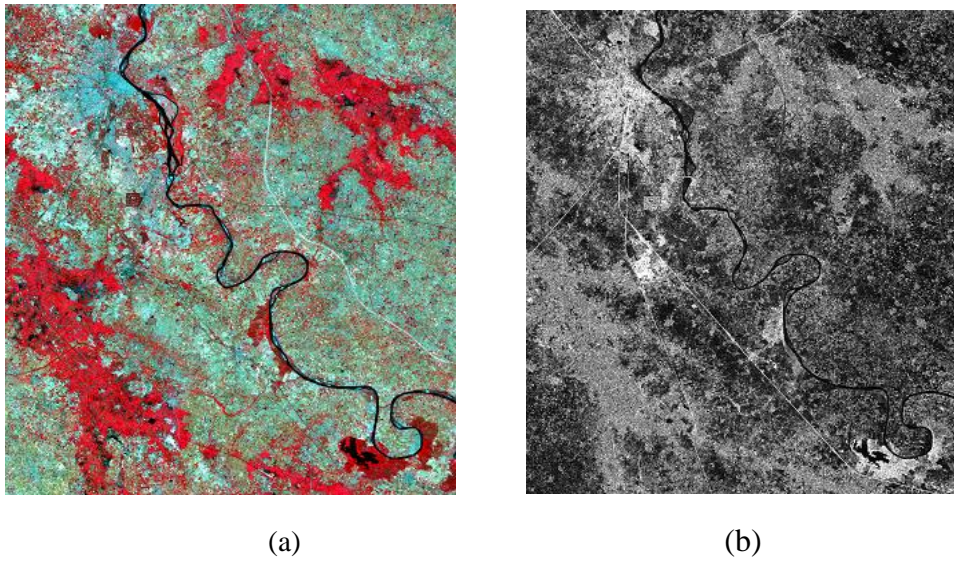
<center>(a)   (b)</center>

Fig. 4.1 (a) Study area of Agra-Mathura region (Optical image) (b) VH polarized SAR image

<center>**Table 4.2**   Specification of sentinel data [171]</center>

Specification	Sentinel-1A SAR	Sentinel-2A Optical
Captured Date	03rd October,2017	07th October,2017
Operating mode	Interferometric Wide swath (IW) mode	-
Frequency, Wavelength	5.405 GHz, 5.4 cm	13 bands
Polarisation mode	VV and VH	-
Revisit Time	12 days	10 days
Swath width	250 km	290 km
Radiometric Resolution	16- bit	12-bit

4.3 Theoretical background

4.3.1 Image pre-processing

Satellite images must be pre-processed before further utilization in remote sensing applications to enhance image quality, reduce noise, and prepare the data for subsequent analysis tasks. SAR and optical images are separately pre-processed before fusion. The following pre-processing steps have been carried out on the SAR image to enhance feature extraction and make it suitable for fusion with optical data [98][165].

<center>132</center>

- **Radiometric calibration:** SAR data is often affected by radiometric distortions caused by variations in antenna gain, system noise, and other factors. Radiometric calibration corrects these distortions to ensure consistent brightness values across the image. It converts a digital number to sigma naught backscatter. The inverted image is now mapped with map data. The equation of radiometric calibration has been given as follows:

$$\sigma_o = 10 \, log_{10} \left(\frac{DN}{G} \right) + \beta \tag{4.1}$$

  Where σ_o is calibrated backscatter, DN is the digital number received by the unprocessed SAR image, G is the gain or calibration factor, and β is the offset term. The bias and calibration terms are calculated using reference objects such as panels and corner reflectors with known backscatter values.

- **Multilooking:** SAR images are typically formed by combining multiple radar pulses (looks) to improve the signal-to-noise ratio. Multilooking involves averaging neighbouring pixels to reduce speckle noise while sacrificing spatial resolution. The image pixel size is half of the SAR instrument resolution.

- **Speckle Filtering**: Speckle is a multiplicative noise inherent in SAR imagery, which appears as a white patch. Speckle filtering techniques aim to preserve image details while reducing noise. Common approaches include Lee, Frost, and Gamma-MAP filters.

- **Terrain Correction:** SAR signal can be affected by terrain variations leading to radiometric and geometric distortions -Terrain-induced artifacts removed by the Digital Elevation Model (DEM).

Optical data is generally required atmospheric correction and resampling before further analysis. Atmospheric correction compensates for the influence of the Earth's

atmosphere on satellite images. It removes atmospheric effects such as scattering and absorption to retrieve surface reflectance values. Various models and algorithms are used for atmospheric correction, such as dark object subtraction or atmospheric and topographic correction.

4.3.2 Speckle filtering algorithms

SAR images gain a granular look with random spatial variations from speckle. Rather of being noise, speckle is a scattering phenomenon. Because of the great diversity of the SAR-speckled response, comparing intensity to a set threshold for the purpose of discriminating between different natural media typically results in many inaccuracies. [9][10][98].

Standard speckle filters, including Boxcar, Median, Lee, and Gamma, are frequently employed in image processing. Each of these speckle filters does the filtering using either the adequate equivalent number of looks (ENL) of a SAR image to estimate the local noise variance or local statistical data provided in the filter window to determine the noise variance within the filter window. After that, the amount of smoothing required for each speckle image is determined using the predicted noise variance. If an area's intensity is consistent, the noise variance computed from the local filter window is more appropriate [172].

Boxcar averaging filter

It enhances the signal-to-noise ratio by moving an averaging filter over a set of neighbourhood pixels (window). This filter calculates the average value of pixel intensities within the window. Furthermore, it replaces the pixel value at (x, y) with the computed average. It reduces the high-frequency components of the speckle noise, which can result in blurring the image and reducing fine details. For each pixel:

Filtered Image I (m, n) $= \frac{1}{N^2} \sum \sum I(x,y)$ (4.2)

Where (x, y) represents the filter window coordinates, x= 0,1,2,3…...N-1 and y = 0,1,2, 3..…..N-1.

Median filter

The Median filter is more effective than the convolution filter when the goal is to reduce noise and preserve edges simultaneously. It replaces each pixel value of image I(m,n) with the median value of its surrounding pixels. It preserves the fine details and edge better than the Gaussian and mean filters.

Gamma map filter

The Maximum A Posteriori (MAP) filter is employing multiplicative noise model with nonstationary mean and variance parameters. It merge geometric and statistical characteristics to compute the values of the pixel and the average of neighbouring pixels using moving windows. It utilizes a maximum a posteriori estimation to reduce speckle noise. It operates by estimating the image's statistical properties (such as mean, variance, etc.) using a kernel. The filter assumes that the original DN value lies between the DN of the pixel of interest and the average DN of the moving kernel.

Moreover, many speckle reduction filters assume a Gaussian distribution for the speckle noise. The estimated statistical properties are then used to compute the weights for filtering each pixel. Naturally, vegetated areas are more appropriately modelled as having a Gamma distributed cross-section [172]. The Gamma-MAP filter is governed by the following equation:

$$E[I(m, n)]^3 - \bar{I}(x, y) E[I(m, n)]^2 + \sigma (E[I(m, n)] - DN) = 0 \qquad (4.3)$$

Where,

$$E [I (m, n)] = \text{Expected pixel value}$$

$$\bar{I}(x, y) = \text{Local average pixel value}$$

$$\sigma = \text{Variance of noisy image}$$

$$DN = \text{Intensity (Digital number) of noisy image}$$

Lee filter

It is based on local statistics to reduce speckle noise. The specific operation used is a weighted average of the image pixels. The weight is calculated based on the local statistics of the image[172]. Equation 4.3.3 is used to calculate filtered image:

$$E(\tau) = \overline{I(\tau)} - W (\tau) (I(\tau) - \overline{I(\tau)}) \tag{4.4}$$

Here, $E(\tau)$ is estimated value of the filtered image

$I(\tau)$, $\overline{I(\tau)}$ are the noisy image and its mean value respectively

$W(\tau)$ is the weighting function.

$$W(\tau) = \frac{var (\tau)}{(I(\tau))^2 \sigma^2 + var (\tau)} \tag{4.5}$$

$$\text{And } var (\tau) = \frac{\sigma_l^2 + \mu_l^2}{\sigma^2 + 1} - \mu_l^2 \tag{4.6}$$

Where $var(\tau)$ is the variance of the pixel being filtered, σ^2 is the global variance of the noisy image, σ_l^2 and μ_l are local variance and local mean respectively.

Lee- Sigma

It is a nonlinear adaptive filter based on a two-sigma PDF of speckle noise. It estimates the mean, variance, and standard deviation of the noise in a local neighborhood

of each pixel. The filter then replaces the value of each pixel with a weighted average of the pixel value and the mean of the speckle noise in the neighborhood. The adaptive weight is the tradeoff between noise reduction and noise variance.

Filtered value = Local mean + W (τ) * (original value – local value)   (4.7)

W (τ) = 1 – (noise variance/local variance)   (4.8)

Lee-sigma filter is simple in implement and effective in reducing speckle noise.

4.3.3 Image fusion algorithms

Image fusion is a process that merges two or more sensor images to extract additional information [10]. This paper merges the Sentinel-1 SAR image with a Sentinel-2 Multispectral image. PCA, HSV, Brovey Transform and GS Transform fusion methods have been used to detect surface objects/classes. PCA fusion method is discussed in Section 3.3.3, so the rest of the fusion techniques are discussed here[9][81][98].

HSV fusion

HSV is an empirical merging technique for researchers to fuse multispectral and panchromatic imagery and SAR. HSV incorporates the transformation of the RGB bands of the image into HSV colour space. This algorithm divides spectral (hue and saturation) and spatial component (value) data from an optical image. In this algorithm, RGB bands of optical images are transformed into Hue (colour contribution), Saturation (purity of colour), and Value (brightness or intensity) bands, respectively. In the next step, firstly, the histogram of the SAR image and Value band is matched so that both bands' variance and mean are equal. Then, the Value band of HSV is replaced with the SAR band to incorporate spatial information. The inverse transformation is accomplished to get the resultant fused optical imagery from HSV bands. The fundamental restriction of the HSV

transform is that it can only change the three bands of the MS image. However, the higher number of multispectral bands can be incorporated by doing multiple HSV transformations [9][173].

Brovey Transform (BT)

BT uses arithmetic combinations of bands to normalize multispectral bands used for colour display. The resulting normalized bands are then multiplied by the desired image (SAR) to fuse to the multispectral bands [9].

$$BT1 = \frac{DN_{MS1}}{DN_{MS1}+DN_{MS2}+DN_{MS3}} DN_{SAR}$$

$$BT2 = \frac{DN_{MS2}}{DN_{MS1}+DN_{MS2}+DN_{MS3}} DN_{SAR} \qquad (4.9)$$

$$BT3 = \frac{DN_{MS3}}{DN_{MS1}+DN_{MS2}+DN_{MS3}} DN_{SAR}$$

BTi is Brovey fused bands, are multispectral bands, and is the SAR image utilized for fusion with multispectral image, which incorporates spatial information multispectral image. The BT method is relatively easy to compute; however, literature reported that using the method for pixel-level fusion applications did not return desired results.

Gram-Schmidt (GS) Transform

This GS transform is much like the PCA algorithm approach. Initially, SAR intensity imagery is a histogram matched to the lower spatial resolution optical bands. So is achieved by equating the bands of the optical data set. Now, GS orthogonalization is achieved on the matched SAR band and the optical bands, where a simulated SAR image has been employed as a primary band of transform [174]. After that, the SAR image is replaced by the first GS transform band. At last, the reverse GS transformation is accomplished to achieve the fused multispectral image [175].

4.3.4 Image classification

Satellite image classification is the process of categorizing satellite images into different classes or categories based on the content or features present in the images. Extract relevant features from the satellite images that can differentiate between different classes. These features can be spectral, textural, or structural attributes derived from the image pixels or regions of interest (ROIs). Manually label a subset of satellite images to create a training dataset. The training dataset should contain representative examples from each class to classify. The labeled images should be paired with their corresponding class labels. SVM and maximum likelihood (ML) algorithms classify natural and man-made classes. Table 4.3 shows the class definitions of various classes utilized in this research.

Table 4.3 Class definition

Class	Description
Man-made structure	Human made structure (buildings, bridges, roads, impervious surfaces etc.)
Water	Water bodies (Ocean, lakes, pond, rivers etc.)
Agri. Veg.	Low vegetation (natural grass, pastures, crops etc.)
Forest	Wood veg. (Coniferous forests, dense shrubs etc.)
Bare soil	Planes devoid Veg. (rocks, karst plains, soil etc.)

4.4 Methodology

The following image processing tasks must be executed to accomplish the objectives of this research: collection of SAR and optical images, pre-processing of SAR and optical images, speckle filtering of SAR data, reprojection to common coordinates, implementation of fusion algorithms, detection/classification of surface objects and

validation and assessment of accuracy. Fig. 4.2 shows the workflow of this research from image pre-processing to validation and assessments.

4.4.1 Preprocessing of Satellite Imagery

SAR and optical images have been downloaded from the Sentinel mission of the European Space Agency (ESA). In further data processing, preprocessing of the SAR and optical images has been initially conducted separately, followed by reprojecting both images onto the same coordinate system.

4.4.1.1 SAR imagery preprocessing

Due to the complex nature and physical properties of SAR images, SAR image processing is one of the most critical steps for further processing of data. The following pre-processing steps are implemented: calibration, speckle noise reduction, and terrain correction [176].

4.4.1.2 Optical image preprocessing

Optical image pre-processing was performed to get bottom of atmospheric (BOA) Level-2 optical image from the Sentinel-2 level-1C top of atmospheric (TOA) data. Atmospheric correction is being performed on the SEN2COR platform developed by the European Space Agency. Green, Red and NIR bands have been used in this research. The nearest neighbour-based resampling of 10x10 meter-square has been implemented to multispectral bands.

Before fusion, SAR and multispectral bands have been terrain-corrected using a 30m SRTM digital elevation model and reprojected to WGS-84, UTM zone- 43.
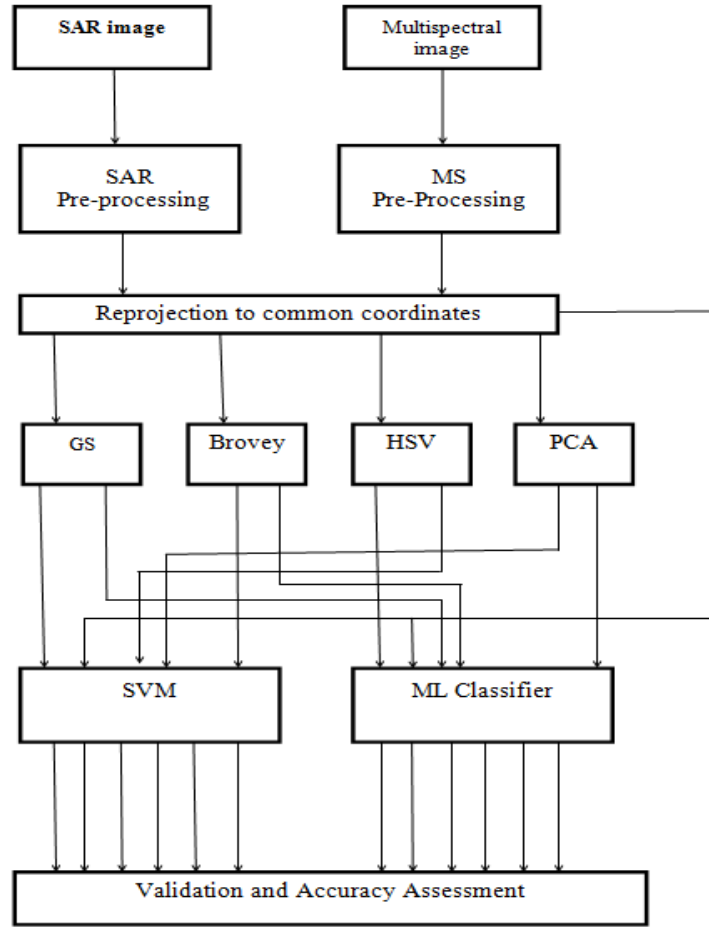
Fig.4.2 Flow diagram showing the methodology

4.4.2 Speckle filter

After preprocessing, impact of speckle filter on image fusion algorithms has been evaluated. To evaluate speckle filtering, various statistical parameter has been calculated [177]. Fig. 4.3 shows the workflow of the task for the speckle filtering impact evaluation to fusion image.

In this study, the statistical assessment parameters that are used to evaluate the speckle filter are variance, mean value, standard deviation, and equivalent number of looks (ENL). In composite analysis, the effect of speckle filtering has been analysed before and after fusion and a conclusion has been drawn based on this task. This study

141

evaluated the influence of various speckle filtering methods (with different window sizes) for SAR and optical image fusion. Box car, Median filter, Gamma map filter, Lee filter and Lee Sigma (with window sizes 5×5 and 7×7) have been evaluated for SAR and optical fusion. These fives speckle filters have been applied to Sentinel-1A SAR images before fusion. All SAR speckle-filtered images have been subjected to fusion with optical images.
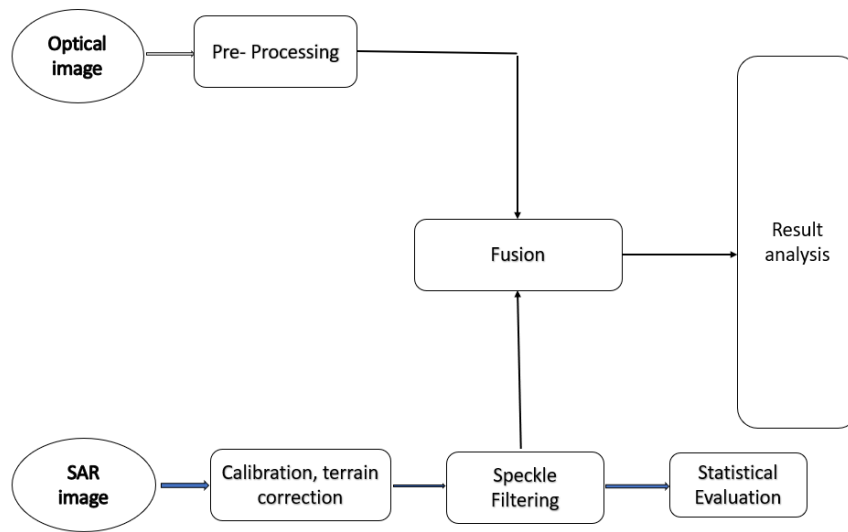

Fig. 4.3 Flowchart for Speckle filter impact analysis

4.4.3 Image fusion methods

The one of the aims of this research is to evaluate various established classification and fusion algorithms and explore the impact of fusion techniques on image classification techniques. Four established fusion techniques, H-S-V fusion, Brovey Transform, PCA, and GS Transform, have been performed on the SAR optical dataset. As the accuracy of MS image is quite good, and interpretation of MS image is much easier than SAR image, the MS image has been selected for reference image for the fusion process.

SAR is single band data with VV and VH polarisation. The VV-SAR image highlights the linear features and VH-SAR image highlights Volume features. Ability to

discriminate prominent features of surface objects, VH-SAR image has been taken for fusion with optical image.

In this study, HSV transformation is being performed on three MS bands (Green, Red, and NIR) and the VH polarized SAR image. In GS transformation, three bands (Green, Red, and NIR) of MS and VH-polarized SAR data are utilised. In PCA, the first PC is replaced by VH polarized SAR images, and all other parameters are default values. Brovey transform is used as a mathematical combination of multispectral and SAR images. Here fused band was reconstructed with the multiplication of VH polarized SAR image and normalized MS bands.

4.4.4 Evaluation of SAR-optical fusion image

SAR is a complex image, and its fusion with optical data leads to more complicated data processing. The fusion quality evaluation is an important task, and numerous researchers exhibit various models to evaluate the fused image. An evaluation of the quality of the fusion image is assessed through two approaches, i.e. subjective and objective assessment. In this research, a comprehensive (application-based) method is proposed and evaluated. The selected evaluation metrics such as Structural Similarity Index (SSIM), Correlation Coefficient (CC), and Entropy, have been chosen to objectively assess the quality and effectiveness of image fusion.

All fused images are evaluated using objective quality metrics: correlation coefficient (CC), universal quality index (UIQI), structural similarity index measure (SSIM), and mean bias require a reference image, whereas entropy, standard deviation (SD), and mutual information (MI) do not require a reference image.

The comprehensive assessment of fusion methods using SVM classification and the outcome of the assessment in terms of kappa coefficient and accuracy has been taken. surface objects (man-made structures, water, forest, Barren land, and veg. agriculture) have been included in the experiment.

4.4.5 Influence of image fusion approach on image classification techniques

In this subsection, the SVM, Maximum likelihood classifier (ML) methods have been implemented to extract man-made and natural objects. Five landscape/surface objects (Man-made structure, Water, Forest, Barren land, and Veg. Agriculture) have been taken for evaluation of fusion and classification combination. Table 4.4 shows the number of testing and training pixels selected for each class. The training pixels have been selected from optical image with the help of field data observation and google earth imagery. The same sets of testing and training pixels are selected from the SAR and fusion images to demonstrate the improvement in results after fusion. The influence of image fusion on the image classifier is evaluated by the overall accuracy and kappa coefficient for all the possible combinations of fuser and classifier. Supervised classification ML and SVM have been implemented to the resultant fusion methods outcome. Here, Brovey, GS, PCA and HSV fusion techniques has been implemented. For SVM, the penalty parameter was set to 100, and a default value (i.e., 0.143) was set for Gamma in the kernel function. The pyramid parameter of SVM was set to zero. A total of eight combinations of Fuser and Classifier have been evaluated for extracting the surface Objects/classes. The combinations are: (i) HSV-SVM (ii) Gram-Schmidt – SVM (iii) PCA- SVM (iv) Brovey- SVM (v) HSV-ML (vi) Gram-Schmidt – MLC (vii) PCA – ML and (viii) Brovey- ML.

Table 4.4 Class-wise training and testing pixels used for evaluation

Class	Map color	Training Pixel	Test Pixel
Man-made structure	⬜	857	662
Water	⬜	927	827
Forest	⬜	983	832
Barren land	⬜	1070	913
Veg. Agriculture	⬜	956	638

4.5 Results and discussion

Sentinel-1A SAR images have been pre-processed (calibration, speckle filtering and terrain correction) with sentinel application platform (SNAP) software, whereas sentinel-2A optical image is pre-processed on the SEN2SOR processor of ESA. SAR data's radiometric and terrain calibration is performed earlier in the composite study area for further processing, whereas atmospheric correction is performed for optical data. The results of this research are further discussed in subsections to address each sub-objective of this research.
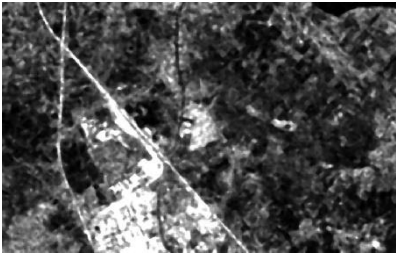
4.5.1 Impact of speckle filtering and its window size on the fusion

This subsection shows the performance of speckle filtering algorithms and their window size to reduce the speckle effect of SAR image, which is subjected to fusion with optical data. A subset of Fig. 4.1 has been chosen for speckle filtering experiments to reduce computation time and storage. The impact of filtering is evaluated before and after the fusion of SAR image. Experiments are performed on the subset of the study area with man-made objects (such as settlements, roads, and rail lines) and natural objects (forests and vegetation). Five established speckle filtering algorithms: box-car, median, gamma-map, Lee, and lee-sigma filter algorithms have been taken for this study. In addition, the

5x5 and 7x7 filter window sizes are taken for the experiments. Fig. 4.4 shows the impact of speckle filtering algorithms on the SAR image before the fusion.

An effective speckle-reducing filter does not significantly impact the average intensity in a homogeneous area. Smooth shrink and image de-blurring have been visual in the box-car and median filters. Lee-sigma and gamma map filters maintain image sharpness and capture details, effectively suppressing speckle noise compared to conventional low-pass smoothing filters. Spatial and multi-look filtering smooths the image and minimizes speckles at the expense of resolution. Table 4.5 shows the measures of statistical parameters of filtered images.

Lee-sigma operates by filtering based on the local statistical value provided in the filter window to compute the noise variance within that window or by estimating the local noise variance using the appropriate equivalent number of looks (ENL) for the study area.

Window size → Filter ↓	5×5	7×7
Box-car		
Median		

Gamma map

Lee
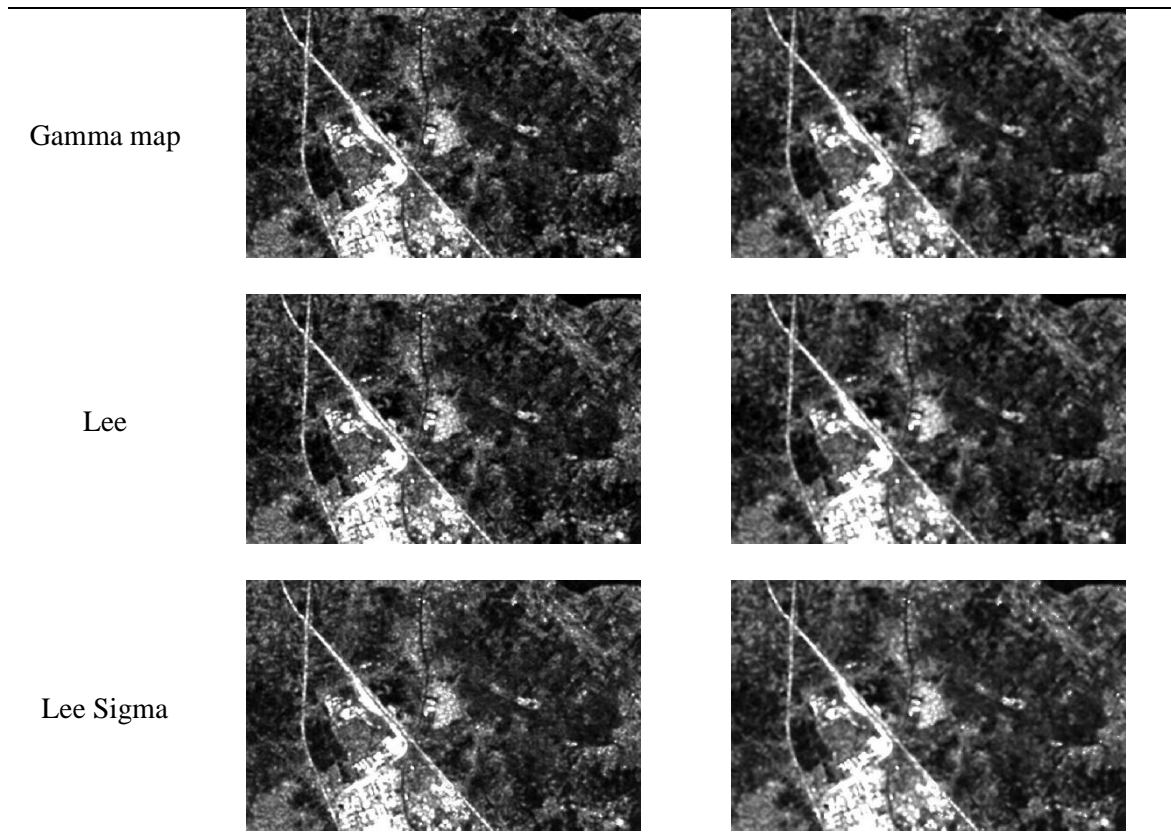
Lee Sigma

Fig. 4.4 Implementation of speckle filter algorithms on SAR image

The lee-sigma filter with a window 7x7 size has shown the highest ENL value. The gamma map filter has the highest standard deviation value, indicating a higher discrimination value. The gamma map filter is more sensitive towards the lower backscatter values. Compared to a window size 7×7, a 5×5 window size has a higher standard deviation value.

Fig. 4.5 offers the performance of speckle filtering algorithms when evaluated with fusion with an optical image. Here, experimental results are presented using Sentinel-1 SAR image fusion with the optical image employing PCA fusion algorithms. In continuous statistical outcomes, lee-sigma and gamma-map filtered fused images show a less deblurred effect than others. Box car, median and Lee filters produce few intermixing of man-made structures with barren land. In contrast, the lee-sigma filter shows promising results by discriminating man-made structures from barren land.

Compared to the 7×7 window size, the 5×5 size preserves textural information. Before fusion, the Lee-sigma and Gamma-map filter with a 7×7 window size gave the best statistical outcomes, whereas, after fusion, the Lee-sigma filter with a 5×5 window size gave better results. Fusion techniques can affect the outcome of speckle filtering. The fusion image indicated that the Lee-sigma filter handled the inherent speckle noise well after the fusion. So, the Lee Sigma filter is used for the rest of the research.

Table 4.5 Statistical measure of Speckle filter

Filter	Window size	Mean	ENL	STD	Variance
Box car	5×5	31.15	0.0004	103.15	44.66
	7×7	33.35	0.0008	96.15	38.55
Median	5×5	32.33	0.0003	109.15	42.15
	7×7	34.56	0.0005	114.15	39.15
Gamma map	5×5	38.15	0.0014	122.33	36.55
	7×7	39.85	0.0020	116.25	32.15
Lee	5×5	-198.15		115.19	
	7×7	-35.27		102.13	
Lee-Sigma	5×5	37.18	0.0018	119.33	42.15
	7×7	39.17	0.0022	116.55	35.67

4.5.2 Assessment of image fusion techniques

An evaluation of the quality of the fusion image is assessed through two approaches, i.e. subjective and objective assessment. In this research, a comprehensive (application-based) method is proposed. Experiments have been conducted for SAR and optical fusion with four fusion techniques: PCA, HSV, BT, and Gram–Schmidt fusion. Here, three bands (NIR, Red, and Green) of Sentinel-2 A multispectral image are being fused with a VH-polarized Sentinel-1A SAR image. The results of these assessment are given in this subsection.
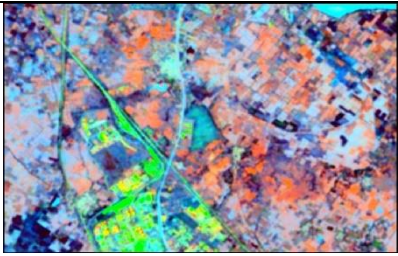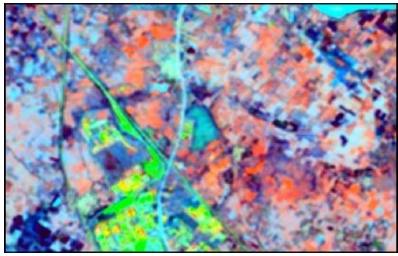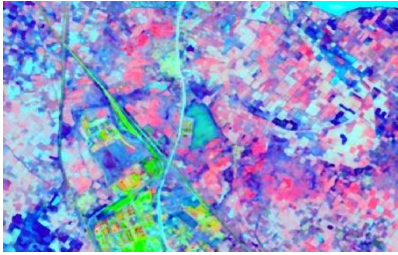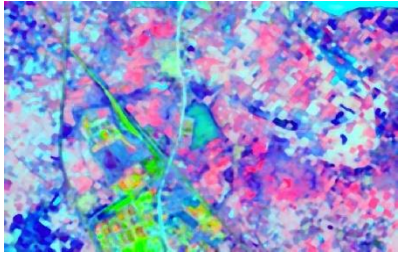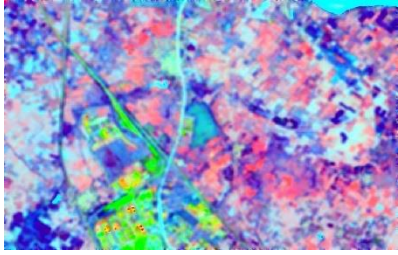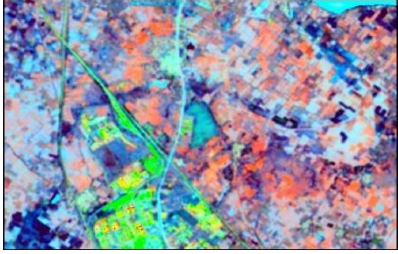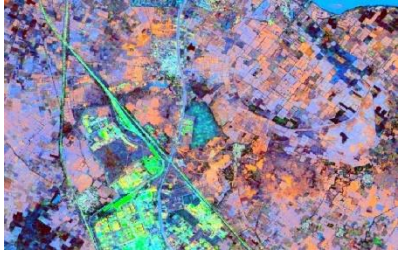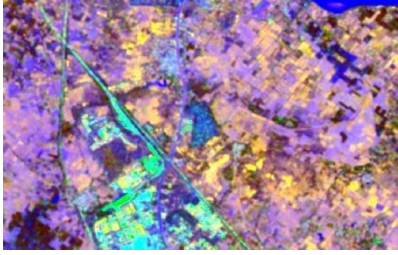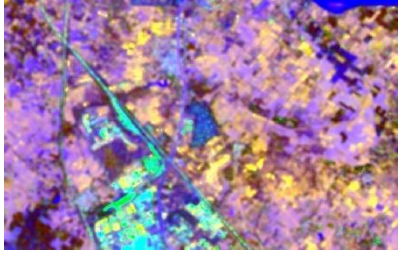
Window → size	5×5	7×7
PCA fusion of Box Car filtered image		
PCA fusion of Median filtered image		
PCA fusion of Gamma map filtered image		
PCA fusion of Lee filtered image		
PCA fusion of Lee sigma filtered image		

Fig. 4.5 SAR and optical image fusion of various speckle filtered images

4.5.2.1 Subjective Assessment

The subjective (visual) results of PCA, HSV, BT, and GS approaches demonstrate that PCA fusion delivers the best fused output of all the investigated methods (Fig. 4.6). The visual findings show that the use of BT and GS fusion methods has resulted in significant spectrum distortion. The findings also show that some texture information accessible in the SAR data is fed into the fused output. The visual findings of HSV fusion show that the outcomes are visually superior to the GS and BT techniques. Some details in the HSV technique are sharper than in PCA, GS, and BT techniques, and Visually, HSV fusion produces a superior fused output. However, simple GS and HSV-based methods have enough room for enhancement, resulting in a spectral mismatch between SAR and optical image distortion.

4.5.2.2 Objective Assessment

Tables 4.6 and 4.7 present the evaluation of some widely used objective metrics. All fused images are evaluated using metrics: CC, UIQI, SSIM, and mean bias require a reference image (Table 4.6), whereas entropy, SD, and MI do not require a reference image (Table 4.7). As evaluated, PCA and GS methods show better results. Among all the methods considered, BT achieved the worst consequences. The CC value of all fusions has little difference. PCA and GS fusion methods result in better metrics values. In the absence of high-resolution reference images, metrics are evaluated using the Wald protocol at reduced resolution [98].

4.5.2.3 Comprehensive Assessment

The visual effect is subjective in nature and vary from researcher to researcher. Objective assessment also shows some ambiguity in feature extraction due to intermixing some classes. To determine the composite evaluation of SAR optical image fusion,
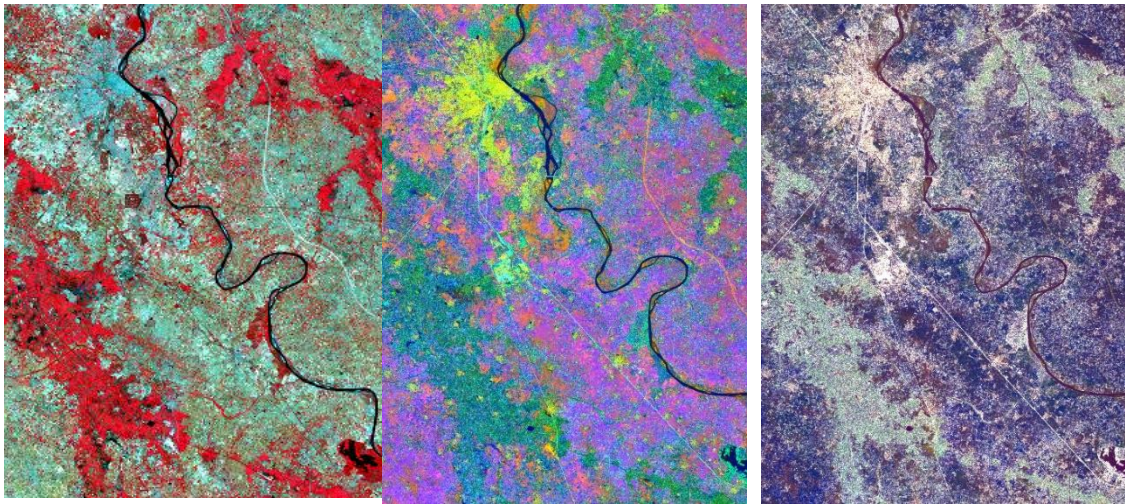
(a) FCC of MS image   (b) PCA   (c) HSV
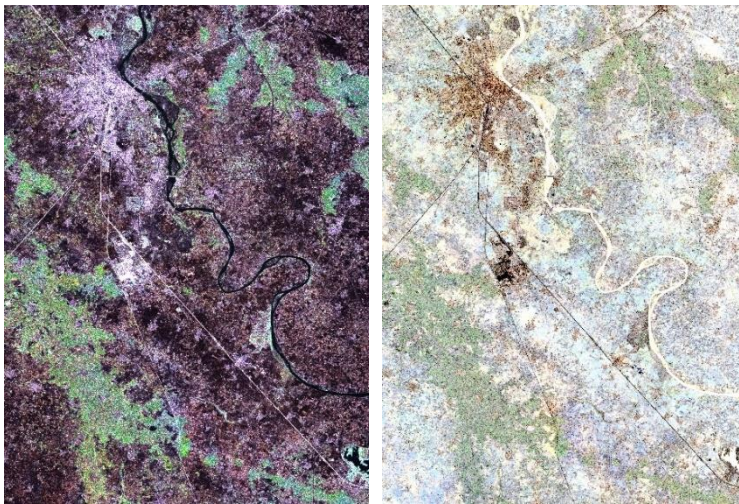
(d) Brovey   (e) GS

Fig. 4.6 SAR-optical fusion of S1A and S2A

Comprehensive assessment (application-based) is introduced, revealing some promising results here. Fig. 4.7 shows the comprehensive assessment of fusion methods using SVM classification, and the outcome of the assessment in terms of kappa coefficient and accuracy is shown in Table 4.8. Surface objects (man-made structures, water, forest, Barren land, and veg. agriculture) have been included in the experiment. The HSV fusion provides maximum accuracy of 83.3521%, and BT gave the worst accuracy. The outcome

Table 4.6 Experimental results of objective measures (reference data required)

Parameter	Fusion method	Fused images			Mean Value	Ideal value
		Green	Red	NIR		
CC	PCA	0.665	0.676	0.710	0.683	1
	GS	0.555	0.555	0.610	0.573	1
	BT	0.056	0.076	0.272	0.134	1
	HSV	0.445	0.445	0.552	0.481	1
UIQI	PCA	-0.045	0.082	0.025	0.021	-1 to 1
	GS	-0.069	-0.055	0.210	0.029	-1 to 1
	BT	-0.049	-0.022	-0.028	-0.033	-1 to 1
	HSV	-0.015	-0.045	0.030	-0.01	-1 to 1
SSIM	PCA	0.570	0.550	0.258	0.459	-1 to 1
	GS	0.462	0.380	0.376	0.406	-1 to 1
	BT	0.250	0.183	0.190	0.208	-1 to 1
	HSV	0.444	0.418	0.276	0.379	-1 to 1
Mean Bias	PCA	0.260	0.220	0.240	0.240	0
	GS	0.000	0.001	0.002	0.001	0
	BT	0.816	0.803	0.595	0.738	0
	HSV	0.304	0.266	0.188	0.249	0

of comprehensive assessment adds some significant contribution, which is not available in subjective and objective evaluation.

4.5.2.4 Computational cost

Computational cost is nowadays a crucial part of analyzing the performance of fusion methods. Here, the processing time of each fusion method is being computed. Even though it is vital to compare in terms of computational costs (processing time, storage), it was difficult as the approaches depended on processing parameters. In this study, the

Table 4.7 Experimental results of objective measures (reference data not required)

Parameter	Band	Initial Value	Fusion method			
			PCA	GS	BT	HSV
	Green	4.520	4.750	5.455	4.002	4.650
Entropy	Red	4.725	4.730	4.995	3.990	4.854
	NIR	5.445	5.556	5.766	4.206	5.485
	Green	124.540	85.224	110.56	17.820	113.35
SD	Red	140.578	85.442	106.34	24.110	142.54
	NIR	154.660	162.57	168.577	72.340	168.54
	Green	9.486	9.210	8.824	4.324	9.256
MI	Red	9.540	9.846	9.276	4.540	9.664
	NIR	10.048	11.324	10.667	6.548	10.424

Table 4.8 Classification outcome evaluation of SAR-optical image fusion method

	Accuracy	Class (percentage)					Overall Accuracy	Kappa Coeff.
		Man-made structure	Barrenland	Water	Forest	Veg. agriculture		
SAR	Prod Acc.	70.21	23.72	65.62	38.55	67.32		
only	User Acc.	73.62	52.33	78.06	79.42	45.73	39.7121	0.2666
Optical	Prod Acc.	93.45	87.19	95.34	74.48	66.52		
only	User Acc.	75.66	81.24	92.89	81.70	72.80	78.1531	0.6835
	Prod Acc.	71.46	99.81	100	46.27	87.46		
PCA	User Acc.	86.90	96.50	96.76	99.74	49.21	82.6276	0.7817
	Prod Acc.	96.66	97.49	65.84	50.48	86.52		
GS	User Acc.	73.73	83.34	90.89	91.70	62.80	79.1190	0.7175
	Prod Acc.	90.63	3.72	5.62	44.35	89.50		
BT	User Acc.	77.82	43.01	53.06	89.56	20.70	39.4871	0.2778
HSV	Prod Acc.	96.67	92.01	100	39.66	89.50		
	User Acc.	81.53	84.76	96.86	77.10	69.04	83.3521	0.7926

same data set and pre-processing steps have been used for all algorithms. In the pixel level approach, the three bands of optical images have been fused with VH polarised SAR image. Table 4.9 shows the processing time for examined fusion methods. So based on computational costs, the BT fusion had the lowest processing time, followed by GS. The results clearly show a trade-off between accuracy and computational cost.

Table 4.9 CPU processing time for fusion methods (Intel i5, 8GB RAM)

	PCA	GS	BT	HSV
Processing Time	30 min 50 sec	29 min 05 sec	02 min 30 sec	30 min 15 sec

The SAR-optical fusion involves moderately high computational complexity due to multi-dimensional data processing and advanced feature extraction. To optimize for real-time or near-real-time applications, following may be undertaken:

- Algorithmic simplification through reduced-rank decomposition and lightweight feature selection helps lower processing loads without a major loss in accuracy.

- Parallel processing using GPUs or parallel computing frameworks can significantly speed up matrix operations and classification tasks.

- Furthermore, edge computing and onboard processing enable the deployment of optimized models directly onto UAVs or mobile platforms, allowing real-time, in-situ data analysis with minimal latency.

- Machine learning optimization techniques, such as employing efficient classifiers like linear SVM or shallow neural networks.

4.5.3 Impact of image fusion on image classification techniques

This research shows the performance of integration of SAR and optical fusion and image classification techniques and exhibits accuracy in term of overall accuracy (OA)

and kappa coefficient. Table 4.10 exhibits the comparison of SVM & ML classifier for different image fusion methods. Table 4.11 compares class accuracies achieved through various combinations of image fusion and classification methods. The analysis of results is presented in a subsequent subsection.
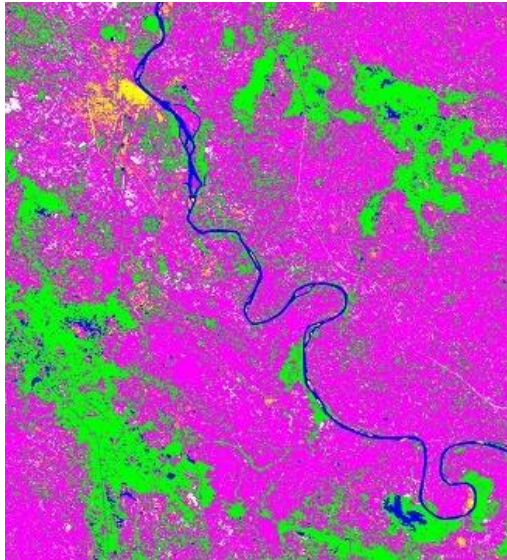
(a) classification of PCA fused
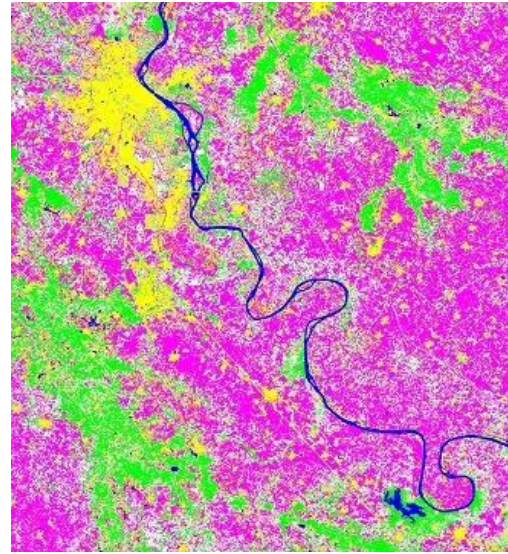
(b) classification of GS fused
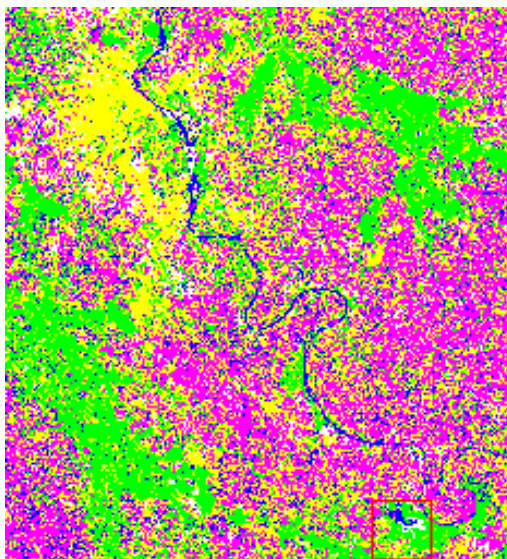
(c) classification of Brovey fused
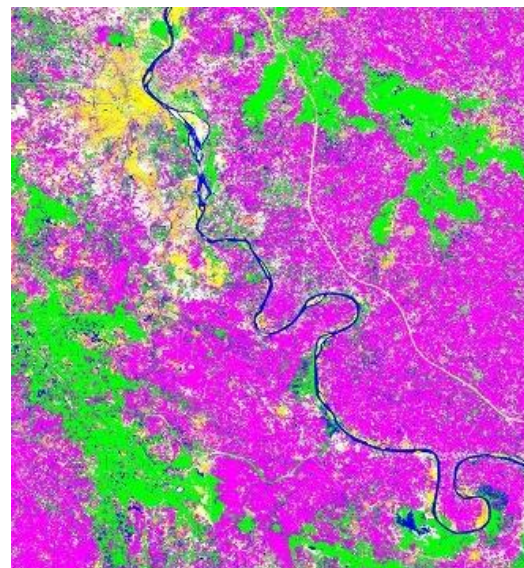
(d) classification of HSV fused

Fig. 4.7 Comprehensive assessment of SAR-optical fusion with SVM classification

Table 4.10 Comparison of SVM & ML classification for different image fusion techniques

Classifier →	SVM		ML	
Fusion ↓	Overall Accuracy	Kappa Coefficient	Overall Accuracy	Kappa Coefficient
SAR only	39.7121	0.2666	35.4141	0.2431
MS only	78.1531	0.6835	77.5431	0.7012
HSV	76.1190	0.6975	74.7641	0.6802
Brovey	39.4871	0.2778	76.4094	0.7021
Gram-Schmidt	84.3521	0.8026	87.5635	0.8431
PCA	82.6276	0.7817	82.5635	0.7711

4.5.3.1 Impact of fusion techniques on maximum-likelihood classification

Fig. 4.8 shows the ML classification outcome of all four fusion techniques (HSV, Brovey, Gram-Schmidt, and PCA). The following observations have been observed from Table 4.10 for ML classifier: Overall classification accuracy of 77.5431% and kappa coefficient of 0.7012 have been obtained from the MS. Overall accuracy of 35.4141% and kappa coefficient of 0.2431 have been achieved from the SAR band. Compared to the SAR image, which lacks spectral information, the MS image has more spectral contents, improving accuracy.

The OA is 76.4094 (kappa coefficient 0.7021) for Brovey Fusion and 74.7641 (kappa coefficient 0.6802) for HSV fusion. A pattern of class intermixing has been observed from Brovey and HSV fusion (Fig. 4.8). BT and HSV methods have been resultant in a reduction in OA by 01.1337% and 02.0341%, respectively. As a result, BT and HSV approaches do not appear to be promising for enhancing classification accuracy. The GS fusion has been the best among all the fusion techniques, as it produced the highest OA of 87.5635% and kappa coefficient of 0.8431, an improvement of

10.0204% in OA and 0.1019 in kappa coefficient, as compared to the MS band only. For PCA technique, the OA is 82.5635 % (kappa coefficient 0.7711), an improvement of about 5.0204% (kappa coefficient 0.0699) in OA over the MS image. Man-made settlement and barrenland have been classified accurately by the PCA technique. All the fusion methods extracted water and forest feature accurately. Thus, GS and PCA fusion methods significantly improve the accuracy of MS images by fusing with SAR images. Confusion between man-made structure, forest, and veg. agriculture have been reduced in the GS-ML combination.

Table 4.11 Comparison of class accuracies for image Fusion and Classification Combinations

Combinations	Man-made structure	Barrenland	Water	Forest	Veg agri
SAR only-SVM	93.66	10.00	15.60	12.15	24.48
SAR only-ML	92.50	25.00	25.60	28.40	90.32
MS only-SVM	80.15	90.15	72.12	48.12	85.15
MS only-ML	80.15	90.68	74.15	42.15	84.12
HSV-SVM	85.65	99.63	63.57	41.59	89.81
HSV-ML	82.48	99.44	62.70	43.27	83.70
Brovey-SVM	90.17	10.05	15.06	46.15	94.20
Brovey-ML	98.49	98.42	60.00	42.31	84.64
GS-SVM	98.04	93.68	100	37.86	92.32
GS-ML	96.68	100	100	52.88	94.52
PCA-SVM	71.45	99.81	100	46.27	87.46
PCA-ML	70.12	98.15	100	44.15	85.15

(a)   PCA with ML   (b)   Gram-Schmidt with ML

(c) Brovey with ML   (d) HSV with ML

Legend: Man-made, Bare-soil, Water, Forest, Agricultural
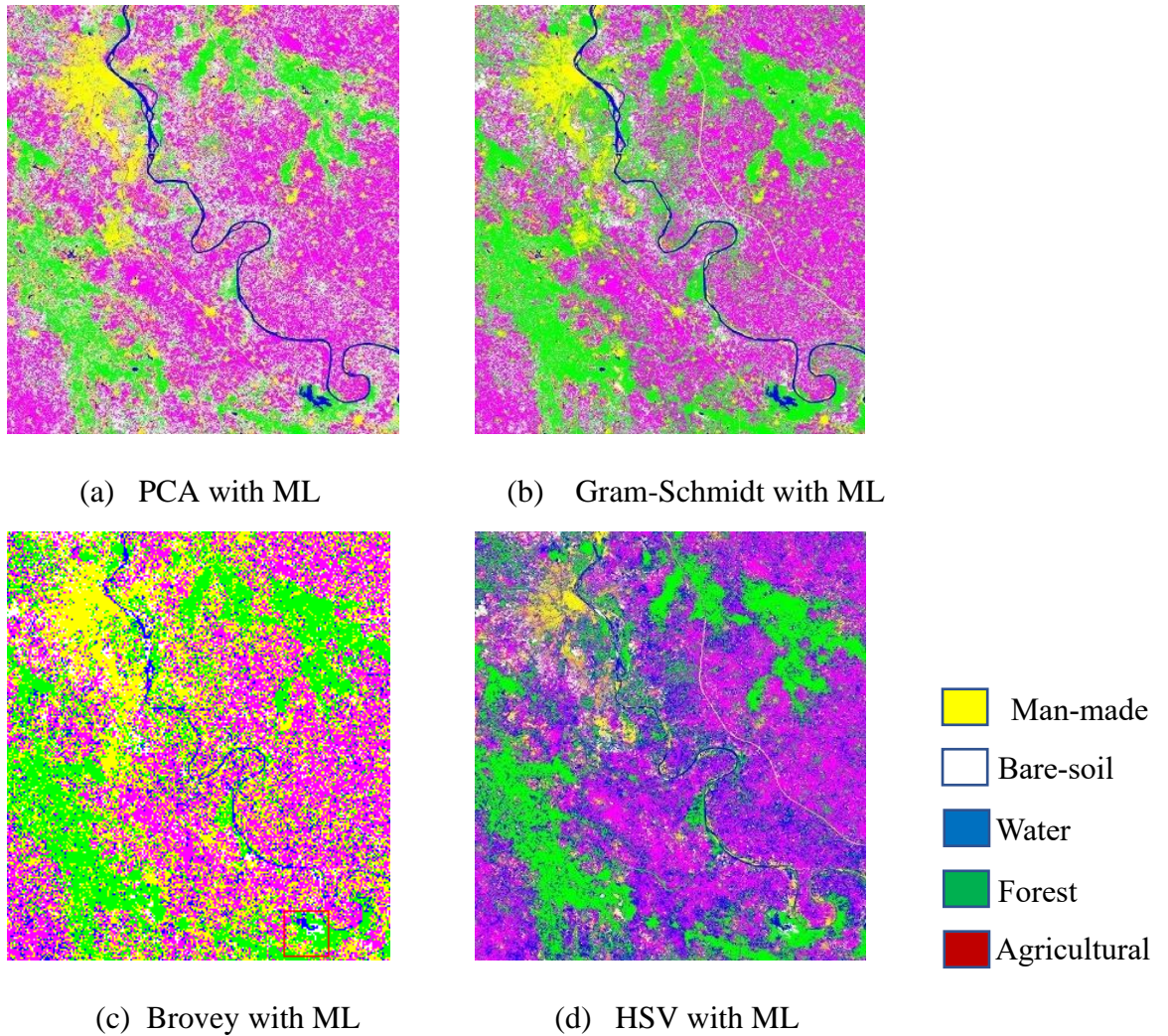
Fig. 4.8 Classified image of combined fusion with classifier (a) PCA with ML (b) Gram-Schmidt with ML, (c) Brovey with ML and (d) HSV with ML

4.5.3.2 Impact of fusion techniques on support vector machines classification

Fig. 4.9 display the influence of four subjected image fusion algorithms on the SVM classification. An overall SVM classifier accuracy of 78.1531% (0.6835 kappa coefficient) for MS image and 39.7121% (0.2666 kappa coefficient) for SAR image has been calculated. The overall accuracy is 39.4871(kappa coefficient 0.2778) for BT Fusion and 76.1190 (kappa coefficient 0.6975) for HSV algorithm. A pattern of class intermixing has been observed from BT and HSV algorithm. These two fusion methods

(BT and HSV) have been resultant in a reduction in OA by 38.6660 % and 02.0341%, respectively. Whereas in the case of the BT fusion algorithm result is worst, and the classes have been intermixed. This poor performance is somehow contributed by speckle interference and the heterogeneous nature of SAR image. GS and PCA fusion enhance the classification accuracy by 06.1990 % and 04.4745%, respectively. GS and PCA fusion preserve the spectral information and embed spatial information into the fused image.

4.5.4 Optimal combination of fusion and classification

In the case of single sensor performance, the outcomes of the SVM classifier outperform the ML classifier for both the SAR and MS image. The SVM classification resulted in higher accuracies for HSV and PCA fusion method than the ML classification, whereas lower for BT and GS fusion techniques. HSV and BT fusion algorithms could not enhance the accuracy assessments (OA and kappa coefficient) of surface objects/ classes compared to single sensor multispectral image. However, the combination of SAR with optical with Gram-Schmidt and PCA improves the feature extraction of surface objects using both classifiers.

In the horizontal comparison of Table 4.10, HSV, the PCA fusion method provides higher accuracy with the SVM classification method than ML. Table 4.10 summarizes all eight combinations of Fusion and classification methods. The GS-ML combination gives the highest overall accuracy, 87.5635, and kappa coefficient 0.8431, whereas the BT-SVM combination provides the worst accuracy. The best result has been achieved with the following combinations: HSV fusion with SVM classifier, Gram-Schmidt fusion with Maximum Likelihood classifier, PCA fusion with SVM classifier, and Brovey Fusion with Maximum Likelihood classifier. The accomplished outcomes demonstrate the supremacy of the GS fusion to PCA, HSV, and Brovey fusion images in

distinguishing and discriminating dense man-made settlements with barren land. Like statistics, visual interpretation of the GS transforms to other fusion outcomes highlight the discrimination of forest with agricultural vegetation. Other studies [159][169] that studied the influence of image fusion on classification techniques (for the fusion of PAN and Multispectral images) also found that GS fusion has been significantly improved the overall accuracy and brovey fusion reduced the accuracy.

(a) PCA with SVM   (b) GS with SVM

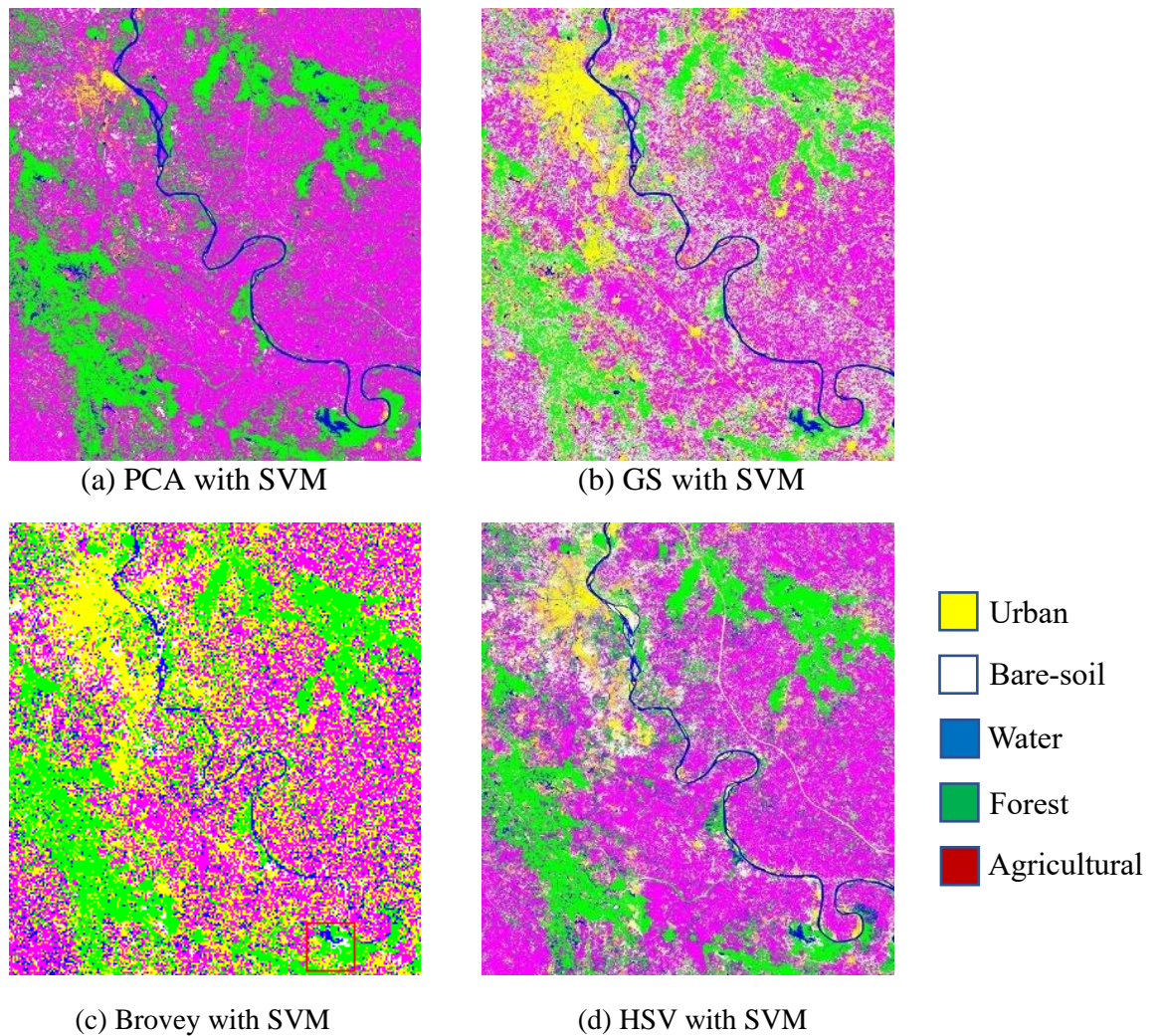(c) Brovey with SVM   (d) HSV with SVM

Fig. 4.9 Classified outcome of Integration of pixel level fusion with SVM classifier (a) PCA with SVM (b) Gram-Schmidt with SVM, (c) Brovey with SVM and (d) HSV with SVM

The achieved results indicate the performance of integration of SAR-optical fusion and image classification techniques. Table 4.10 gives a comparison of SVM and

ML classification methods when different Fusion techniques are used. The achieved results show that mapping can be improved by fusing SAR images with MS images. However, every fusion method doesn't need to improve classification accuracy. The classification accuracy is being affected by the way heterogenous images are fused, incredibly complex SAR images. SAR image is corrupted by Speckle noise, which also affects the accuracy of the resultant. Inaccurate Pixel-to-pixel image registration is also a reason for poor accuracy. These processing errors in SAR data sometimes dominate the composite fused image and resulting in poor accuracy. The intermixing of barren land and man-made objects has been a common error also reported by various studies. It may be observed that SVM performs better than ML in the case of HSV and PCA fusion techniques in addition to SAR only and optical data. However, ML performs better than SVM in two fusion techniques, i.e., BT and Gram-Schmidt. One full image optical component was replaced by SAR image in the case fusion using PCA and HSV. However, in the case of BT, it utilizes the formula given in equation no. 4.9. Hence the fusion is carried out at the level of pixels. In the Gram-Schmidt transform, though PCA-type component substitution is carried out, SAR is done after histogram matches with lower resolution optical bands and orthogonalization.

It appears that both the Brovey and Grams-Schmidt transform lead to a fused image in which the statistical relationship between its pixels is better captured by ML, which is a parametric approach. SVM, which is a non-parametric approach, is not able to retain the original statistical relationship. The SVM support vectors change after fusion, but it is not possible to predict how these would move/change after fusion. Hence, it is difficult to comment whether, after fusion, the performance of SVM will continue to be

better. Similarly, in the case of a different set of data, it is difficult to predict how the changes after fusion manifest in the SVM support vectors.

4.6 Conclusion

This chapter follows the thesis motivation by applying SAR and optical data fusion to improve subsurface and surface object detection and classification in real-world scenarios, including border regions and terrain observation. The availability of open-source SAR and optical data has enhanced the study of multisensory image fusion and its application in the remote sensing domain for several years. Recent research and launch of SAR sensors (specially ESA's Sentinel-1 and Sentinel-2) opens several new trends in SAR-optical fusion in many dimensions. Because SAR and optical images provide complementary details, this kind of fusion is the way forward for a variety of applications, despite the challenges (spatial/spectral distortions, computational complexity and misregistration). The preprocessing of SAR image is one of the key factors that affects the performance of fusion, particularly speckle filtering. The experiment has been conducted to evaluate the speckle effect present in SAR imagery. Speckle filtering of Sentinel-1 C-band has been evaluated with different filters and window sizes. The Lee-sigma and gamma-map filter with window 5x5 size has given the best statistical outcome. Ten de-speckled SAR resultant have been used to fuse with Optical images to find the suitable filter, which preserve the fine feature of SAR data. The fusion image indicates that the lee-sigma filter has handled significantly with inherent speckle filter, so taken for further processing.

This study investigates fusion methods employing PCA, BT, GS, and HSV algorithms. Researchers commonly utilize subjective and objective assessments to evaluate the quality of fusion methods. The visual effect is subjective and may vary

among researchers. Objective assessment requires greater clarity in feature extraction due to the intermixing of some classes. To establish a composite evaluation of SAR optical image fusion, a comprehensive assessment (application-based) is introduced and scrutinized, revealing promising results. The result also established the trade-off between computation-time and accuracy of the fusion techniques.

Another major task of this research focused on the effect of optical and SAR fusion techniques on the image classification approach. Here, image classification accuracy outcomes are taken as evaluation indices of image fusion techniques. The four image fusion approaches (Brovey, HSV, Gram-Schmidt, and PCA) were applied to SAR and optical images. Image fusion outputs have been utilized for two established image classification techniques (SVM, maximum likelihood). Conventional accuracy assessment parameters overall accuracy and Kappa coefficient have been used for classification assessment. The Analysis indicates some pixel-level image fusion methods (GS and PCA) improved the classification accuracy of SAR optical fusion, whereas some fusion techniques (Brovey, HSV) haves poor classification accuracy. Here, eight combinations of fusion and classification techniques have been evaluated, and results indicate that SVM performs better than ML in the case of HSV and PCA methods in addition to SAR only and Multispectral (MS) data. However, ML performs better than SVM in two fusion techniques, i.e., Brovey and Gram-Schmidt. It is concluded that not all fusion techniques improve accuracy, and image fusion techniques influence the accuracy of classification methods.

With the launch of new SAR satellites with higher resolution, SAR and optical fusion remains an active research field that will be useful for a wide range of remote sensing applications. Recent findings indicate that SAR-optical PLF development is moving toward deep learning, big data, and cloud computing. Furthermore, the chapter

highlights the compromise between fusion accuracy and computational time and sheds light on practical matter of sacrificing improved performance against need for real-time processing in mass surveillance applications, such as border surveillance and emergency response.

Chapter- 5

Conclusions, Major Contributions, Limitations and Future Work

In this research, detection of surface and subsurface objects has been explored using Optical data (multispectral), microwave data (real-aperture i.e scatterometer and synthetic aperture radar i.e. SAR) and fusion (SAR and Optical) under three objectives.

- The first objective of the research is to explore improvement in the detection of buried subsurface objects (live antitank mine) by utilising multiband multipolarisation fusion of X- and C-band scatterometer microwave data having VV and HH polarisation.

- The second objective presents the research on improvement of man-made and natural object detection using a fusion of scattering components of C-and L-band Polarimetric SAR data.

- The third objective of this research is to explore improvement in the detection of surface objects using the fusion of optical (Sentinel-2A multispectral image) and microwave (Sentinel-1A SAR) data.

Conclusions arrived after this study have been summarised in the subsequent section followed by research contribution, limitations, and future scope.

5.1 Conclusions

Detection and classification of surface and subsurface (buried) objects using remote sensing data has been a point of research for several years. The capability of all-time, all-weather vision of microwave data makes a natural choice for detecting surface

and subsurface buried objects. The motivation for the research, issues in object detection, and the introduction of microwave remote sensing and image fusion methods have been presented in Chapter 1 of this thesis. Chapter 1 summarises the introduction of the research, the research gaps, objectives, and a critical literature review. In Chapter 1, the image fusion techniques were summarised into five categories. At the end of Chapter 1, the layout of this thesis has been presented. The subsequent three chapters explore the research under the three objectives. Some of the major conclusions drawn concerning each of the objectives are summarised here.

- The research explored the use of microwave remote sensing to detect buried landmines. The landmine detection has been carried out with X- and C-band SCAT data generated through experiments to detect live antitank mines buried under smooth and rough surfaces at different surface roughness depths of 1, 2, 3, 4, and 5 cm. By leveraging VV and HH polarizations and their fusion, a reduction in surface roughness effects, enhancing the accuracy of landmine detection has been observed. Various numerical polarization fusion approaches have been evaluated and polarization discrimination ratio has been found to yield minimum entropy signifying that it results in maximum reduction in surface roughness effects which in turn means that it enhances detection of buried mine. Backscatter and statistical analysis of C- and X- band shows the lower backscatter value of C-band. Also, it appears that C-band data discriminate small backscatter value. The research findings underscore the potential of multiband, multi-polarization fusion techniques for enhancing landmine detection capabilities.

- Multi-band data enhances accuracy for both metallic and non-metallic mines with minimal false alarms.

- In the second research objective, the polarimetry capability of PolSAR data has been utilised to improve the detection of man-made (urban structures) and natural objects (water and forests). The multiband (C-band Radarsat-2 data and L-band ALOS-1 PALSAR) SAR data were decomposed using incoherent and hybrid-based decomposition algorithms. Based on the mean scattering power of three identified man-made and natural object patches, the dominant scattering components were selected. The research proposes a novel approach to the fusion of the dominant volume scattering component of the L-band with the surface and double bounce scattering component of C-band PoLSAR data. The model is evaluated through PCA fusion technique, and it concluded that PCA fusion technique significantly improve the results of detection of man-made and natural objects.

- The third objective i.e. fusion of SAR and optical data has several issues and detection of objects is mostly affected by the presence of speckle noise. Mitigating speckle noise by selecting the appropriate filter and window size is a significant challenge in SAR image processing. The work presented evaluated the speckle filtering of Sentinel-1 C-band data with different filters of 5x5 and 7x7 window sizes. Ten de-speckled results of data of SAR and optical image fusion has been presented. Before fusion, the Lee-sigma and Gamma-map filter with a 7x7 window size gave the best statistical outcomes, whereas, after fusion, the Lee-sigma filter with a 5x5 window size gave better results. Fusion techniques can affect the outcome of speckle filtering. The fusion image indicated that the Lee-sigma filter handled the inherent speckle noise well after the fusion.

- This objective examines fusion techniques based on PCA, BT, GS and CN spectral sharpening (CN) PLF. Fusion techniques based on CS are less computationally demanding and more accessible to implement. Numerical-based methods are less complex but offer severe spectral and spatial distortion. MRA methods reduce spatial and spectral distortion. Model-based methods have greater computational complexity but outperform them in terms of performance. Hybrid techniques combine the benefits of CS and MRA methodologies, resulting in a superior fused outcome than separate methods.

- In this research, a comprehensive assessment of image fusion techniques were presented and evaluated with established objective and subjective evaluation. The application-based comprehensive assessment provided a significant result. To show the assessment, SVM was used for the experimental outcomes of PCA, HSV, GS and BT fused images for land-cover classification of the man-made objects (settlement) and natural (agri. Vegetation, water body, and forest) class.

- This research also focuses on the effect of optical and SAR fusion techniques on the image classification approach. In this research, image classification accuracy outcomes serve as evaluation indices for image fusion techniques. The four image fusion approaches (Brovey, HSV, Gram-Schmidt, and PCA) were applied to SAR and optical images. Image fusion outputs have been utilized for two popular image classification techniques (SVM, Maximum Likelihood). The analysis indicate that some pixel-level image fusion methods (GS and PCA) improved the classification accuracy of SAR optical fusion. In contrast, some fusion techniques (Brovey, HSV) have poor classification accuracy.

- In the research, eight combinations of fusion and classification techniques were evaluated, and result indicated that SVM performs better than ML in the case of HSV and PCA methods in addition to SAR only and Multispectral (MS) data. However, ML performs better than SVM in two fusion techniques, i.e., Brovey and Gram-Schmidt. It appears that not all fusion techniques improve accuracy, and image fusion techniques influence the accuracy of classification methods.

- Computational cost (Table 4.9) is nowadays a crucial part of analysing the performance of fusion methods. Here, the processing time of each fusion method has been computed. Even though it is vital to compare in terms of computational costs (processing time, storage), it is difficult as the approaches depended on processing parameters. Based on computational costs, the BT fusion appears to have lowest processing time, followed by GS. The results show a trade-off between accuracy and computational cost.

- SAR-optical fusion improves surface feature detection under varying environmental conditions, supporting disaster response and environmental monitoring.

These methods are scalable, adaptable, and suitable for integration into defence, disaster management, and environmental monitoring systems.

5.2 Research contributions

Based on the preceding conclusions, the major contributions of this research are summarised below-

- In this research, an alternative model using multiband, multipolarisation microwave data has been uexplored for buried landmine detection. This model leads to the minimization of surface roughness effects and highlighting various

mine-like features in an image without getting too intricately involved in the complexities of modelling the EM scattering phenomena and layered media effect.

- In this research, the effect of speckle filters and their window sizes has been analysed on pixel-level SAR-optical image fusion data. The result brings out a new approach for speckle filter evaluation and impact on SAR data processing.

- The results of third objective establishes that optimal combinations of the SAR- and optical image data improves surface object detection.

- This work evaluates the performance of SAR and optical fusion through objective, subjective, and comprehensive parameters. Evaluating SAR and optical image fusion on a comprehensive (application based) scale is a contribution of the paper.

5.3 Limitations

Some of the limitations of this research which may have a bearing on the results are summarised below-

- The landmine detection experiments have been restricted to dry sand only, which may be extended to soil with varying moisture conditions.

- Microwave scatterometers and PolSAR systems may have limited penetration depth in wet or highly conductive soils, reducing detection reliability for deeply buried objects.

- Landmine detection experiments have been considered for like-polarisation (VV and HH) data, which should be extended for cross-polarisation (VH and HV) data as cross-polarisation data are sensitive to volume scattering.

- Non-availability of Temporal C- and L- band data of same dates restricts its the in detection of man-made and natural objects.

- The seasonal sensitivity of natural objects such as water and forests and man-made objects such as buildings could not explored in this work. The objects selected have been those which had minimal seasonal effects.

- Detection performance can be affected by soil moisture variations, vegetation cover, and surface roughness, particularly in real-world landmine detection using microwave data.

- Optical data fusion is affected by cloud cover and lighting conditions, which may reduce availability and consistency.

- Some fusion and classification methods require significant processing power, posing challenges for real-time or onboard implementation without hardware optimization.

5.4 Future scope

To build upon the results of this research. Following aspects may be considered for future research:

- With the recent advancement of the UAV and drone technology, further research may be carried out to develop a model for landmine detection techniques irrespective of soil conditioning using drones.

- The development of real-time or near-real-time landmine detection systems for deployment in critical areas like conflict zones or post-conflict regions is a significant challenge. Future research can focus on creating portable and autonomous systems that can operate in dynamic environments.

- Large-scale landmine detection can be achieved by deploying multi-polarization microwave techniques using UAVs or mobile platforms across vast desert or border areas.

- Future research can explore more sophisticated data fusion techniques that incorporate additional polarimetric channels and frequency bands. This could enhance the discrimination between landmines and clutter even further.

- Combining microwave data with data from other sensor modalities, such as thermal imaging or ground-penetrating radar, can provide a comprehensive approach to landmine detection. Multi-sensor fusion can potentially reduce false alarms and improve detection rates.

- The multiband SAR image fusion gets momentum with the availability of multiband Spaceborne SAR sensors on a single platform, in view of upcoming open-source NISAR project.

REFERENCE

[1] Aggarwal, Shefali. "Principles of remote sensing." *Satellite remote sensing and GIS applications in agricultural meteorology* 23.2 (2004): 23-28.

[2] Mohd Noor, Norzailawati, Alias Abdullah, and Mazlan Hashim. "Remote sensing UAV/drones and its applications for urban areas: A review." *IOP conference series: Earth and environmental science*. Vol. 169. IOP Publishing, 2018.

[3] Jellouli, Amine, et al. "Application of optical and radar satellite images for mapping tectonic lineaments in kerdous inlier of the Anti-Atlas belt, Morocco." *Remote Sensing Applications: Society and Environment* 22 (2021): 100509.

[4] Hussein, Esam MA, and Edward J. Waller. "Landmine detection: the problem and the challenge." *Applied Radiation and Isotopes* 53.4-5 (2000): 557-563.

[5] Rahman, M. Mahmudur, Josaphat Tetuko Sri Sumantyo, and M. Fouad Sadek. "Microwave and optical image fusion for surface and sub-surface feature mapping in Eastern Sahara." *International Journal of Remote Sensing* 31.20 (2010): 5465-5480.

[6] Lillesand, Thomas, Ralph W. Kiefer, and Jonathan Chipman. *Remote sensing and image interpretation*. John Wiley & Sons, 2015.

[7] Elachi, Charles, and Jakob J. Van Zyl. *Introduction to the physics and techniques of remote sensing*. John Wiley & Sons, 2021.

[8] Gao, Gui, et al. "Adaptive ship detection in hybrid-polarimetric SAR images based on the power–entropy decomposition." *IEEE Transactions on Geoscience and Remote Sensing* 56.9 (2018): 5394-5407.

[9] Pohl, Cle, and John L. Van Genderen. "Multisensor image fusion in remote sensing: concepts, methods and applications." *International journal of remote sensing* 19.5 (1998): 823-854.

[10] Simone, Giovanni, et al. "Image fusion techniques for remote sensing applications." *Information fusion* 3.1 (2002): 3-15.

[11] Bhadouria, Vikesh S., et al. "Automated microwave monitoring of hidden objects for strategic and security applications." *Journal of Electromagnetic Waves and Applications* 35.18 (2021): 2492-2509.

[12] Upender, Patri, and Anil Kumar. "Design and Development of a Scatterometer to Detect Shallowly Buried Objects Using Microwaves at X-Band Frequency." *Journal of Green Engineering* 10 (2020): 12988-13004.

[13] Chen, Shengbo, Juliana Useya, and Hillary Mugiyo. "Decision-level fusion of Sentinel-1 SAR and Landsat 8 OLI texture features for crop discrimination and classification: case of Masvingo, Zimbabwe." *Heliyon* 6.11 (2020).

[14] Bestagini, Paolo, et al. "Landmine detection using autoencoders on multipolarization GPR volumetric data." *IEEE Transactions on Geoscience and Remote Sensing* 59.1 (2020): 182-195.

[15] Pochanin, Gennadiy, et al. "Radar Systems for Landmine Detection." *2020 IEEE Ukrainian Microwave Week (UkrMW)*. IEEE, 2020.

[16] Peichl, Markus, et al. "Novel imaging radar technology for detection of landmines and other unexploded ordnance." *European Journal for Security Research* 2.1 (2017): 23-37.

[17] Tiwari, Kailash Chandra, Dharmendra Singh, and Manoj Arora. "Development of a model for detection and estimation of depth of shallow buried non-metallic landmine at microwave X-band frequency." *Progress In Electromagnetics Research* 79 (2008): 225-250.

[18] Ulaby, F. T., et al. "Microwave Radar and Radiometric Remote Sensing, University of Michigan Press." *Ann Arbor* (2014).

[19] Dill, Stephan, et al. "A drone carried multichannel Synthetic Aperture Radar for advanced buried object detection." *2019 IEEE Radar Conference (RadarConf)*. IEEE, 2019.

[20] Quang, Nguyen Hong, et al. "Synthetic aperture radar and optical remote sensing image fusion for flood monitoring in the Vietnam lower Mekong basin: A prototype application for the Vietnam Open Data Cube." *European Journal of Remote Sensing* 52.1 (2019): 599-612.

[21] Amarsaikhan, D., et al. "Fusing high-resolution SAR and optical imagery for improved urban land cover study and classification." *International Journal of Image and Data Fusion* 1.1 (2010): 83-97.

[22] Kerman, Bryan. "Fusion of Dual-Frequency SAR Imagery of Sea Ice." *Atmosphere--Ocean (Canadian Meteorological & Oceanographic Society)* 37.4 (1999).

[23] Joshi, Neha, et al. "A review of the application of optical and radar remote sensing data fusion to land use mapping and monitoring." *Remote Sensing* 8.1 (2016): 70.

[24] Zhang, Hongsheng, and Ru Xu. "Exploring the optimal integration levels between SAR and optical data for better urban land cover mapping in the Pearl River Delta." *International journal of applied earth observation and geoinformation* 64 (2018): 87-95.

[25] Zhang, Shijun, et al. "Small target detection of infrared image based on energy features." *International Conference on Neural Networks and Signal Processing, 2003. Proceedings of the 2003*. Vol. 1. IEEE, 2003.

[26] Chen, Siyue, and Henry Leung. "Chaotic spread spectrum watermarking for remote sensing images." *Journal of Electronic Imaging* 13.1 (2004): 220-230.

[27] Blaschke, Thomas, Stefan Lang, and Geoffrey Hay, eds. *Object-based image analysis: spatial concepts for knowledge-driven remote sensing applications*. Springer Science & Business Media, 2008.

[28] Cheng, Gong, and Junwei Han. "A survey on object detection in optical remote sensing images." *ISPRS journal of photogrammetry and remote sensing* 117 (2016): 11-28.

[29] Roelfsema, Chris, et al. "Challenges of remote sensing for quantifying changes in large complex seagrass environments." *Estuarine, Coastal and Shelf Science* 133 (2013): 161-171.

[30] Miller, Timothy W., J. M. H. Hendrickx, and B. Borchers. "Radar detection of buried landmines in field soils." *Vadose Zone Journal* 3.4 (2004): 1116-1127.

[31] Kumar, Ajay, et al. "Landmines detection using migration and selection algorithm on ground penetrating radar images." *2020 International Conference on Convergence to Digital World-Quo Vadis (ICCDW)*. IEEE, 2020.

[32] Comite, Davide, et al. "Forward-looking ground-penetrating radar: Subsurface target imaging and detection: A review." *IEEE Geoscience and Remote Sensing Magazine* 9.4 (2021): 173-190.

[33] Potin, Delphine, et al. "An abrupt change detection algorithm for buried landmines localization." *IEEE Transactions on Geoscience and Remote Sensing* 44.2 (2006): 260-272.

[34] Masunaga, Seiji, and Kenzo Nonami. "Controlled metal detector mounted on mine detection robot." *International Journal of Advanced Robotic Systems* 4.2 (2007): 26.

[35] Caorsi, Salvatore, and Gaia Cevini. "An electromagnetic approach based on neural networks for the GPR investigation of buried cylinders." *IEEE Geoscience and Remote Sensing Letters* 2.1 (2005): 3-7.

[36] Amiri, Amin, Kenneth Tong, and Kevin Chetty. "Feasibility study of multi-frequency Ground Penetrating Radar for rotary UAV platforms." (2012): 92-92.

[37] Song, Yicheng, and Akira Hirose. "Proposal of a ground penetrating radar system utilizing polarization information by using phasor-quaternion self-organizing map." *2021 IEEE International Geoscience and Remote Sensing Symposium IGARSS*. IEEE, 2021.

[38] Habib, Maki K. "Controlled biological and biomimetic systems for landmine detection." *Biosensors and Bioelectronics* 23.1 (2007): 1-18.

[39] Poling, Alan, et al. "Using giant African pouched rats (Cricetomys gambianus) to detect landmines." *The Psychological Record* 60.4 (2010): 715-728.

[40] Yagur-Kroll, Sharon, et al. "Escherichia coli bioreporters for the detection of 2, 4-dinitrotoluene and 2, 4, 6-trinitrotoluene." *Applied Microbiology and Biotechnology* 98 (2014): 885-895.

[41] Kasban, Hany, et al. "A comparative study of landmine detection techniques." *Sensing and Imaging: An International Journal* 11 (2010): 89-112.

[42] Cardona, Lorena, Jovani Jiménez, and Nelson Vanegas. "Landmine detection technologies to face the demining problem in Antioquia." *Dyna* 81.183 (2014): 115-125.

[43] Suganthi, G., and K. Reeba. "Discrimination of mine-like objects in infrared images using artificial neural network." *Indian J. Appl. Res* 4.12 (2014): 206-208.

[44] Kaneko, Alex M., Edwardo Fukushima, and Gen Endo. "A discrimination method for landmines and metal fragments using metal detectors." *J Conv Weapons Destr* 18.1 (2014): 16.

[45] Bruschini, Claudio, et al. "Ground penetrating radar and imaging metal detector for antipersonnel mine detection." *Journal of Applied Geophysics* 40.1-3 (1998): 59-71.

[46] Chan, Yee Kit, and Voon Koo. "An introduction to synthetic aperture radar (SAR)." *Progress In Electromagnetics Research B* 2 (2008): 27-60.

[47] Moreira, Alberto, et al. "A tutorial on synthetic aperture radar." *IEEE Geoscience and remote sensing magazine* 1.1 (2013): 6-43.

[48] Lee, Jong-Sen, and Eric Pottier. *Polarimetric radar imaging: from basics to applications*. CRC press, 2017.

[49] Maleki, Saeideh, et al. "Analysis of multi-frequency and multi-polarization SAR data for wetland mapping in Hamoun-e-Hirmand wetland." *International Journal of Remote Sensing* 41.6 (2020): 2277-2302.

[50] Guida, Raffaella, Su Wai Ng, and Pasquale Iervolino. "S-and X-band SAR data fusion." *2015 IEEE 5th Asia-Pacific Conference on Synthetic Aperture Radar (APSAR)*. IEEE, 2015.

[51] Amarsaikhan, D., et al. "Applications of GIS and very high-resolution RS data for urban land use change studies in mongolia." *International Journal of Navigation and Observation* 2011 (2011).

[52] Alparone, Luciano, et al. "Landsat ETM+ and SAR image fusion based on generalized intensity modulation." *IEEE Transactions on geoscience and remote sensing* 42.12 (2004): 2832-2839.

[53] Herold, Nathaniel D., and Barry N. Haack. "Fusion of radar and optical data for land cover mapping." *Geocarto International* 17.2 (2002): 21-30.

[54] Pal, S. K., T. J. Majumdar, and Amit K. Bhattacharya. "ERS-2 SAR and IRS-1C LISS III data fusion: A PCA approach to improve remote sensing based geological interpretation." *ISPRS journal of photogrammetry and remote sensing* 61.5 (2007): 281-297.

[55] Abdikan, Saygin, and Fusun Balik Sanli. "Comparison of different fusion algorithms in urban and agricultural areas using SAR (PALSAR and RADARSAT) and optical (SPOT) images." *Boletim de Ciências Geodésicas* 18 (2012): 509-531.

[56] Abd Manaf, Syaifulnizam, et al. "Comparison of Classification Techniques on Fused Optical and SAR Images for Shoreline Extraction: A Case Study at Northeast Coast of Peninsular Malaysia." *J. Comput. Sci.* 12.8 (2016): 399-411.

[57] Kumar, Mohit, et al. "Study of mangrove communities in Marine National Park and Sanctuary, Jamnagar, Gujarat, India, by fusing RISAT-1 SAR and Resourcesat-2 LISS-IV images." *International Journal of Image and Data Fusion* 8.1 (2017): 73-91.

[58] Harris, Jeff R., Richard Murray, and Tom Hirose. "IHS transform for the integration of radar imagery with other remotely sensed data." *Photogrammetric Engineering and Remote Sensing* 56.12 (1990): 1631-1641.

[59] Liu, Jun, et al. "Human visual system consistent quality assessment for remote sensing image fusion." *ISPRS Journal of Photogrammetry and Remote Sensing* 105 (2015): 79-90.

[60] Shao, Zhenfeng, Wenfu Wu, and Songjing Guo. "IHS-GTF: A fusion method for optical and synthetic aperture radar data." *Remote Sensing* 12.17 (2020): 2796.

[61] Ehlers, Manfred, et al. "Multi-sensor image fusion for pansharpening in remote sensing." *International Journal of Image and Data Fusion* 1.1 (2010): 25-45.

[62] Abdikan, Saygin, et al. "Enhancing land use classification with fusing dual-polarized TerraSAR-X and multispectral RapidEye data." *Journal of Applied Remote Sensing* 9.1 (2015): 096054-096054.

[63] Gibril, Mohamed Barakat A., et al. "Fusion of RADARSAT-2 and multispectral optical remote sensing data for LULC extraction in a tropical agricultural area." *Geocarto international* 32.7 (2017): 735-748.

[64] Alparone, Luciano, et al. "Fusion of multispectral and SAR images by intensity modulation." *Proceedings of the 7th International Conference on Information Fusion.* Vol. 2. 2004.

[65] Chandrakanth, R., et al. "A novel image fusion system for multisensor and multiband remote sensing data." *IETE Journal of Research* 60.2 (2014): 168-182.

[66] Hong, Gang, Yun Zhang, and Bryan Mercer. "A wavelet and IHS integration method to fuse high resolution SAR with moderate resolution multispectral images." *Photogrammetric Engineering & Remote Sensing* 75.10 (2009): 1213-1223.

[67] Shah, Esha, P. Jayaprasad, and M. E. James. "Image fusion of SAR and optical images for identifying Antarctic ice features." *Journal of the Indian Society of Remote Sensing* 47 (2019): 2113-2127.

[68] Yaning, Lu, et al. "SAR and MS image fusion based on curvelet transform and activity measure." *2011 International Conference on Electric Information and Control Engineering.* IEEE, 2011.

[69] El-Tawel, Gh S., and A. K. Helmy. "Fusion of multispectral and full polarimetric SAR images in NSST domain." *Int. J. Image Process* 8.6 (2014): 497.

[70] Zhang, Jixian. "Multi-source remote sensing data fusion: status and trends." *International Journal of Image and Data Fusion* 1.1 (2010): 5-24.

[71] Shakya, Achala, Mantosh Biswas, and Mahesh Pal. "CNN-based fusion and classification of SAR and Optical data." *International Journal of Remote Sensing* 41.22 (2020): 8839-8861.

[72] Grohnfeldt, Claas, Michael Schmitt, and Xiaoxiang Zhu. "A conditional generative adversarial network to fuse SAR and multispectral optical data for cloud removal from Sentinel-2 images." *IGARSS 2018-2018 IEEE International Geoscience and Remote Sensing Symposium*. IEEE, 2018.

[73] Bermudez, Jose D., et al. "Synthesis of multispectral optical images from SAR/optical multitemporal data using conditional generative adversarial networks." *IEEE Geoscience and Remote Sensing Letters* 16.8 (2019): 1220-1224.

[74] Wang, X. L., and C. X. Chen. "Image fusion for synthetic aperture radar and multispectral images based on sub-band-modulated non-subsampled contourlet transform and pulse coupled neural network methods." *The Imaging Science Journal* 64.2 (2016): 87-93.

[75] Huang, Yuqin, et al. "The fusion of multispectral and SAR images based wavelet transformation over urban area." *Proceedings. 2005 IEEE International Geoscience and Remote Sensing Symposium, 2005. IGARSS'05.*. Vol. 6. Ieee, 2005.

[76] Han, Nianlong, Jinxing Hu, and Wei Zhang. "Multi-spectral and SAR images fusion via Mallat and À trous wavelet transform." *2010 18th International Conference on Geoinformatics*. IEEE, 2010.

[77] Kulkarni, Samadhan C., and Priti P. Rege. "Application of Taguchi method to improve land use land cover classification using PCA-DWT-based SAR-multispectral image fusion." *Journal of Applied Remote Sensing* 15.1 (2021): 014509-014509.

[78] Chibani, Youcef. "Additive integration of SAR features into multispectral SPOT images by means of the à trous wavelet decomposition." *ISPRS journal of photogrammetry and remote sensing* 60.5 (2006): 306-314.

[79] Chen, Shaohui, et al. "SAR and multispectral image fusion using generalized IHS transform based on à trous wavelet and EMD decompositions." *IEEE Sensors Journal* 10.3 (2010): 737-745.

[80] Quan, Yinghui, et al. "A novel image fusion method of multi-spectral and SAR images for land cover classification." *Remote Sensing* 12.22 (2020): 3801.

[81] Chen, Chao, et al. "A pixel-level fusion method for multi-source optical remote sensing image combining the principal component analysis and curvelet transform." *Earth Science Informatics* 13 (2020): 1005-1013.

[82] Tu, Te-Ming, et al. "A fast intensity-hue-saturation fusion technique with spectral adjustment for IKONOS imagery." *IEEE Geoscience and Remote sensing letters* 1.4 (2004): 309-312.

[83] Dahiya, Susheela, Pradeep Kumar Garg, and Mahesh K. Jat. "A comparative study of various pixel-based image fusion techniques as applied to an urban environment." *International Journal of Image and Data Fusion* 4.3 (2013): 197-213.

[84] Klonus, Sascha, and Manfred Ehlers. "Image fusion using the Ehlers spectral characteristics preservation algorithm." *GIScience & Remote Sensing* 44.2 (2007): 93-116.

[85] Taha, Lamyaa Gamal El-deen, and Salwa Farouk Elbeih. "Investigation of fusion of SAR and Landsat data for shoreline super resolution mapping: the northeastern Mediterranean Sea coast in Egypt." *Applied Geomatics* 2 (2010): 177-186.

[86] Ghassemian, Hassan. "A review of remote sensing image fusion methods." *Information Fusion* 32 (2016): 75-89.

[87] Wang, Zhijun, et al. "A comparative analysis of image fusion methods." *IEEE transactions on geoscience and remote sensing* 43.6 (2005): 1391-1402.

[88] Misra, Indranil, et al. "An efficient algorithm for automatic fusion of RISAT-1 SAR data and Resourcesat-2 optical images." *2012 4th International Conference on Intelligent Human Computer Interaction (IHCI)*. IEEE, 2012.

[89] Ranchin, Thierry, and Lucien Wald. "Fusion of high spatial and spectral resolution images: The ARSIS concept and its implementation." *Photogrammetric engineering and remote sensing* 66.1 (2000): 49-61.

[90] Han, Nianlong, Jinxing Hu, and Wei Zhang. "Multi-spectral and SAR images fusion via Mallat and À trous wavelet transform." *2010 18th International Conference on Geoinformatics*. IEEE, 2010.

[91] Luo, Dan, et al. "Fusion of high spatial resolution optical and polarimetric SAR images for urban land cover classification." *2014 Third International Workshop on Earth Observation and Remote Sensing Applications (EORSA)*. IEEE, 2014.

[92] Zhang, Rui, et al. "A novel feature-level fusion framework using optical and SAR remote sensing images for land use/land cover (LULC) classification in cloudy mountainous area." *Applied Sciences* 10.8 (2020): 2928.

[93] Zhang, Wei, and Le Yu. "SAR and Landsat ETM+ image fusion using variational model." *2010 International Conference on Computer and Communication Technologies in Agriculture Engineering*. Vol. 3. IEEE, 2010.

[94] Liu, Chunhui, Yue Qi, and Wenrui Ding. "Airborne SAR and optical image fusion based on IHS transform and joint non-negative sparse representation." *2016 IEEE International Geoscience and Remote Sensing Symposium (IGARSS)*. IEEE, 2016.

[95] Ghahremani, Morteza, and Hassan Ghassemian. "A compressed-sensing-based pan-sharpening method for spectral distortion reduction." *IEEE Transactions on Geoscience and remote Sensing* 54.4 (2015): 2194-2206.

[96] Liu, Meijie, et al. "PCA-based sea-ice image fusion of optical data by HIS transform and SAR data by wavelet transform." *Acta Oceanologica Sinica* 34 (2015): 59-67.

[97] Jagalingam, P., and Arkal Vittal Hegde. "A review of quality metrics for fused image." *Aquatic Procedia* 4 (2015): 133-142.

[98] Kulkarni, Samadhan C., and Priti P. Rege. "Pixel level fusion techniques for SAR and optical images: A review." *Information Fusion* 59 (2020): 13-29.

[99] Byun, Younggi, Jaewan Choi, and Youkyung Han. "An area-based image fusion scheme for the integration of SAR and optical satellite imagery." *IEEE journal of selected topics in applied earth observations and remote sensing* 6.5 (2013): 2212-2220.

[100] El-Mezouar, Miloud Chikr, et al. "An IHS-based fusion for color distortion reduction and vegetation enhancement in IKONOS imagery." *IEEE Transactions on Geoscience and Remote Sensing* 49.5 (2010): 1590-1602.

[101] Kulkarni, Samadhan C., and Priti P. Rege. "Fusion of Risat-1 SAR image and Resourcesat-2 multispectral images using wavelet transform." *2019 6th International Conference on Signal Processing and Integrated Networks (SPIN)*. IEEE, 2019.

[102] Wald, Lucien, Thierry Ranchin, and Marc Mangolini. "Fusion of satellite images of different spatial resolutions: Assessing the quality of resulting images." *Photogrammetric engineering and remote sensing* 63.6 (1997): 691-699.

[103] Li, Shanshan, Richang Hong, and Xiuqing Wu. "A novel similarity based quality metric for image fusion." *2008 International Conference on Audio, Language and Image Processing*. IEEE, 2008.

[104] You, Chunyan, et al. "An Objective Quality Metric for Image Fusion based on Mutual Information and Muti-scale Structural Similarity." *J. Softw.* 9.4 (2014): 1050-1054.

[105] Zheng, Yufeng, et al. "A new metric based on extended spatial frequency and its application to DWT based fusion algorithms." *Information Fusion* 8.2 (2007): 177-192.

[106] Neetu, and Shibendu Shankar Ray. "Evaluation of different approaches to the fusion of Sentinel-1 SAR data and Resourcesat 2 LISS III optical data for use in crop classification." *Remote Sensing Letters* 11.12 (2020): 1157-1166.

[107] Ali, Muhammad Zeeshan, Waqas Qazi, and Nasir Aslam. "A comparative study of ALOS-2 PALSAR and landsat-8 imagery for land cover classification using maximum likelihood classifier." *The Egyptian Journal of Remote Sensing and Space Science* 21 (2018): S29-S35.

[108] Clerici, Nicola, Cesar Augusto Valbuena Calderón, and Juan Manuel Posada. "Fusion of Sentinel-1A and Sentinel-2A data for land cover mapping: a case study in the lower Magdalena region, Colombia." *Journal of Maps* 13.2 (2017): 718-726.

[109] Gibril, Mohamed Barakat A., et al. "Fusion of RADARSAT-2 and multispectral optical remote sensing data for LULC extraction in a tropical agricultural area." *Geocarto international* 32.7 (2017): 735-748.

[110] Manakos, Ioannis, Georgios A. Kordelas, and Kalliroi Marini. "Fusion of Sentinel-1 data with Sentinel-2 products to overcome non-favourable atmospheric conditions for the delineation of inundation maps." *European Journal of Remote Sensing* 53.sup2 (2020): 53-66.

[111] Veerabhadraswamy, Naveen, Guddappa M. Devagiri, and Anil Kumar Khaple. "Fusion of complementary information of SAR and optical data for forest cover mapping using random forest algorithm." *Curr. Sci* 120 (2021): 193-199.

[112] Riedel, T., C. Thiel, and C. Schmullius. "Fusion of optical and SAR satellite data for improved land cover mapping in agricultural areas." *Proc. Envisat Symposium*. 2007.

[113] Meraner, Andrea, et al. "Cloud removal in Sentinel-2 imagery using a deep residual neural network and SAR-optical data fusion." *ISPRS Journal of Photogrammetry and Remote Sensing* 166 (2020): 333-346.

[114] Li, Xiujuan, et al. "A hybrid polarimetric target decomposition algorithm with adaptive volume scattering model." *Remote Sensing* 14.10 (2022): 2441.

[115] Daniels, Julian, et al. "Microwave remote sensing of physically buried objects in the Negev Desert: implications for environmental research." *Remote sensing of environment* 86.2 (2003): 243-256.

[116] Singh, Dharmendra, et al. "Shape recognition of shallow buries metallic objects at X-band using ANN and image analysis techniques." (2009).

[117] Schofield, John, David Daniels, and Paul Hammerton. "A multiple migration and stacking algorithm designed for land mine detection." *IEEE Transactions on Geoscience and Remote Sensing* 52.11 (2014): 6983-6988.

[118] Tabatabaeenejad, Alireza, and Mahta Moghaddam. "Bistatic scattering from three-dimensional layered rough surfaces." *IEEE Transactions on Geoscience and Remote Sensing* 44.8 (2006): 2102-2114.

[119] Takahashi, Kazunori, et al. "Influence of heterogeneous soils and clutter on the performance of ground-penetrating radar for landmine detection." *IEEE transactions on geoscience and remote sensing* 52.6 (2013): 3464-3472.

[120] Maathuis, Ben HP, and JL van Genderen. "A review of satellite and airborne sensors for remote sensing based detection of minefields and landmines." *International journal of remote sensing* 25.23 (2004): 5201-5245.

[121] Gebremichael, T., Dilip Mali, and Abdelhak M. Zoubir. "Clutter reduction techniques for GPR based buried landmine detection." *2011 International Conference on Signal Processing, Communication, Computing and Networking Technologies*. IEEE, 2011.

[122] Cmielewski, Octavien, et al. "Surface roughness estimation towards a buried target characterization." *2007 IEEE International Geoscience and Remote Sensing Symposium*. IEEE, 2007.

[123] Latini, Daniele, Fabio Del Frate, and Cathleen E. Jones. "Multi-frequency and polarimetric quantitative analysis of the Gulf of Mexico oil spill event comparing different SAR systems." *Remote Sensing of Environment* 183 (2016): 26-42.

[124] El-Shenawee, Magda. "Polarimetric scattering from two-layered two-dimensional random rough surfaces with and without buried objects." *IEEE transactions on geoscience and remote sensing* 42.1 (2004): 67-76.

[125] Chen, Jiong, Yilun Chen, and Jian Yang. "Ship detection using polarization cross-entropy." *IEEE Geoscience and Remote Sensing Letters* 6.4 (2009): 723-727.

[126] Singh, Dharmendra. "Polarization discrimination ratio approach to retrieve bare soil moisture at X-band." *Proceedings. 2005 IEEE International Geoscience and Remote Sensing Symposium, 2005. IGARSS'05*. Vol. 1. IEEE, 2005.

[127] Voronovich, Alexander G., and Valery U. Zavorotny. "Full-polarization modeling of monostatic and bistatic radar scattering from a rough sea surface." *IEEE Transactions on Antennas and Propagation* 62.3 (2013): 1362-1371.

[128] Smith, Paul D., et al. "An introduction to polarisation effects in wave scattering and their applications in target classification." *Ultra-Wideband, Short-Pulse Electromagnetics 5* (2002): 493-500.

[129] Shi, Y. F., F. X. Jin, and M. Y. Li. "A total entropy model of spatial data uncertainty." *Journal of information science* 32.4 (2006): 316-323.

[130] Estatico, Claudio, et al. "A Multifrequency Inexact-Newton Method in Lp banach Spaces for Buried Objects Detection." *IEEE Transactions on Antennas and Propagation* 63.9 (2015): 4198-4204.

[131] Scatterometer C- and X-band data, Indian Institute of Technology, Roorkee, India.

[132] Schmelzbach, Cedric, and Emanuel Huber. "Efficient deconvolution of ground-penetrating radar data." *IEEE transactions on geoscience and remote sensing* 53.9 (2015): 5209-5217.

[133] Kaur, Jaskirat, S. Agrawal, and R. Vig. "Performance analysis of clustering based image segmentation and optimization methods." *Computer Science & Information Technology CS & IT* 5.2 (2012): 2.

[134] Kumar, Nitin. "Thresholding in salient object detection: a survey." *Multimedia Tools and Applications* 77.15 (2018): 19139-19170.

[135] Pare, S., et al. "Image segmentation using multilevel thresholding: a research review." *Iranian Journal of Science and Technology, Transactions of Electrical Engineering* 44 (2020): 1-29.

[136] Chen, Siyue, and Henry Leung. "Chaotic spread spectrum watermarking for remote sensing images." *Journal of Electronic Imaging* 13.1 (2004): 220-230.

[137] Goh, Ta Yang, et al. "Performance analysis of image thresholding: Otsu technique." *Measurement* 114 (2018): 298-307.

[138] Yang, Xiaolu, et al. "An improved median-based Otsu image thresholding algorithm." *AASRI procedia* 3 (2012): 468-473.

[139] Charlton, M. B., and K. White. "Sensitivity of radar backscatter to desert surface roughness." *International Journal of Remote Sensing* 27.8 (2006): 1641-1659.

[140] Hussin, Yousif A. "Effect of polarization and incidence angle on radar return from urban features using L-band aircraft radar data." *1995 International Geoscience and Remote Sensing Symposium, IGARSS'95. Quantitative Remote Sensing for Science and Applications*. Vol. 1. IEEE, 1995.

[141] Elkotb, Ashraf Sami, et al. "Evaluating the Efficiency of Multisensor Satellite Data Fusion Based on the Accuracy Level of Land Cover/Use Classification." *Journal of Marine Science and Technology* 23.5 (2015): 24.

[142] Varghese, Alappat Ouseph, Arun Suryavanshi, and Asokh Kumar Joshi. "Analysis of different polarimetric target decomposition methods in forest density classification using C band SAR data." *International Journal of Remote Sensing* 37.3 (2016): 694-709.

[143] Cloude, Shane. *Polarisation: applications in remote sensing*. OUP Oxford, 2009.

[144] Freeman, Anthony, and Stephen L. Durden. "A three-component scattering model for polarimetric SAR data." *IEEE transactions on geoscience and remote sensing* 36.3 (1998): 963-973.

[145] Yamaguchi, Yoshio, et al. "Four-component scattering model for polarimetric SAR image decomposition." *IEEE Transactions on geoscience and remote sensing* 43.8 (2005): 1699-1706.

[146] Singh, Gulab, Yoshio Yamaguchi, and Sang-Eun Park. "General four-component scattering power decomposition with unitary transformation of coherency matrix." *IEEE Transactions on Geoscience and Remote Sensing* 51.5 (2012): 3014-3022.

[147] Maurya, Himanshu, and Rajib Kumar Panigrahi. "Non-negative scattering power decomposition for PolSAR data interpretation." *IET Radar, Sonar & Navigation* 12.6 (2018): 593-602.

[148] Maurya, Himanshu, et al. "Hybrid three-component scattering power characterization from polarimetric SAR data isolating dominant scattering mechanisms." *IEEE Transactions on Geoscience and Remote Sensing* 60 (2022): 1-15.

[149] Cloude, Shane. *Polarisation: applications in remote sensing*. OUP Oxford, 2009.

[150] Lang, Wenhui, et al. "Detection of ice types in the Eastern Weddell Sea by fusing L-and C-band SIR-C polarimetric quantities." *International journal of remote sensing* 35.19 (2014): 6874-6893.

[151] Huang, Xiaodong, et al. "Assessment of forest above ground biomass estimation using multi-temporal C-band Sentinel-1 and polarimetric L-band PALSAR-2 data." *Remote Sensing* 10.9 (2018): 1424.

[152] Ponnurangam, G. G., and Y. S. Rao. "The application of compact polarimetric decomposition algorithms to L-band PolSAR data in agricultural areas." *International Journal of Remote Sensing* 39.22 (2018): 8337-8360.

[153] Zou, Bin, et al. "Target detection based on L-and C-band PolSAR data." *2011 IEEE International Geoscience and Remote Sensing Symposium*. IEEE, 2011

[154] Khati, Unmesh, Gulab Singh, and Shashi Kumar. "Potential of space-borne PolInSAR for forest canopy height estimation over India—A case study using fully polarimetric L-, C-, and X-band SAR data." *IEEE Journal of Selected Topics in Applied Earth Observations and Remote Sensing* 11.7 (2018): 2406-2416.

[155] Radarsat-2 and ALOS PALSAR-1 POLSAR San Francisco sample data, Retrieved, May 2020 https://ietr-lab.univ-rennes1.fr/polsarpro-bio/san-francisco/

[156] Liu, Bo, et al. "Co-and cross-polarization decoupling structure with polarization rotation property between linearly polarized dipole antennas with application to decoupling of circularly polarized antennas." *IEEE Transactions on Antennas and Propagation* 70.1 (2021): 702-707.

[157] Sugimoto, Ryu, et al. "Deforestation detection using scattering power decomposition and optimal averaging of volume scattering power in tropical rainforest regions." *Remote Sensing of Environment* 275 (2022): 113018.

[158] Ainsworth, Thomas L., Yanting Wang, and Jong-Sen Lee. "Model-based polarimetric SAR decomposition: An L 1 regularization approach." *IEEE Transactions on Geoscience and Remote Sensing* 60 (2021): 1-13.

[159] Kumar, Shashi, et al. "Polarimetric calibration of spaceborne and airborne multifrequency SAR data for scattering-based characterization of manmade and natural features." *Advances in space research* 69.4 (2022): 1684-1714.

[160] Zhu, Xiaoxiu, et al. "Coherent compensation and high-resolution technology of multi-band inverse synthetic aperture radar fusion imaging." *IET Radar, Sonar & Navigation* 15.2 (2021): 167-180.

[161] Samrat, A., M. S. Devy, and T. Ganesh. "Delineating fragmented grassland patches in the tropical region using multi-seasonal synthetic aperture radar (SAR) and optical satellite images." *International Journal of Remote Sensing* 42.10 (2021): 3938-3954.

[162] Xie, Xiaohui. "Principal component analysis." *Wiley interdisciplinary reviews* (2019).

[163] Yang, Wenjie, et al. "Using principal components analysis and IDW interpolation to determine spatial and temporal changes of surface water quality of Xin'anjiang river in Huangshan, China." *International journal of environmental research and public health* 17.8 (2020): 2942.

[164] Labrín, Caterina, and Francisco Urdinez. "Principal component analysis." *R for Political Data Science*. Chapman and Hall/CRC, 2020. 375-393.

[165] Khan, Armugha, et al. "Synergistic use of Sentinel-1 and Sentinel-2 for improved LULC mapping with special reference to bad land class: a case study for Yamuna River floodplain, India." *Spatial Information Research* 28 (2020): 669-681.

[166] Chen, Yuxing, and Lorenzo Bruzzone. "Self-supervised sar-optical data fusion of sentinel-1/-2 images." *IEEE Transactions on Geoscience and Remote Sensing* 60 (2021): 1-11.

[167] Vohra, Rubeena, and K. C. Tiwari. "Object based classification using multisensor data fusion and support vector algorithm." *International Journal of Image and Data Fusion* 9.1 (2018): 63-81.

[168] Shakya, Achala, Mantosh Biswas, and Mahesh Pal. "CNN-based fusion and classification of SAR and Optical data." *International Journal of Remote Sensing* 41.22 (2020): 8839-8861.

[169] Rokni, Komeil, et al. "A new approach for surface water change detection: Integration of pixel level image fusion and image classification techniques." *International Journal of Applied Earth Observation and Geoinformation* 34 (2015): 226-234.

[170] Rahman, Ashikur, et al. "Performance of different machine learning algorithms on satellite image classification in rural and urban setup." *Remote Sensing Applications: Society and Environment* 20 (2020): 100410.

[171] Dataset: European space agency (ESA), online download https://scihub.copernicus.eu/.

[172] Kumar, Manoj, et al. "Speckle denoising techniques in imaging systems." *Journal of Optics* 22.6 (2020): 063001.

[173] Klonus, Sascha, and Manfred Ehlers. "Image fusion using the Ehlers spectral characteristics preservation algorithm." *GIScience & Remote Sensing* 44.2 (2007): 93-116.]

[174] Laben, Craig A., and Bernard V. Brower. "Process for enhancing the spatial resolution of multispectral imagery using pan-sharpening." U.S. Patent No. 6,011,875. 4 Jan. 2000.

[175] Yang, Xi, et al. "SAR-to-optical image translation based on improved CGAN." *Pattern Recognition* 121 (2022): 108208.

[176] McVittie, Alex. "SENTINEL-1 flood mapping tutorial." (2019).

[177] Singh, Prabhishek, et al. "A Review on SAR Image and its Despeckling." *Archives of Computational Methods in Engineering* 28 (2021): 4633-4653.

RESEARCH PUBLICATIONS

Research Papers in International Journal (Published)

(i)   Sanjay Singh, K. C. Tiwari, "Exploring the optimal combination of image fusion and classification techniques", *Remote Sensing Applications: Society and Environment*, Elsevier, volume -24, Nov-2021. Impact Factor: 4.7

(ii)   Sanjay Singh, K. C. Tiwari, ''SAR and Optical Pixel Level Fusion Methods and Evaluations,'' *Journal of Spatial Science*, 2022, Taylor & Francis, doi: 10.1080/14498596.2022.2153754. Impact factor: 1.9

Research Papers in International Conference

(i)   Sanjay Singh, K. C. Tiwari, 'Multi-Frequency SAR image fusion', 37th Asian conference of Remote Sensing, New Delhi,2017.

(ii)   Sanjay Singh, K. C. Tiwari, 'Impact of Speckle filtering algorithms and their window size on SAR and optical Image Fusion', International Conference on Advanced Electrical and Electronics, Noida, 30 December,2022.

AUTHOR'S BIOGRAPHY

Sanjay Singh received the Bachelor of Engineering (B.E.) from B.S.A. College of Engineering and Technology (Affiliated to Dr B.R. Ambedkar University), Mathura, Uttar Pradesh in the year 2001 and the Master of Technology (M.Tech.) from Gautam Budda Technical University (AKTU), Lucknow, Uttar Pradesh, India in the year 2011. He qualified the UGC National Eligibility Test (NET) for Assistant Professor in year 2015.He holds the position of Assistant Professor in Department of Electronics & Communication Engineering at Hindustan College of Science & Technology, Mathura, Uttar Pradesh since 2004. He joined Delhi Technological University, New Delhi as part time Ph.D. scholar in Electronics & Communication Engineering Department under the supervision of Dr. K. C. Tiwari. His research focuses include Microwave data fusion for improvement in detection of surface and buried objects and digital signal processing.

DELHI TECHNOLOGICAL UNIVERSITY

(Formerly Delhi College of Engineering)

Shahbad Daulatpur, Main Bawana Road, Delhi-110042

<u>PLAGIARISM VERIFICATION</u>

Title of the Thesis: **Object Detection using Fusion of Multiband Microwave Data**

Total Pages: **172**   Name of the Scholar: **Sanjay Singh**

Supervisor: **Prof Dr K. C. Tiwari**

Department: **Electronics & Communication Engineering**

This is to report that the above Thesis was scanned for similarity detection. Process and outcome is given below:

Software used: **Turnitin**   Similarity Index: **7%**   Total Word Count: **42680**

Date:

Signature of Supervisor

thesis sanjay singh for plag.pdf